

Chapter 1

Theoretical and Experimental Overview

1.1 Deep Inelastic Scattering

To understand the structure of the nucleon it is useful to first introduce the original process which described the nucleon as having a sub-structure. This process is the Deep Inelastic Scattering (DIS) process where a lepton impinges on a nucleon denoted as

$$l(\ell) + N(P) \rightarrow l(\ell') + X(P_X), \quad (1.1)$$

where l denotes a lepton, N denotes a nucleon, X represents all products not detected and ℓ, ℓ', P and P_X are the four momentum for their respective lepton or nucleon. This process is an electromagnetic reaction where a lepton is scattered via virtual photon exchange with the nucleon. The leading order Feynman diagram for this reaction is shown in Fig. 1.1.

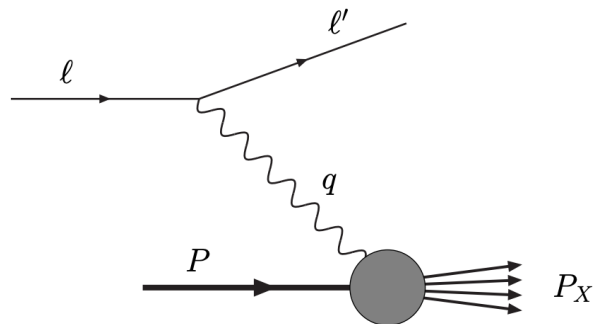


Figure 1.1: The leading order Feynman diagram for deep inelastic scattering

DIS is traditionally studied with a high energy lepton beam and a fixed nuclear target. The initial state kinematics are described by

$$s = (\ell + P)^2 \quad \text{or} \quad E, \quad (1.2)$$

where s is the center of mass energy and E is the energy of the lepton beam. The detected reaction kinematics in the lab frame are described by

$$Q^2 = -q^2 = -(\ell - \ell')^2 \approx EE'(1 - \cos\theta) \quad (1.3)$$

$$x = \frac{Q^2}{2P \cdot q} = \frac{Q^2}{2M\nu} \quad (1.4)$$

$$\nu = E - E' \quad (1.5)$$

$$y = \frac{P \cdot q}{P \cdot \ell} = \frac{E - E'}{E} = \frac{\nu}{E} \quad (1.6)$$

$$W^2 = (P + q)^2 \quad (1.7)$$

where q is the virtual photon four momentum, E' is the scattered leptons energy, x is Bjorken x , ν is the change in energy of the scattered lepton, y is the inelasticity and W^2 is invariant mass of hadron final state. In the last relation from Eq. 1.3, θ is the scattering angle of the lepton with respect to the beam and the approximation is only true when the lepton mass is assumed to be zero. In Eq. 1.4, M is the nucleon mass. In the parton model, section 1.2, x has the interpretation as being the momentum fraction of the struck parton with respect to its parent hadron and therefore x ranges between 0 and 1. The inelasticity, y , measure the proportional lepton energy reduction and therefore takes on a value between 0 and 1.

The process is called deep if $Q^2 \gg M^2$ and inelastic if $y < 1$. For practical purposes in experiments, the deep inelastic criteria corresponds to a $Q^2 > 1 \text{ GeV}$ and $W^2 > M^2$. As can be seen in Eq. [1.3-1.7], not all the variables are independent. DIS is described by two independent variables usually given by (x, Q^2) or (x, y) . For reference, in the limit as $y \rightarrow 1$ the process becomes elastic scattering and can then be described by only one independent variable.

The cross-section for DIS is defined as [11]

$$d\sigma = \frac{1}{4P \cdot \ell} \frac{e^4}{Q^4} L_{\mu\nu} W^{\mu\nu} 2\pi \frac{d^3\ell'}{(2\pi)^3 2E'} \quad (1.8)$$

where $L_{\mu\nu}$ is the leptonic tensor and $W^{\mu\nu}$ is the hadronic tensor. The leptonic tensor describes free leptons and can therefore be calculated in perturbation theory. It can be decomposed into a systematic spin-independent tensor and an anti-symmetric spin-dependent tensor. Summing over all the possible spins of the lepton beam, the leptonic tensor is

$$L_{\mu\nu} = 2 \left(\ell_\mu \ell'_\nu + \ell_\nu \ell'_\mu - g_{\mu\nu} \ell \cdot \ell' \right) + 2m\epsilon_{\mu\nu\rho\sigma} s^\rho q^\sigma \quad (1.9)$$

where m is the lepton mass and s^ρ is the spin four vector of the lepton.

Generically the hadronic tensor is defined as

$$W^{\mu\nu} = \frac{1}{2\pi} \int d^4\xi e^{iq\cdot\xi} \langle PS | J^\mu(\xi) J^\nu(0) | PS \rangle \quad (1.10)$$

where J is an electromagnetic current and $|PS\rangle$ represents the nucleon with momentum P and spin S . The hadronic tensor describes a hadron bound together by quantum chromo-dynamics (QCD). As of yet there is no known technique for calculating the hadronic tensor in a perturbation theory or otherwise. Instead the hadronic tensor can be written in the most general Lorentz invariant form using structure functions to parameterize the non-perturbative nature of the tensor. With the use of these structure functions, the differential DIS cross-section can be written

$$\frac{d\sigma}{dxdy} = \frac{8\pi\alpha^2 ME}{Q^4} \left\{ xy^2 F_1(x, Q^2) + \left(1-y\right) \frac{F_2(x, Q^2)}{x} + c_1(y, \frac{Q^2}{\nu}) g_1(x, Q^2) + c_2(y, \frac{Q^2}{\nu}) g_2(x, Q^2) \right\} \quad (1.11)$$

where α is the electromagnetic coupling constant; F_1 , F_2 , g_1 , g_2 are structure functions; and c_1 and c_2 are functions which depend on the polarization of the target. The SLAC collaboration measured the structure functions, F_1 and F_2 , and found mild variations as a function Q^2 [15, 18]. This phenomenon now known as Bjorken scaling lead to the theory of the parton model [13]. Fig. 1.2 shows the F_2 structure function which is approximately constant as a function of Q^2 .

1.2 The Parton Model

The parton model is described in what is called an infinite momentum frame where the nucleon is moving with large momentum. In the parton model the nucleon, in high energy scattering processes, is considered to be composed of point like constituent mass-less particles called partons. At high energy scattering the QCD strong force binding the partons becomes asymptotic small and therefore the partons appear to be free. The cross-section in DIS can then be described as a lepton scattering incoherently off a free parton in the nucleon. In the parton model the hadron tensor for scattering off a quark can be written as [11]

$$W^{\mu\nu} = \frac{1}{2\pi} \sum_q e_q^2 \sum_X \int \frac{d^3 P_X}{(2\pi)^3 2E_X} \int \frac{d^4 k}{(2\pi)^4} \int \frac{d^4 k'}{(2\pi)^4} \delta(k'^2) \times [\bar{u}(k') \gamma^\mu \langle X | u(k) | PS \rangle] * [\bar{u}(k') \gamma^\nu \langle X | u(k) | PS \rangle] \times (2\pi)^4 \delta^4(P - k - P_X) (2\pi)^4 \delta^4(k + q - k'), \quad (1.12)$$

where e_q is the electric charge of quark flavor q ; and u and \bar{u} are free Dirac spinors. This hadronic tensor can be simplified by introducing the quark-quark correlation matrix as

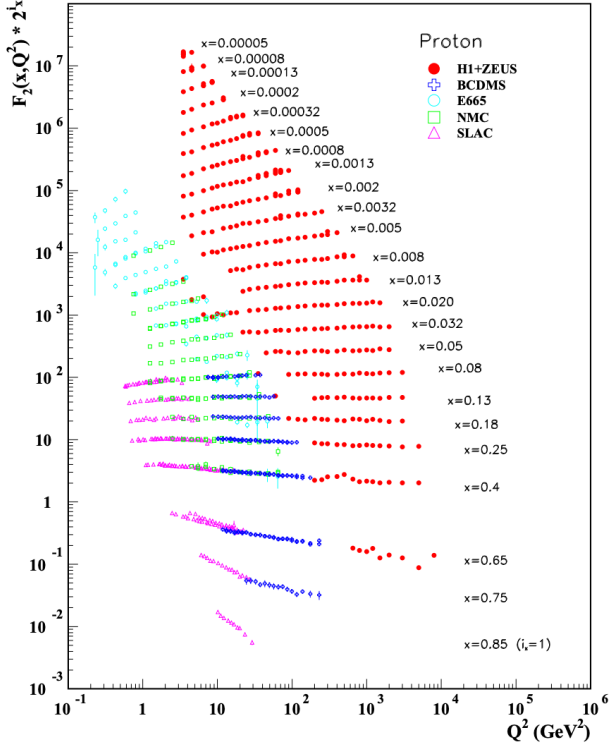


Figure 1.2: The F_2 structure function measured by several experiments. Note that the data is shifted up by a factor 2^{i_x} to see the x dependence. Image taken from [38]

$$\Theta_{ij}(k, P, S) = \sum_X \int \frac{d^3 P_X}{(2\pi)^3 2E_X} (2\pi)^4 \delta^4(P - k - P_X) \times \langle PS | \phi_j(0) | X \rangle \langle X | \phi_i(0) | PS \rangle, \quad (1.13)$$

where $\phi(\xi) = e^{-ip \cdot \xi} u(p)$ is a quark field. Using the quark-quark correlation matrix, the hadronic tensor can be written as

$$W^{\mu\nu} = \sum_q e_q^2 \int \frac{d^4 k}{(2\pi)^4} \int \frac{d^4 k'}{(2\pi)^4} \delta(k'^2) (2\pi)^4 \delta^4(k + q - k') \times \text{Tr}[\Theta \gamma^\mu k^\nu \gamma^\nu]. \quad (1.14)$$

In the cases of unpolarized or longitudinally polarized DIS the lead order contributing terms from the quark-quark correlator are [10, 16, 30]

$$\Theta = \frac{1}{2} \left(f_1(x) \not{p} + g_{1L}(x) \lambda \gamma_5 \not{p} \right) \quad (1.15)$$

where λ is the longitudinal polarization of the hadron. The hadronic tensor simplifies to a symmetric contribution and an anti-symmetric contribution [11]

$$W_{\mu\nu}^{\text{symmetric}} = \frac{1}{P \cdot q} \sum_q e_q^2 \left((k_\mu + q_\mu) P_\nu + (k_\nu + q_\nu) P_\mu - g_{\mu\nu} \right) f_1^q(x), \quad (1.16)$$

$$W_{\mu\nu}^{\text{anti-symmetric}} = \lambda \epsilon_{\mu\nu\rho\sigma} (k_\nu + q_\nu) P^\rho \sum_q e_q^2 g_{1L}^q(x), \quad (1.17)$$

where in Eq. 1.15 f_1 and g_1 are two parton distribution functions (PDFs). f_1 is interpreted as the quark number density and g_{1L} is interpreted as the total quark helicity distribution in a hadron. f_1 is then refers to the density of unpolarized quarks in a hadron and g_{1L} refers to the density of quarks longitudinally polarized in the same longitudinal direction as the hadron. To make this explicit, f_1 and g_{1L} can be written

$$f_1 = f_1^+ + f_1^-, \quad (1.18) \quad g_{1L} = f_1^+ - f_1^-, \quad (1.19)$$

where + and - denote the helicity. To be clear the parton distribution g_{1L} is not the same as the structure function g_1 .

The unpolarized quark number density, f_1 , has been extracted from global analysis of several experiments [24]. Fig. 1.3 shows the current xf_1 values and confidence intervals for different quarks and gluons specifically in the proton.

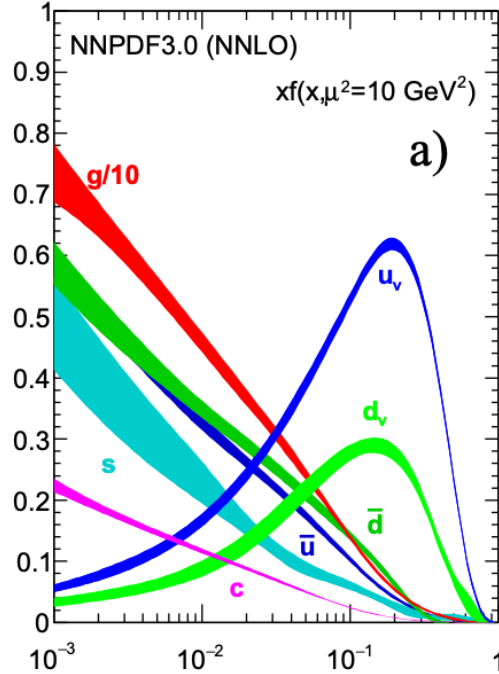


Figure 1.3: The unpolarized parton distribution functions times the momentum fraction. The different color correspond to different quarks or gluons. Image taken from [38]

The longitudinal spin structure, g_{1L} has also been measured at SMC, HERMES, and COMPASS [4, 6,

35]. The global analysis fit is shown in Fig. 1.4 using the parameterizations from NNPDF2014, AAC2008, DSSV2008 and LSS2010 [3, 27, 28, 31].

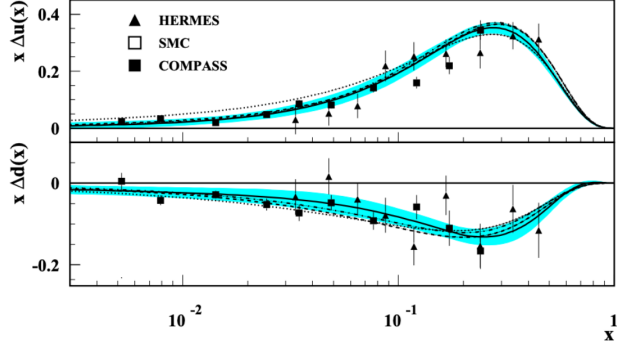


Figure 1.4: The longitudinally polarized parton distribution functions times the momentum fraction for the u-quark (top) and the d-quark (bottom). Image taken from [38]

In the parton model the structure function F_1 and F_2 are related to each other and to the unpolarized quark number as

$$F_2(x) = 2xF_1(x) = \sum_q e_q^2 x \left(f_1^q + f_1^{\bar{q}} \right) \quad (1.20)$$

which is known as the Callan-Gross relation [21]. As well the structure function g_1 is related to the helicity distribution, g_{1L} , as

$$g_1(x) = \frac{1}{2} \sum_q e_q^2 g_{1L}(x). \quad (1.21)$$

1.3 Transverse Momentum Dependence

The transverse momentum of the partons is integrated over when measuring the DIS process. This is because only the scattered lepton is measured and any transverse parton motion cannot be measured. The Drell-Yan process 1.5 and the SIDIS process 1.4 however are sensitive to the internal transverse momentum of the partons. In the limit of small transverse momentum compared to the virtual photon momentum and including the transverse parton momentum, the most generic leading order quark-quark correlator can be written [10, 16, 30]

$$\begin{aligned} \Theta = & \frac{1}{2} \left[f_1(x, k_\perp) \not{P} + \frac{1}{M} h_1^\perp(x, k_\perp) \sigma^{\mu\nu} k_\mu P_\nu + g_{1L}(x, k_\perp) \lambda \gamma_5 \not{P} \right. \\ & + \frac{1}{M} g_{1T}(x, k_\perp) \gamma_5 \not{P} (k_\perp \cdot S_\perp) + \frac{1}{M} h_{1L}(x, k_\perp) \lambda i \sigma_{\mu\nu} \gamma_5 P^\mu k_\perp^\nu + h_1(x, k_\perp) i \sigma_{\mu\nu} \gamma_5 P^\mu S_\perp^\nu \\ & \left. + \frac{1}{M^2} h_{1T}^\perp(x, k_\perp) i \sigma_{\mu\nu} \gamma_5 P^\mu \left(k_\perp \cdot S_\perp k_\perp^\nu - \frac{1}{2} k_\perp^2 S_\perp^\nu \right) + \frac{1}{M} f_{1T}^\perp(x, k_\perp) \epsilon^{\mu\nu\rho\sigma} \gamma_\mu P_\nu k_\rho S_\sigma \right], \end{aligned} \quad (1.22)$$

where k_{\perp} denotes the transverse parton momentum and S_{\perp} denotes the transverse hadron spin. Eq. 1.22 includes eight transverse momentum dependent (TMD) PDFs which are functions of x and k_{\perp} . The notation used to depict the TMDs functions is the so-called Amsterdam notation. The letters represent the different quark polarizations where f, g, h stand for unpolarized, longitudinally polarized and transversely polarized respectively. The subscript 1 denotes leading order and the subscripts T and L denote a transversely polarized hadron and a longitudinally polarized hadron respectively. Finally the superscript \perp denotes that the distribution is an odd function of k_{\perp} and therefore is zero when integrated over the parton transverse momentum. Fig. 1.5 organizes the TMDs by nucleon and quark polarizations and gives a visual of each TMD's interpretation.

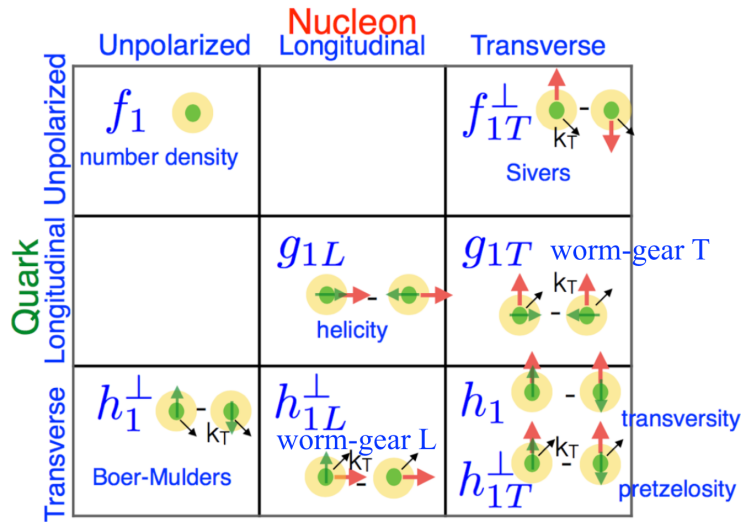


Figure 1.5: The eight TMDs needed to describe a spin 1/2 nucleon at leading order. The columns represent the different nucleon polarization and the rows represent the different quark polarizations. The individual figures give a visual of the TMD's interpretation.

1.3.1 Sivers Distribution

The Sivers TMD was first purposed to explain large nucleon spin-dependent asymmetries [36]. The interpretation of the Sivers TMD, $f_{1,T}^{q\perp}(x, \mathbf{k}_T)$, is that it gives a correlation between transverse spin of the parent hadron and transverse momentum of parton. When viewing the hadron in the direction of its momentum, if $f_{1,T}^{q\perp}(x, \mathbf{k}_T)$ is positive then it is expected that there are more partons with momentum going left than going right. Intuitively a non-zero $f_{1,T}^{q\perp}(x, \mathbf{k}_T)$ would then imply that the bound quarks carry orbital angular momentum. As of yet however, there is no theoretical link between orbital angular momentum and the Sivers function.

The Sivers function changes sign from naive time reversal. Naive time reversal is defined as reversing time but not swapping initial and final states [10]. The Sivers function is therefore said to be a T-odd function, and as a result it was originally believed to be a forbidden correlation. However it was shown that the Sivers function could be non-zero from gluon exchange during the initial state in the Drell-Yan process and during the final state in SIDIS [19, 20]. Surprisingly it was shown that a non-zero Sivers function is expected to have opposite sign in SIDIS and Drell-Yan [23]. That is

$$f_{1T}^\perp|_{Drell-Yan} = -f_{1T}^\perp|_{SIDIS}. \quad (1.23)$$

Include information on Bohr-Mulders, transversity and pretzelosity (all TSAs determined in DY). Give Star Sivers result.

1.4 Semi-Inclusive Deep Inelastic Scattering

Semi-Inclusive Deep Inelastic Scattering (SIDIS) is the process where a lepton scatters electromagnetically off a nucleon and subsequently the scattered lepton and at least one scattered hadron are detected. As the name implies, SIDIS is related to the DIS reaction only SIDIS includes the addition of a detected hadron. SIDIS is denoted as

$$l(\ell, \lambda_l) + N(P, S) \rightarrow l(\ell') + h(P_h) + X(P_X), \quad (1.24)$$

where λ_l is the helicity of the incoming lepton, S is the spin of the nucleon, h is the detected hadron and P_h is the detected hadron's four momentum. The leading order one photon exchange Feynman diagram for the SIDIS process is shown in Fig. 1.6.

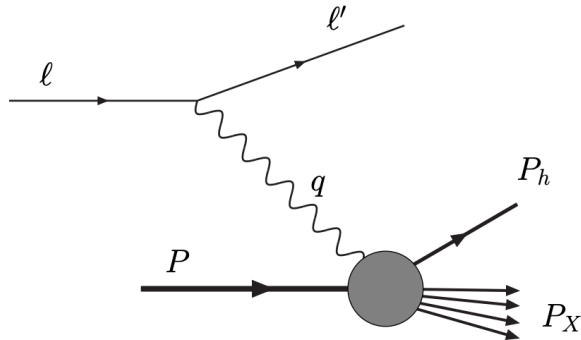


Figure 1.6: The semi-inclusive deep inelastic scattering leading order Feynman diagram

In addition to the kinematic variables used to describe DIS, Eq. [1.3-1.7], one more variable is needed to describe the SIDIS process,

$$z = \frac{P \cdot P_h}{P \cdot q} \stackrel{\text{frame}}{=} \frac{E_h}{E - E'}, \quad (1.25)$$

which is interpreted as the fraction of possible energy the detected hadron can obtain. The transverse spin-dependent SIDIS cross-section can be described in a model independent way using structure functions as [10]

$$\begin{aligned} \frac{d\sigma}{dx dy d\psi dz d\phi_h dP_{h\perp}^2} &= \frac{\alpha^2}{xyQ^2} \frac{y^2}{2(1-\varepsilon)} \left(1 + \frac{\gamma^2}{2x}\right) \left\{ F_{UU,T} + \varepsilon F_{UU,L} + \sqrt{2\varepsilon(1+\varepsilon)} \cos \phi_h F_{UU}^{\cos \phi_h} \right. \\ &\quad + \varepsilon \cos(2\phi_h) F_{UU}^{\cos 2\phi_h} + \lambda_l \sqrt{2\varepsilon(1-\varepsilon)} \sin \phi_h F_{LU}^{\sin \phi_h} \\ &\quad + |S_\perp| \left[\sin(\phi_h - \phi_S) \left(F_{UT,T}^{\sin(\phi_h - \phi_S)} + \varepsilon F_{UT,L}^{\sin(\phi_h - \phi_S)} \right) \right. \\ &\quad \left. + \varepsilon \sin(\phi_h + \phi_S) F_{UT}^{\sin(\phi_h + \phi_S)} + \varepsilon \sin(3\phi_h - \phi_S) F_{UT}^{\sin(3\phi_h - \phi_S)} \right. \\ &\quad \left. + \sqrt{2\varepsilon(1+\varepsilon)} \sin \phi_S F_{UT}^{\sin \phi_S} + \sqrt{2\varepsilon(1-\varepsilon)} \sin(2\phi_h - \phi_S) F_{UT}^{\sin(2\phi_h - \phi_S)} \right] \\ &\quad + |S_\perp| \lambda_l \left[\sqrt{1-\varepsilon^2} \cos(\phi_h - \phi_S) F_{LT}^{\cos(\phi_h - \phi_S)} + \sqrt{2\varepsilon(1-\varepsilon)} \cos \phi_S F_{LT}^{\cos \phi_S} \right. \\ &\quad \left. + \sqrt{2\varepsilon(1-\varepsilon)} \cos(2\phi_h - \phi_S) F_{LT}^{\cos(2\phi_h - \phi_S)} \right] \}, \end{aligned} \quad (1.26)$$

where

$$\varepsilon = \frac{1-y - \frac{1}{4}\gamma^2 y^2}{1-y + \frac{1}{2}y^2 + \frac{1}{4}\gamma^2 y^2}, \quad (1.27)$$

and $\gamma = \frac{2M_x}{Q}$ and ψ is the azimuthal scattering angle of the lepton around the lepton beam with respect to the transverse spin direction of the target. The SIDIS cross-section, Eq. 1.26, is defined in the γ -nucleon reference frame which is a target frame where the virtual photon is along the z-axis and the xz-plane is determined by the lepton plane. Fig. 1.7 shows the γ -nucleon lab frame and the relevant azimuthal angles.

The 14 structure functions in Eq. 1.26 are coefficients to the azimuthal angles. The structure functions are labeled as F where the superscript denotes which azimuthal angle coefficient they correspond to and the three subscripts represent the beam, target and virtual photon polarization from left to right respectively. The subscript polarizations are U for unpolarized, L for longitudinally polarized and T for transversely polarized. The cross-section, Eq. 1.26, is determined similarly to the DIS cross-section, Eq. 1.11, in that

structure functions are used to generically parameterize the hadronic tensor.

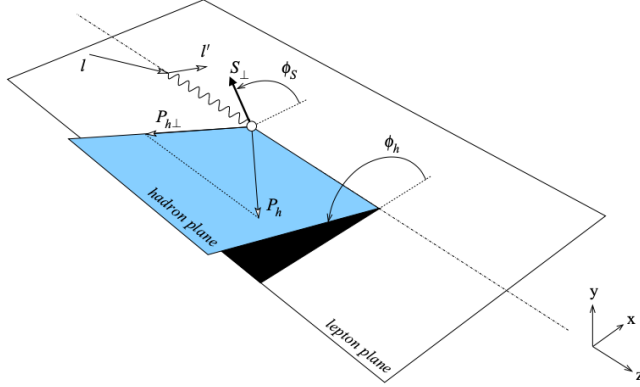


Figure 1.7: The γ -nucleon lab frame where the target nucleon is at rest and the virtual photon is along the z -axis. The lepton scattering plane defines the xz -plane where the outgoing lepton defines the positive x -direction. This image was taken from [10].

In the TMD regime the structure functions are related to TMD function and fragmentation functions (FF). That is to say where the detected hadron's transverse momentum is small compared to the virtual photon momentum, $P_{hT} \ll Q$, the model independent structure functions are related to TMD functions. The structure functions are equal to a convolution of a TMD and a FF in this regime where the convolution is defined as

$$\mathcal{C}[w(p_T, k_T)fD] = x \sum_q e_q^2 \int d^2 p_T d^2 k_T \delta^{(2)}(p_T - k_T - P_{h\perp}/z) w(p_T, k_T) f^q(x, p_T^2) D^q(z, k_T^2), \quad (1.28)$$

where w is a weight f is a TMD function and D is a FF. The relation between structure functions and TMDs at leading order for the structure functions related to transverse target polarization are [10]

$$F_{UT,T}^{\sin(\phi_h - \phi_S)} = \mathcal{C} \left[-\frac{\hat{h} \cdot p_T}{M} f_{1T}^\perp D_1 \right] \propto f_{1T}^\perp \otimes D_1, \quad (1.29)$$

$$F_{UT,L}^{\sin(\phi_h - \phi_S)} = 0, \quad (1.30)$$

$$F_{UT}^{\sin(\phi_h + \phi_S)} = \mathcal{C} \left[-\frac{\hat{h} \cdot k_T}{M_h} h_1 H_1^\perp \right] \propto h_1 \otimes H_1^\perp, \quad (1.31)$$

$$F_{UT}^{\sin(3\phi_h - \phi_S)} = \mathcal{C} \left[\frac{2(\hat{h} \cdot p_T)(\mathbf{p}_T \cdot \mathbf{k}_T) + \mathbf{p}_T^2(\hat{h} \cdot \mathbf{k}_T) - 4(\hat{h} \cdot p_T)^2(\hat{h} \cdot \mathbf{k}_T)}{2M^2 M_h} h_{1T}^\perp H_1^\perp \right] \propto h_{1T}^\perp \otimes H_1^\perp, \quad (1.32)$$

$$F_{LT}^{\cos(\phi_h - \phi_S)} = \mathcal{C} \left[\frac{\hat{h} \cdot p_T}{M} g_{1T} D_1 \right] \propto g_{1T} \otimes D_1, \quad (1.33)$$

and the leading order structure functions related to an unpolarized target are

$$F_{UU,T} = \mathcal{C}[f_1 D_1] \propto f_1 \otimes D_1, \quad (1.34)$$

$$F_{UU,L} = 0, \quad (1.35)$$

where the unit vector $\hat{h} = P_{h\perp}/|P_{h\perp}|$ and D_1 and H_1^\perp are fragmentation functions. The fragmentation functions are functions of z and describe the probability for a quark to hadronize to a specific hadron. These fragmentation functions depend on the quark spin, the hadron type and polarization and the quark k_T . In Eq. [1.29- 1.35] the fragmentation function D_1 refers to an unpolarized quark fragmenting to an unpolarized hadron and H_1^\perp refers to a transversely polarized quark fragmenting to an unpolarized hadron.

The SIDIS cross-section, Eq. 1.26, can be rewritten in terms of asymmetries. These asymmetries are defined as

$$A_{BeamTarget}^{w_i(\phi_h, \phi_S)} = \frac{F_{BeamTarget}^{w_i(\phi_h, \phi_S)}}{F_{UU,T} + \varepsilon F_{UU,L}}, \quad (1.36)$$

where $w_i(\phi_h, \phi_S)$ is the azimuthal angle associated with this asymmetry and *Beam* and *Target* represent the polarization of the beam and target. The asymmetry amplitude, Eq. 1.36, is a structure function divide by the unpolarized structure functions. This asymmetry amplitude definition is defined because it is easier to measure experimentally. In order to determine an asymmetry amplitude, the number of counts experimentally measures can be fit using a function in the form of Eq. 1.26 with the coefficients to each azimuthal amplitude as parameters to the fit. The result of the fit can determine the spin-dependent asymmetry amplitudes without needing to determine the luminosity.

COMPASS and HERMES measurements the asymmetry $A_{UT,T}^{\sin(\phi_h - \phi_S)}$ from the SIDIS reaction from a proton target [5, 8]. The comparison of the result between these two collaboration is shown in Fig. 1.8. The asymmetry amplitude $A_{UT,T}^{\sin(\phi_h - \phi_S)}$ is related to the Sivers function and was measured to be non-zero at the level of 5%.

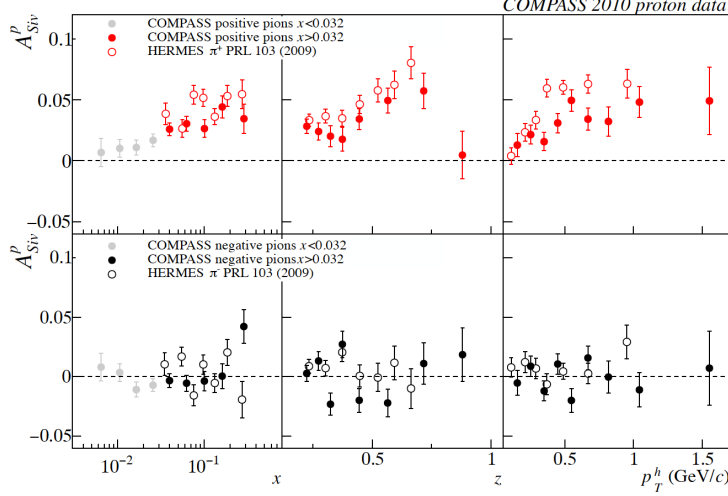


Figure 1.8: The asymmetry amplitude related to the Sivers function measure by COMPASS [8] and HERMES [5]

The top plots in Fig. 1.8 is the asymmetry for a positive detected hadron which is dominated by u-quark scattering and therefore by the u-quark Sivers function. This is the case for three reasons. Firstly because the SIDIS reaction is weighted by charge squared which therefore makes the u-quark scattering four times more likely. Secondly the so-called favor FF, where the detected hadron is the same charge as the which quark fragmented, is larger than the unfavored FF. Therefore a positively detected hadron most likely resulted from a positively fragmenting quark. Thirdly the proton target is composed twice as many u-quarks as d-quarks in this scattering kinematic region. For these three reasons the results in Fig. 1.8 imply that the u-quark Sivers function from the SIDIS reaction is positive.

The bottom plots in Fig. 1.8 suggest that the d-quark Sivers function in the SIDIS reaction is negative. The bottom results in Fig. 1.8 are from the combination of u-quark scattering then fragmenting unfavorably and d-quark scattering and fragmenting favoredly. As was mentioned the charge weighting in the SIDIS reaction and the proton quark composition results in the u-quark scattering with a higher probability. On the other hand the favor FF for d-quark fragmenting to a negatively charged hadron versus the unfavored FF for u-quark fragmenting to a negatively charged hadron cancel the previous effect out. Therefore results in the bottom of Fig. 1.8 are for an equal combination from u-quark scattering and d-quark scattering. As the u-quark asymmetry amplitude is positive, the d-quark asymmetry amplitude must therefore be negative

and so also must the d-quark Sivers function.

1.5 Drell-Yan

The Drell-Yan process is the reaction where a quark and an anti-quark annihilate and the end product results in two leptons. The Drell-Yan process is denoted as

$$H_a(P_a) + H_b(P_b, S) \rightarrow \gamma^* + X \rightarrow l(\ell) + l'(\ell') + X \quad (1.37)$$

where H_a and H_b are hadrons which carry the quark and anti-quarks and only the target hadron, H_b is considered to polarized with spin S . In this thesis the quark anti-quark pair annihilate to form a virtual photon, γ^* and in addition the final state leptons detected are a muon and an anti-muon. The leading order one photon exchange diagram is shown in Fig. 1.9.

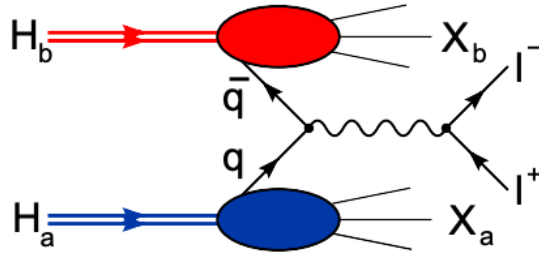
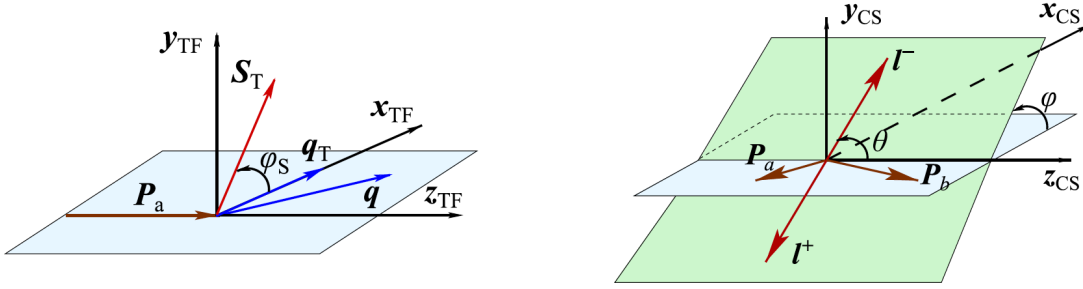


Figure 1.9: The Drell-Yan leading order diagram

The angles used to define the general Drell-Yan cross-section are defined with the use of two reference frames. The target frame (TF), Fig. 1.10a, defines the ϕ_S angle and the Collins-Soper (CS), Fig. 1.10b, frame defines the additional ϕ and θ angles. The ϕ_S angle is defined in TF as the angle between the transverse momentum of the virtual photon and the transverse spin of the target. The ϕ and θ angles, in the CS frame, are defined as the azimuthal and polar angle of the negatively charged muon.

The target frame is defined in the lab frame where the lab frame is rotated so the beam is along the z-axis and the transverse momentum of the virtual photon is along the x-axis. The y-axis in the target frame is then chosen so the coordinate system is right handed. The Collins-Soper frame is defined in the rest frame of the virtual photon where the xz-plane coincides with the hadron plane and the z-axis is chosen so it bisects the momentum vectors P_a and $-P_b$. The CS frame is defined from the target frame as a boost first along the along z-axis and then a boost along the x-axis so the rest frame of the virtual photon is reached. In this way the x-axis of the CS frame is defined and then the y-axis is again chosen so the coordinate system is



(a) The target frame where the z -axis is along the beam and the x -axis is in the direction of the transverse momentum of the virtual photon.

(b) The Collins-Soper frame is defined in the rest frame of the virtual photon where the z -axis bisects the beam and target momentum vectors.

right handed.

The leading order model independent Drell-Yan differential cross-section for a polarized target is [9, 29]

$$\begin{aligned} \frac{d\sigma}{d^4q d\Omega} = & \frac{\alpha_{em}^2}{F q^2} \left\{ \left((1 + \cos^2 \theta) F_U^1 + (1 - \cos^2 \theta) F_U^2 + \sin 2\theta \cos \phi F_U^{\cos \phi} + \sin^2 \theta \cos 2\phi F_U^{\cos 2\phi} \right) \right. \\ & + S_L \left(\sin 2\theta \sin \phi F_L^{\sin \phi} + \sin^2 \theta \sin 2\phi F_L^{\sin 2\phi} \right) \\ & + |S_T| \left[\left(F_T^{\sin \phi_S} + \cos^2 \theta \tilde{F}_T^{\sin \phi_S} \right) \sin \phi_S + \left(F_T^{\sin(\phi+\phi_S)} \sin(\phi + \phi_S) + F_T^{(\sin \phi - \phi_S)} \sin(\phi - \phi_S) \right) \sin 2\theta \right. \\ & \left. \left. + \left(F_T^{\sin(2\phi+\phi_S)} \sin(2\phi + \phi_S) + F_T^{\sin(2\phi-\phi_S)} \sin(2\phi - \phi_S) \right) \sin^2 \theta \right] \right\}, \end{aligned} \quad (1.38)$$

where $F = 4\sqrt{(P_a \cdot P_b)^2 - M_a^2 M_b^2}$ is the flux and Ω is the solid angle of the outgoing negatively charged muon. The twelve model independent structure functions in Eq. 1.38 are labeled as $F_{\text{Target polarization}}^{\text{azimuthal angle coefficient}}$. The phase space when the TMD regime is valid in DY scattering is when $q_T \ll q$. In this regime the structure functions are equal to a convolution of a beam and a target TMD function. The convolution is defined similarly to the SIDIS case, Eq. 1.28, as

$$\begin{aligned} \mathcal{C}[w(k_{aT}, k_{bT}) f_1 \bar{f}_2] = & \frac{1}{N_c} \sum_q e_q^2 \int d^2 k_{aT} d^2 k_{bT} \delta^{(2)}(q_T - k_{aT} - k_{bT}) \\ & \times w(k_{aT}, k_{bT}) \left[f_1^q(x, k_{aT}^2) f_2^{\bar{q}}(x, k_{bT}^2) + f_1^{\bar{q}}(x, k_{aT}^2) f_2^q(x, k_{bT}^2) \right], \end{aligned} \quad (1.39)$$

where $N_c = 3$ is the number of color charges and in this notation f_1 is a beam TMD function and f_2 is a target TMD function. The leading order DY structure functions in the TMD phase space are related to

TMD functions as [9]

$$F_U^1 = \mathcal{C}[f_1 \bar{f}_1] \propto f_{1,Beam}^{\bar{u}} \otimes f_{1,Target}^u, \quad (1.40)$$

$$F_U^{\cos 2\phi} = \mathcal{C} \left[\frac{2(\vec{h} \cdot \vec{k}_{aT})(\vec{h} \cdot \vec{k}_{bT}) - \vec{k}_{aT} \cdot \vec{k}_{bT}}{M_a M_b} h_1^\perp \bar{h}_1^\perp \right] \propto h_{1,Beam}^{\perp \bar{u}} \otimes h_{1,Target}^{\perp u}, \quad (1.41)$$

$$F_L^{\sin 2\phi} = -\mathcal{C} \left[\frac{2(\vec{h} \cdot \vec{k}_{aT})(\vec{h} \cdot \vec{k}_{bT}) - \vec{k}_{aT} \cdot \vec{k}_{bT}}{M_a M_b} h_1^\perp \bar{h}_{1L}^\perp \right] \propto h_{1,Beam}^{\perp \bar{u}} \otimes h_{1L,Target}^{\perp u}, \quad (1.42)$$

$$F_T^1 = \mathcal{C} \left[\frac{\vec{h} \cdot \vec{k}_{bT}}{M_b} f_1 \bar{f}_{1T}^\perp \right] \propto f_{1,Beam}^{\bar{u}} \otimes f_{1T,Target}^{\perp u}, \quad (1.43)$$

$$F_T^{\sin(2\phi - \phi_S)} = -\mathcal{C} \left[\frac{\vec{h} \cdot \vec{k}_{aT}}{M_a} h_1^\perp \bar{h}_1 \right] \propto h_{1,Beam}^{\perp \bar{u}} \otimes h_{1,Target}^u, \quad (1.44)$$

$$F_T^{\sin(2\phi + \phi_S)} = -\mathcal{C} \left[\frac{2(\vec{h} \cdot \vec{k}_{bT})[2(\vec{h} \cdot \vec{k}_{aT})(\vec{h} \cdot \vec{k}_{bT}) - \vec{k}_{aT} \cdot \vec{k}_{bT}] - \vec{k}_{bT}^2 (\vec{h} \cdot \vec{k}_{aT})}{2M_a M_b^2} h_1^\perp \bar{h}_{1T}^\perp \right] \propto h_{1,Beam}^{\perp \bar{u}} \otimes h_{1T,Target}^{\perp u}, \quad (1.45)$$

where $\vec{h} = \vec{q}_T/q_T$ is a unit vector and furthermore the assumption is made that the beam \bar{u} -quark annihilates with the target u -quark. The additional leading order structure functions are zero

$$F_U^2 = F_U^{\cos \phi} = F_L^{\sin \phi} = F_T^2 = F_T^{\sin(\phi - \phi_S)} = F_T^{\sin(\phi + \phi_S)} = 0. \quad (1.46)$$

The differential cross-section, Eq. 1.38, can be rewritten in terms of asymmetry amplitudes and depolarization factors. The asymmetry amplitudes are defined similarly to the case in SIDIS, Eq. 1.36, and again for the reason that asymmetries can be determined to a higher precision than structure functions. For Drell-Yan these asymmetry amplitudes are

$$A_{Target}^{w_i(\phi, \phi_S)} = \frac{F_{Target}^{w_i(\phi, \phi_S)}}{F_U^1 + F_U^2}, \quad (1.47)$$

The asymmetry amplitudes are the result of different virtual photon polarizations decaying to final state

lepton pair. The depolarization factor is defined as the ratio of the virtual photon polarization to produce such an asymmetry to that of a transversely polarized virtual photon. The depolarization is defined for each asymmetry amplitude as

$$D_{[f(\theta)]} = \frac{f(\theta)}{1 + A_U^1 \cos^2 \theta}, \quad (1.48)$$

where the function $f(\theta)$ corresponds to virtual photon angular decay responsible for the given asymmetry. The Drell-Yan differential cross-section, Eq. 1.38, now simplifies to [29]

$$\begin{aligned} \frac{d\sigma}{d^4 q d\Omega} = & \frac{\alpha_{em}^2}{F q^2} \hat{\sigma}_U \left\{ \left(1 + D_{[\sin^2 \theta]} \cos 2\phi A_U^{\cos 2\phi} \right) \right. \\ & + S_L D_{[\sin^2 \theta]} \sin 2\phi A_L^{\sin 2\phi} \\ & \left. + |S_T| \left[A_T^{\sin \phi_S} \sin \phi_S + \left(A_T^{\sin(2\phi + \phi_S)} \sin(2\phi + \phi_S) + A_T^{\sin(2\phi - \phi_S)} \sin(2\phi - \phi_S) \right) D_{[\sin^2 \theta]} \right] \right\}, \end{aligned} \quad (1.49)$$

where $\hat{\sigma}_U = F_U^1 (1 + \cos^2 \theta)$ is the unpolarized DY cross-section.

1.6 Weighted Asymmetries

Chapter 2

The COMPASS Experiment at CERN

The COmmon Muon Proton Apparatus for Structure and Spectroscopy (COMPASS) experiment is a fixed target experiment located in France in the North Area at CERN. COMPASS started taking data in 2002 in the same hall as earlier European Muon Collaboration (EMC), New Muon Collaboration (NMC) and Spin Muon Collaboration (SMC) experiments. COMPASS has studied hadron structure through (SI)DIS, Drell-Yan and Primakoff reactions and has done hadron spectroscopy measurements.

CERN is the European Organization for Nuclear physics research. It is located part in France and part in Switzerland and includes many experiments and accelerators providing beam to these experiments. The accelerator beam lines are connected and feed beam to each other resulting in an increase in beam momentum at each successive accelerator. A schematic of the accelerators at CERN is shown in Fig. 2.1 where the accelerator that sends beam to COMPASS is the Super Proton Synchrotron (SPS).

The COMPASS spectrometer is a two-stage spectrometer. The two stages are series where each stage contains various tracking detectors and a muon wall filter at the end of each stage. Any particles that penetrate through the active area of either of the muon wall filters are with a high probability, muons. Both stages also contain an electromagnetic and hadron calorimeter. The stages are both centered around a strong spectrometer magnet used for determining particle momentum. The first stage downstream of the target is the large angle spectrometer (LAS) and it is centered around the SM1 magnet which has an integrated field of 1 Tm. This stage detects tracks with larger polar scattering angles roughly between 26 mrad and 160 mrad. The second stage is the small angle spectrometer (SAS) and it detects particle tracks having a scattering angle between roughly 8 mrad and 45 mrad. This stage is centered around the SM2 magnetic which has an integrated field of 4.4 Tm.

The left and right side of the spectrometer are referred to by the mountains that surround the spectrometer. When looking down the beam line the left side is referred to as the Jura side which roughly corresponds to the west side and the right side is referred to as the Saleve side which roughly corresponds to the east side. A graphic of the 2015 setup is shown in Fig 2.2.

This chapter gives an overview of the general COMPASS data taking setup and highlights the specific

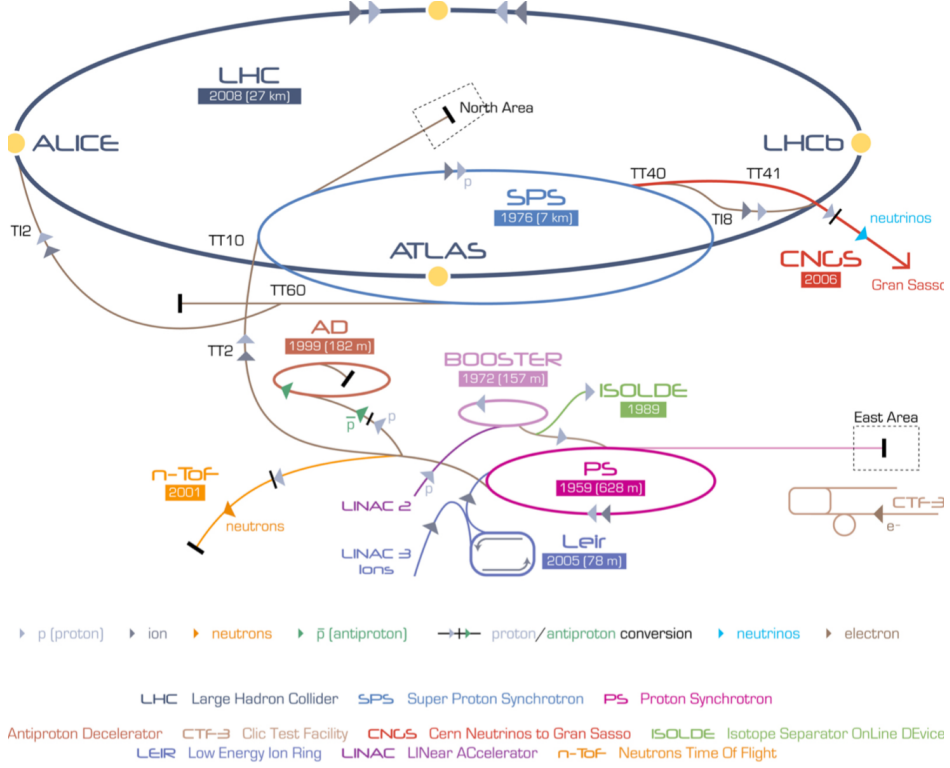


Figure 2.1: The CERN experiments and accelerators

features in 2015. All the data in this thesis was produced with the 2015 setup. For a more thorough review of the spectrometer see reference [1]. This chapter is roughly organized by how the data taking occurs and concludes with an extra section summarizing the unique features of the 2015 Drell-Yan data taking conditions.

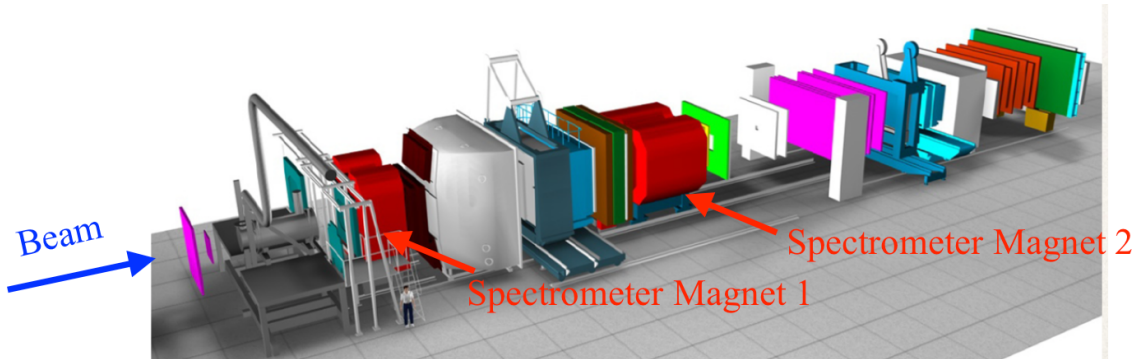


Figure 2.2: A schematic of the 2015 COMPASS setup

2.1 The Beam

The COMPASS spectrometer receives beam from the Super Proton Synchrotron along the M2 beam line. A schematic of the components in the M2 beam line is shown in Fig. 2.3. The SPS is the second largest accelerator at CERN with a circumference of almost 7 km which accelerates protons up to an energy of 450 GeV. The SPS extracts beam to famous Large Hadron Collier and as well sends beam to various experiments in the North Area at CERN. While the COMPASS spectrometer is above ground, the SPS is below ground and the M2 beam line must bend the beam from below ground to ground level.

There are several different beam types and energies available to COMPASS. The beam types used for physics analysis are a tertiary muon beam up to 190 GeV/ c and secondary hadron beam with an energy up to 280 GeV/ c . Both of the previous beam types can have a positive or negative charge. As well as the other two beam types it is also possible to have a low intensity tertiary electron beam, mainly used for calibrations.

The start of the M2 beam line is the T6 target. The SPS can accelerates primary protons up to 400 GeV/ c to impinge on this T6 target which produces a secondary beam. The nominal proton intensity on the T6 target is 100×10^{11} spill $^{-1}$. The T6 target is made of beryllium and has an adjustable length. The longer the T6 target the higher the secondary intensity where 500mm is the longest and typical target length used for physics data taking. The reaction of the proton beam with the T6 mainly produces secondary protons, pions and kaons. Following this reaction a series of dipole and quadruple magnets select the momentum and charge of interest.

The SPS spill structure varies throughout the data taking year depending mainly on the needs of the Large Hadron Colider (LHC). In 2015 the average intensity provided was 0.6×10^8 s $^{-1}$ and the typical spill structure was two 4.8 second spills every 36 seconds.

2.1.1 Muon Beam

The muon beam is a tertiary beam which results from a weak decay of the secondary beam. After the initial proton reaction on T6 the resulting secondary particles are momentum and charge selected and sent through a 600m tunnel with focusing and de-focusing (FODO) quadruple magnets. In this tunnel the secondary pions and kaons can decay as

$$\pi^{-(+)} \rightarrow \mu^{-(+)} + \bar{\nu}_{\mu^-}(\nu_{\mu^+}) \quad (2.1)$$

and

$$K^{-(+)} \rightarrow \mu^{-(+)} + \bar{\nu}_{\mu^-}(\nu_{\mu^+}), \quad (2.2)$$

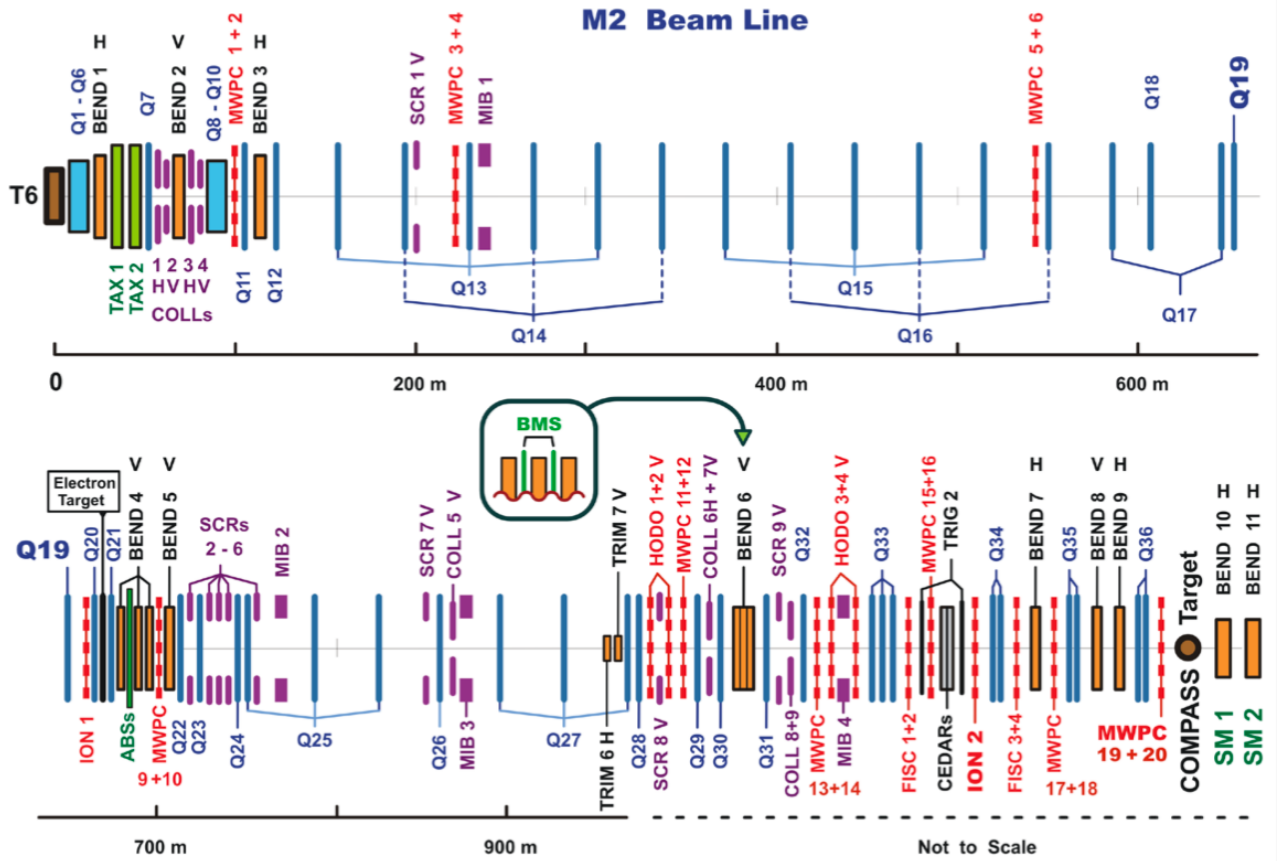


Figure 2.3: The M2 beam line at CERN

where $K^{-(+)}$ is a kaon of negative or positive charge. At the end of the tunnel, a series of nine 1.1 m long beryllium absorbers, referred to as the ABS in Fig. 2.3, remove the remaining hadron component which did not decay. A 172 GeV/c secondary pion beam is chosen to achieve a 160 GeV/c tertiary muon beam. Due to the fact that the neutrino in the reactions 2.1 and 2.2 is always left handed, the muon will naturally be longitudinally polarized. For the muon momentum chosen, the muon beam achieves a polarization of 80%.

2.1.2 Hadron Beam

To deliver a hadron beam to COMPASS the ABS absorbers are not used. The decayed muons used for the tertiary muon beam have a lower momentum than the hadron beam and are therefore removable by magnetically rejecting these lower momentum muons. In the case of a negative hadron beam as in 2015, the composition of the beam is approximately 97 % π^- , 2.5% kaons and 0.5% \bar{p} . The 2015 Drell-Yan data taking was performed with a 190 GeV/ c hadron beam.

2.1.3 Additional Beam Line Components

After the decay tunnel the beam is bent upwards along another FODO tunnel. The length of this tunnel is 250m and reaches the surface level approximately 100m before the COMPASS target. A series of three dipole magnets, called bend 6, then bend the beam to a horizontal position aimed at the COMPASS target. Both upstream and downstream of bend 6, there are three tracking detectors (BM01-BM06) that make up the Beam Momentum Station (BMS). The BMS is the upstream most component of the COMPASS spectrometer. It is able to determine the beam momentum to better than 1% of the beam momentum with an efficiency of approximately 93%. Bend 6 and the BMS are shown schematically in Fig. 2.4.

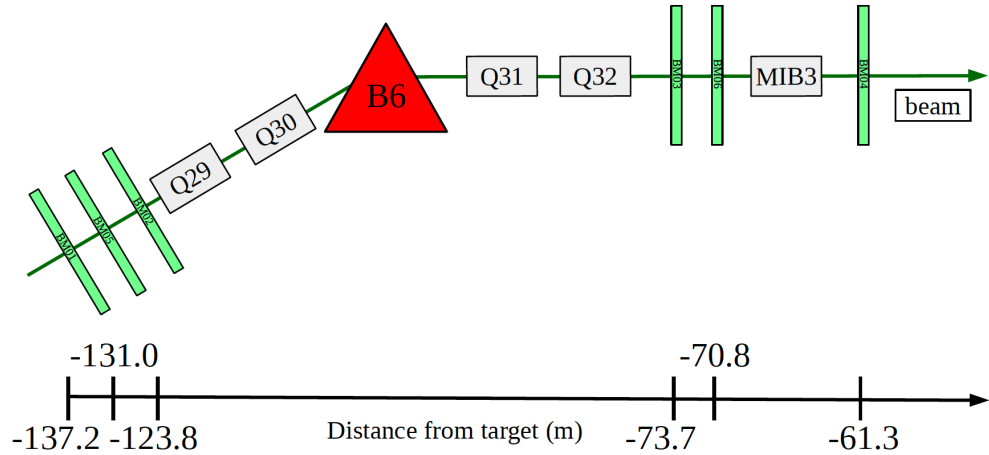


Figure 2.4: Bending the beam to a horizontal position. The BMS detectors are upstream and downstream of the bend 6 magnet.

During the 2015 Drell-Yan setup the π^- beam intensity was too high for the BMS station to work properly. For this reason, special low intensity, approximately 10^6 s^{-1} , π^- beams were used in 2014 to determine the momentum distribution during Drell-Yan data taking. The beam momentum distribution is shown in Fig. 2.5 where the average momentum is 190.9 GeV/ c with a spread of $\pm 3.2 \text{ GeV}/c$.

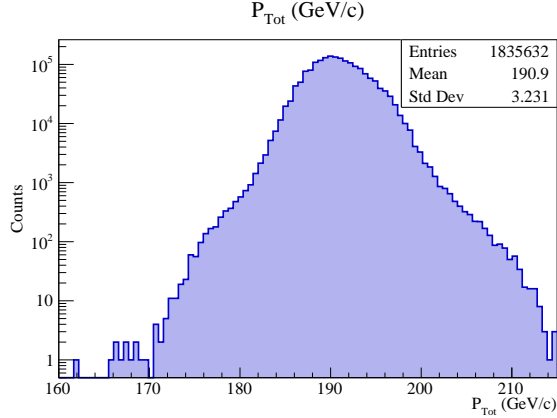


Figure 2.5: The momentum distribution of the π^- beam, determined during dedicated low intensity beam conditions

Approximately 30 m upstream of the target are two Cherenkov counter (CEDAR) detectors. As the hadron beam has contamination from several components these CEDARs can be used to distinguish between the different components. The CEDARs at COMPASS are high pressure detectors and have been demonstrated to achieve fast particle identification for particle momentums up to 300 GeV/c . The CEDARs general principle of operation is that two particles with the same momentum but different mass will emit Cherenkov radiation at different angles relative to their momentum. When a particle is traveling faster than the speed of light in a given medium, it emits Cherenkov radiation in a cone centered along its momentum axis. The faster the particle is traveling the narrower the angle of the Cherenkov light cone. A schematic of the CEDAR operating principle is shown in Fig. 2.6. In 2015 the CEDARs were measured to be largely inefficient due to the high beam intensity and are not used for the analysis of this thesis.

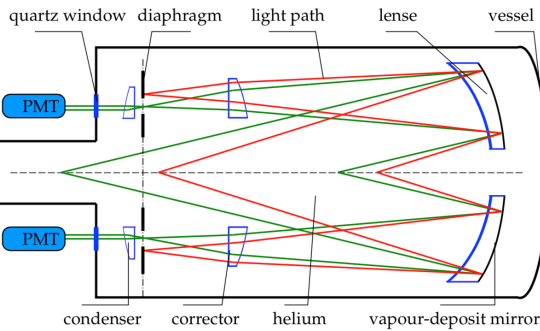


Figure 2.6: Light lines emitted inside CEDARs at COMPASS. The red(green) lines correspond to Cherenkov light emitted from a particle.

For years with a transversely polarized target, such as 2015, a chicane system of dipole magnets is setup in front of the target. The chicane first bends the beam away from the beam line and then back to the

target such that the beam hits the target at an angle. A chicane magnet setup is used because a beam hitting the target without any angle would then be deflected from the target magnet to the left or right of the spectrometer. For this reason the chicane gives the beam an angle before hitting the target such that the non-interacting beam exits the target traveling straight towards the spectrometer.

2.2 The Polarized Target

The polarized target at COMPASS is the most complicated and essential component of the spectrometer. It is located upstream of the tracking detectors and spectrometer magnets and downstream of the beam telescope, described in section 2.3, detectors. The target consists of two or three cylindrical cells. The possible materials are either solid state ammonia (NH_3) or deuterated lithium (${}^6\text{LiD}$) or liquid hydrogen. Fig. 2.7 shows a schematic of the target.

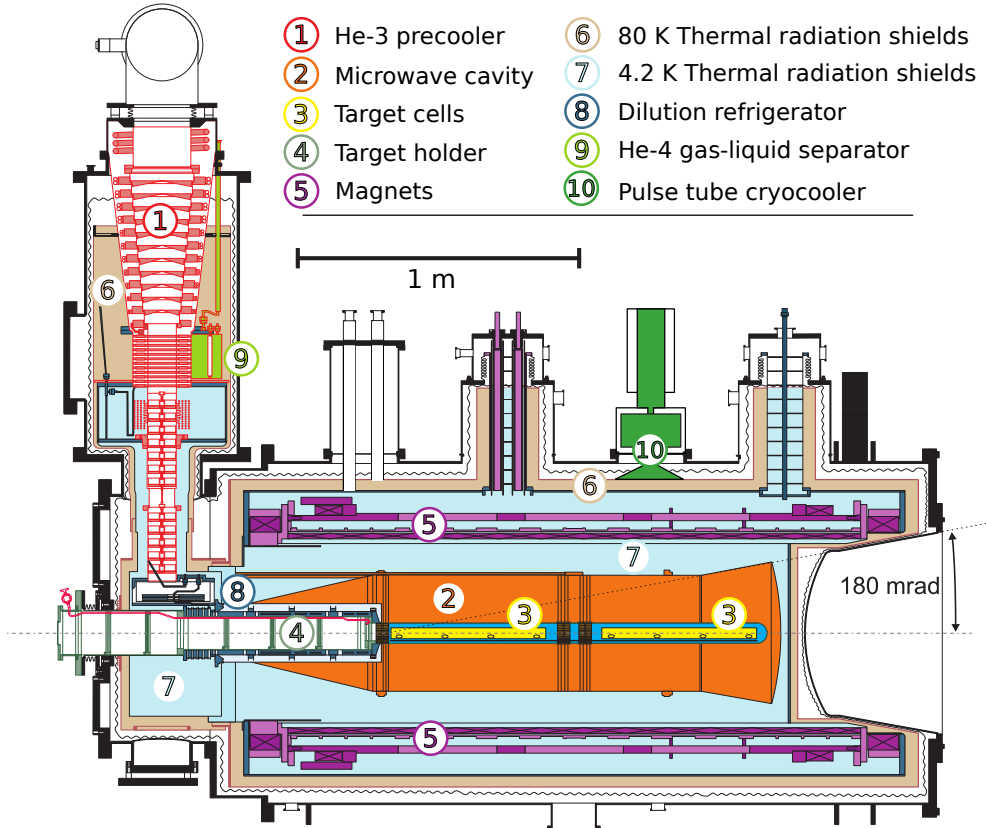


Figure 2.7: The polarized target at COMPASS

Surrounding the cylindrical cells is a longitudinal super conducting magnet capable of reaching a magnetic field of 2.5 T. This longitudinal magnet polarizes the target parallel or anti-parallel to the direction of the

beam momentum. The target polarization is maintained by keeping the target in a liquid helium bath of approximately 60 mK. This is called frozen spin mode where the temperature is maintained by a dilution refrigerator.

The target is polarized through the dynamic nuclear polarization (DNP) method [2]. This process works by first polarizing electrons in the target with the longitudinal magnet. With a high probability, the target electrons are all polarized in the same longitudinal direction for each target cells. Due to their much lower mass, electrons have a larger magnetic moment and therefore can be polarized at a much faster rate than protons or neutrons. At the same time the electrons are being longitudinally polarized, microwave electromagnetic radiation is sent through each target cell. For atoms which have a nuclear spin it is then possible for these atoms to absorb a microwave going to an excited state with the electron spin anti-parallel to the magnet and the nuclear spin either parallel or anti-parallel to the magnet depending on the microwave frequency. To ensure only one frequency enters each target cell, there is a microwave stopped between each target cell. The electron with the anti-aligned spin will then quickly have its spin realigned while the nucleon will take much longer to lose its polarization due to its smaller magnetic moment. This process can continue in this way resulting in a net nuclear polarization. Using the DNP method the target can achieve a polarization of approximately 90% in three days.

The target also includes a 0.63T transverse dipole magnet to change from longitudinal polarization to transversely polarized. The target must first be longitudinally polarized before the transverse target magnet can change the polarization direction. Once the target is transversely polarized, the target polarization can no longer be increased as microwaves can no longer shine on the target in the polarization direction. Therefore the polarization will decrease exponentially. In 2015 the target was polarized for about half a day between data taking sub-periods ad achieved an average polarization of 0.73%, including the effects of exponential polarization lose with time. The target transverse polarization relaxation time was about 1000 hours in 2015.

The target polarization was measured with 10 NMR coils while the target cells were longitudinal polarized. In the 2015, each target cell had the most upstream and downstream coils in the center of the target cell and the other three coils on the outside perimeter as is shown in Fig. 2.8. Due to the fact that the polarization can only be measured with the longitudinal magnet on, the polarization is only measure at the start and finish of a transversely polarized data taking. The intermediate polarization is then determined by exponential interpolating between these two times.

In 2015 the setup was two transversely polarized target cells of 55 cm length and 2 cm in radius. The cells were separated by 20 cm and polarized in opposite directions. The polarization of the target cells was flipped

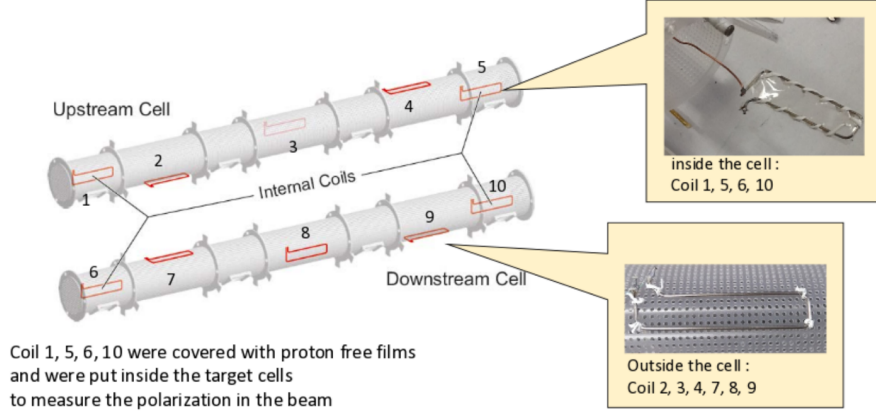


Figure 2.8: The empty polarized target cells side by side along with their NMR coil positions

ever two weeks of data taking to reduce systematic effects from luminosity and geometrical spectrometer acceptance. Due to the fact that the beam needs to be precisely steered onto the target and that the chicane magnets upstream of the target are setup for only one transverse target magnet direction, the transverse target magnet only pointed downward in 2015. To achieve a polarization flip the target polarization had to therefore be rotated back to the longitudinal direction and the input microwaves had to be changed to achieve the desired polarization direction.

The target material in 2015 was solid state NH_3 . The protons in the three hydrogen atoms were the only nucleons with nuclear spin and therefore only some fraction of the target was able to be polarized. The fraction of polarized nucleons to total nucleons is called the dilution factor. Counting the ratio of unpolarized nitrogen nucleons to polarized hydrogen, one would expect the dilution to be 3/17. However to get a more accurate determination of the dilution factor the follow calculation was used

$$f = \frac{n_H \sigma_{\pi^- H}^{DY}}{n_h \sigma_{\pi^- H}^{DY} + \sum_A n_A \sigma_{\pi^- A}^{DY}}, \quad (2.3)$$

where f is the dilution factor, n_H is the number of hydrogen atoms in NH_3 , n_A is the number of other nucleons in NH_3 , and $\sigma_{\pi^- H}^{DY}$ and $\sigma_{\pi^- A}^{DY}$ are the Drell-Yan cross-section for pion hydrogen scattering and

pion nucleon scattering respectively. The cross-sections were determined using a parton-level Monte-Carlo program MCFM [17]. The dilution factor was also further scaled down by studies of reconstruction migration between target cells. The average dilution factor in 2015 was determined to 0.18 in the invariant mass range of $4.3(\text{GeV}/c)^2$ to $8.5(\text{GeV}/c)^2$.

2.3 Tracking Detectors

To determine when and where a reaction occurs in the polarized target, tracking detectors are able to position the products of the reaction. The goal of the tracking detectors is to determine a point in space where a particle traversed. The COMPASS tracking detectors attempt to do this for a wide range of angles, momentums and at different rates. For these reasons there are several planar tracking technologies used at COMPASS which can be divided into three categories: very small angle tracker, small angle trackers and large area trackers. As the name suggest very small angle trackers measure tracks with small angle deflections from the beam axis which are essentially beam particles. The small area trackers measure particle tracks with low but non-zero scattering polar angle and have small central dead zones. The large area trackers are several meters in height and width and measures the largest deflection angles up to 180 mrad.

All of these trackers are split into stations. Each station corresponds to several detectors planes at roughly the same z-position along the beam line. Each station measures a track position in one or more orientation while most measure tracks in three or more orientations. The coordinate orientations measured are the X and Y coordinates which are the horizontal and vertical directions respectfully, and as well the U and V coordinates which are rotated at different angles with respect the X and Y coordinates.

2.3.1 Very Small Angle Trackers

The very small angle trackers extend up to 3 cm away from the beam axis. This is the region with the highest number of tracking particles and therefore these detectors must be able to handle the highest rates up to 5×10^7 Hz. The two detector types that make up the very small angle trackers are either scintillating fiber detectors (SciFi) or silicon microstrip detectors. These two detector types are complementary to each other as the former have very good timing resolution while the latter have very good spacial resolution.

There are three silicon stations possible at COMPASS. These stations have active detecting areas of $5 \times 7 \text{ cm}^2$. The spacial resolution of these detectors is nominally $10 \mu\text{m}$ and the timing resolution is nominally 2.5 ns. For the 2015 setup, the beam intensity was too high for the silicon detectors to operate and therefore these detectors were not used.

There are 10 SciFi stations available at COMPASS. The active areas vary from $3.9 \times 3.9 \text{ cm}^2$ to $12.3 \times 12.3 \text{ cm}^2$ planar areas. As well the detection fiber diameters vary between detectors with the different diameters used at COMPASS being 0.5 nm, 0.75 nm and 1 nm. Several fibers are bundled together to determine a strip hit position and the resulting nominal spacial resolutions are $130 \mu\text{m}$, $170 \mu\text{m}$ and $210 \mu\text{m}$. The nominal timing resolution of these detectors is about 400 ps. In 2015 three SciFi stations made up the beam telescope and were placed upstream of the target to measure the beam trajectory and timing information. A fourth SciFi station was place in the LAS section of the spectrometer.

2.3.2 Small Angle Trackers

The small angle trackers detect particles with non-zero deflection angles. These detectors have medium size active areas compared to the very small angle trackers and the large angle trackers. They cover 5 cm to 40 cm from the beam axis where the rate drops to approximate 10^5 Hz , two orders of magnitude lower than the rates the very small angle trackers receive. At COMPASS there are two types of small area tracking detectors: micromesh gaseous structure (micromegas) and gas electron multipliers (GEMs).

There are three micromega stations at COMPASS. All three stations are location sequentially after each other between the target and the first spectrometer magnet. As well all three detectors measure four coordinate projections and have an active area of $40 \times 40 \text{ cm}^2$ with a 5 cm diameter dead zone. The micromegas operate by having a conversion region and a smaller amplification region. An ionized particle produced in the conversion region will drift through an electric field of around 3.2 kV/cm to the amplification region where the electric field is around 50 kV/cm . The electric field is too small for amplification in the conversion region but as the name suggest the electric field is high enough to amplify the signal in the amplification region. The amplified signal is then read out on strips. The conversion and amplification regions are separated by a metallic micromesh material. The electrons pass through the micromesh without resistance and are not rimmed out. The micromegas have good spacial resolution because the thickness of the amplification region is only $100 \mu\text{m}$, small enough to prevent much transverse spreading of the electron avalanche between strips. The separation of the larger conversion region from the smaller amplification region with the micromesh prevents electric field lines from being distorted in the conversion region and therefore prevents the primary electrons from drifting slower in the conversion region. This allows micromegas to operate at a higher rate than would be possible otherwise. This principle of operation is illustrated in Fig. 2.9. The strips in the central part of the detector are $360 \mu\text{m}$ corresponding to a resolution of about $100 \mu\text{m}$ and the strips in the outer region are $460 \mu\text{m}$ corresponding to a resolution of about $120 \mu\text{m}$. The nominal timing resolution 9 ns. In 2015 the micromegas were upgraded to include a pixelized section covering much of the dead zone area.

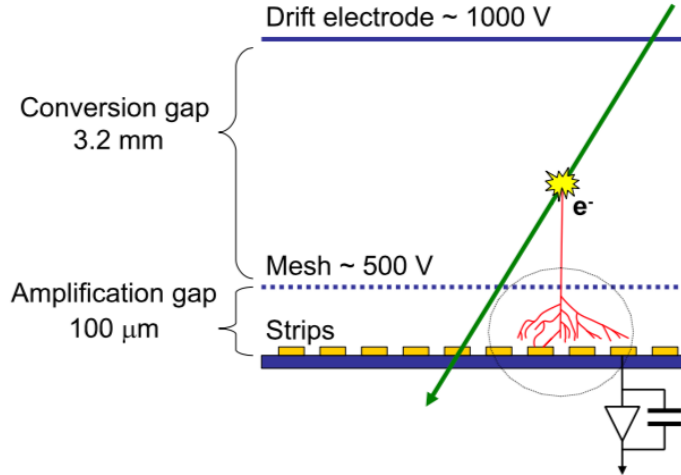


Figure 2.9: Principle of operation for the micromesh gaseous structures (micromegas)

There are eleven GEM detectors located throughout the COMPASS spectrometer. The first GEMs are located after the first spectrometer magnet and the last GEMs are located near the end of the spectrometer. These detectors are positioned close to the beam axis. They are mounted on a large area tracker, covering the dead zone region of the large area tracker. All eleven detectors have an active area of $31 \times 31 \text{ cm}^2$ and a 5 cm diameter dead zone. In times of lower beam intensity the dead zones can be turned on as an active area.

The detector is split into four regions. These regions are separated by a polyimide foil (50 μm thick) having around 10^4 cm^{-1} drifting holes of 70 μm diameter and are clad with copper on both sides. There is an electric potential of a few hundred volts between each foil layer. The electron amplification occurs around the holes of each of the three foil dividers. This means GEM detectors speed up the amplification process by splitting the amplification avalanche into three locations. The process is sped up because the drifting electrons are accelerated multiple times thereby speeding up their drifting velocity which therefore reduces the overall drift time from the ionization location to the strip readout. This allows the GEMs to operate at a higher rate than would otherwise be possible. The principle of operation is illustrated in Fig. 2.10. The nominal timing and spacial resolution of the GEM detectors is 10 ns and 110 μm respectively. Two pixelized GEM detectors were also in operation but were not as crucial for the 2015 Drell-Yan measurement.

2.3.3 Large Area Trackers

The large area trackers measure the largest polar scattering angles at COMPASS. Their dead zones mostly coincide with a small area tracker, described in the previous section 2.3.2, which therefore means these

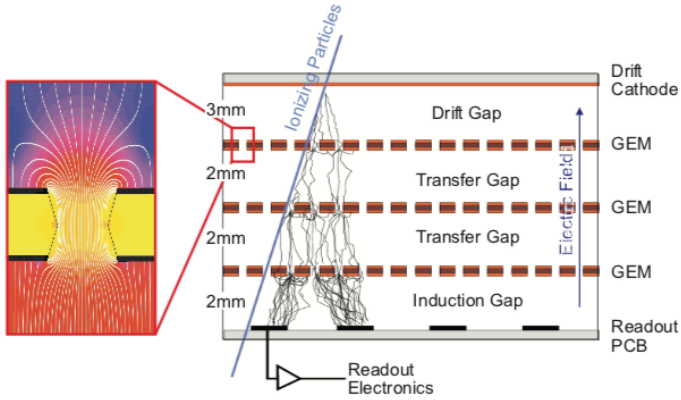


Figure 2.10: The operation principle of the gas electron multiplier (GEM) detectors

detectors do not have to process the higher fluxes very close to the beam line. The most important feature of these detectors is that they have a large planar area. As a consequence however, their position and timing resolutions are not as good as the small and very small angle trackers. The types of large area trackers used at COMPASS are all gaseous detectors and include drift chambers (DCs), straw tube detectors (straws) and multi-wire proportional chambers (MWPCs).

The first four drift chambers downstream of the target are named DC00, DC01, DC04 and DC05. The first two, DC00 and DC01, have smaller active areas of $180 \times 127 \text{ cm}^2$ and a circular dead zone of 30 cm diameter. These two drift chambers are positioned upstream of the SM1 magnet. The rates upstream of SM1 are higher. This is due to the fact that low energy particles are produced in the target, but are bent out of the acceptance of spectrometer by SM1. Therefore detectors downstream of SM1 do not track these low energy particles and therefore DC00 and DC01 need to be able to process a higher particle flux. The next two drift chambers, DC04 and DC05, are downstream of SM1 and both have larger active areas of $240 \times 204 \text{ cm}^2$ and as well have dead zones of 30 cm diameter. The active areas of all four of these DCs was roughly chosen to coincide with the acceptance of the SM1 yoke. DC05 was first installed for the 2015 Drell-Yan data taking and is further described in chapter 3. All four of these DCs measure four projection views corresponding to eight detector layers. A sketch of the principle of operation is shown in Fig. 2.11. The nominal spacial resolution for these detectors is $250 \mu\text{m}$.

Further downstream the spectrometer, downstream of the SM2 magnet, are the W45 drift chamber stations. The W45 drift chambers are the largest drift chambers at COMPASS. There are six W45 detector stations which each have an active area of $520 \times 260 \text{ cm}^2$ and a circular dead zone of 50 cm or 100 cm diameter.

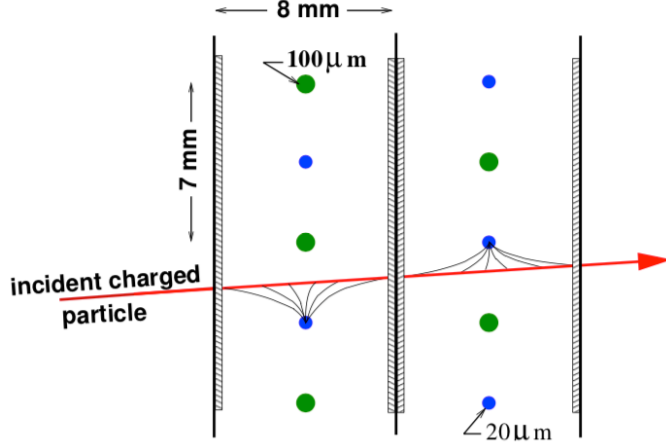


Figure 2.11: Drift cell of a drift chamber with the ionized drift electron lines coming from the incident charged particle

Each W45 station measures two projection views corresponding to four detector layers. The drift cells in W45 are $40 \times 10 \text{ mm}^2$ and the spacial resolution is nominally $1500 \mu\text{m}$.

The two straw stations in operation during the 2015 data taking are named ST03 and ST05. ST03 was in the large angle spectrometer after DC05 and consisted of two stations measuring six projection views. ST05 was in the small angle spectrometer and measured three projection views. The active areas of each of the horizontal wire stations is $350 \times 243 \text{ cm}^2$ and the active area of each of the rotated wires is $323 \times 272 \text{ cm}^2$. The principle of operation for the straw detectors is very similar to that of a drift chamber. However, instead of having the detector made up of connected drift cells the straw detectors are made of separated circular tubes. Each tube consist of a gold plated tungsten anode wire in the center and the walls of the tube make up a cathode. Due to the fact that the cathode completely surrounds the anode wire there is no electrical interference between neighboring anode wires as there is for drift chambers. For this reason the electric field in each tube is easier to control and the ionized electron drift speed is more linear than other detectors. Each straw detector plane is divided into sections where the straw tubes in the outer most section from the beam line have a diameter of 9.6 mm and the tubes close to the beam line have a diameter of 6.1 mm. In addition, in the central part of the detector there is a physical hole, dead zone of $20 \times 20 \text{ cm}^2$. The nominal position resolution for these detectors is $400 \mu\text{m}$. A frontal schematic is shown in Fig. 2.12. For the reason that most of the detected muons are reconstructed in the large angle spectrometer and the fact that many of the high voltage modules were not operation for ST05 in 2015, ST05 was not used for track reconstruction for 2015 Drell-Yan data.

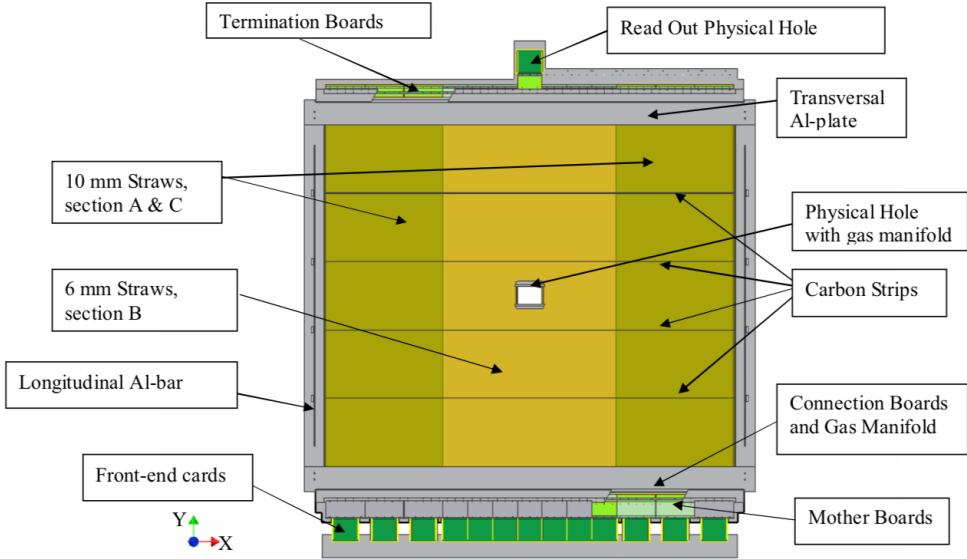


Figure 2.12: Front on view of a the active area of a straw detector at COMPASS

The next type of large angle track is the richwall. This large area tracker operates similarly to the straw tube detectors. The detector consist of eight layers of mini drift tubes (MDT) shown in Fig. 2.13. The central part of each MDT includes a gold plated tungsten sense wire. The richwall is located before the SM2 magnet and after ST03 with an active area of $5.27 \times 3.91 \text{ cm}^2$ and a central dead zone of $1.02 \times 0.51 \text{ cm}^2$. The nominal position resolution of this detector is $600 \mu\text{m}$.

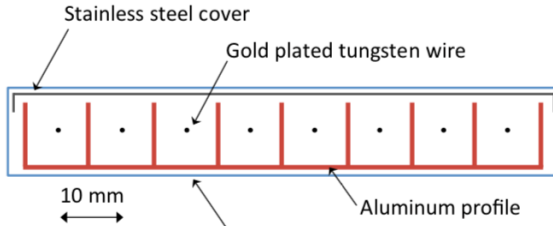


Figure 2.13: The richwall mini drift tubes

The final type of large area tracking detector at COMPASS is the MWPC. There are 14 of these stations located throughout the experiment. The MWPCs are separated into three categories distinguished by the coordinates they measure. The first type is called type A and consists of three projection views measuring an x, u and v coordinate. The second type is type A* and is the same as type A but measures the y coordinate in addition to the other three coordinates. Both type A and A* have active areas of $178 \times 120 \text{ cm}^2$. The final type is type B which has a smaller active area of $178 \times 90 \text{ cm}^2$ and measures the same projections as type A.

There are seven stations of type A, one station of type A* and six stations of type B. All three types have circular dead zones of diameters 16 cm, 20 cm and 22 cm for types A, A* and B respectively.

The MWPCs operate on similar principles to the drift chambers but without a calibration drift curve. For this reason the MWPCs can be made to have one common gas volume between each station. Their position resolution is determined as

$$\frac{\text{sense wire separation}}{\sqrt{12}}, \quad (2.4)$$

which is the variance of a uniform distribution. The separation between sense wires is approximately 2 mm which corresponds to a spacial resolution of these detectors of around 600 μm .

2.4 Particle Identification

In the COMPASS spectrometer there are four types of detectors used to determine particle identification (PID). These four detectors are the ring image Cherenkov (RICH) detector, electromagnet calorimeters (ECAL), hadron calorimeters (HCAL) and muon walls (MW). The RICH distinguishes between pions, kaons and protons; ECAL1 and ECAL2 measure the energy from photons and electrons; HCAL1 and HCAL2 measure the energy from hadrons; and MW1 and MW2 distinguish muons from all other particles. The RICH, ECAL1, HCAL1 and MW1 are in the large angle spectrometer in that respective order along the beam line. The small angle spectrometer includes ECAL2, HCAL2 and MW2 again in that respective order along the beam line.

The RICH detector operates similarly to the CEDARS, section 2.1.3. In the RICH, Cherenkov radiation is emitted from particles traveling through it at an angle dependent on the particle's velocity. The RICH is filled with a dielectric gas, C_4F_{10} , which has an index of refraction greater than air. The momentum of a particle going through the RICH is determined from bending radius around SM1. Therefore once the RICH determines the entering particle's velocity, the mass of particles can be distinguished. A sketch of the RICH and its operating principle is shown in Fig. 2.14. To distinguish between particles the minimum momenta are: 2.5 GeV/c for pions, 9 GeV/c for kaons and 17 GeV/c for protons. The maximum momentum the RICH can distinguish between any of these particles is 50 GeV/c . This detector is located in the large angle spectrometer before any calorimeters.

The ECALs and HCALs both measure the energy of entering particles. Both types of calorimeters do this by stopping a specific entering particle, where the amount of energy deposited in each respective calorimeter is proportional to the incoming particle's energy. ECALs are able to stop and measure electron and ph-

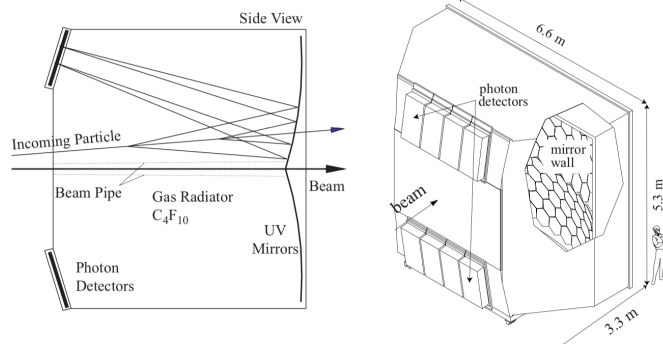


Figure 2.14: Side view demonstrating the principle of operation of the RICH detector.

ton energies and HCALs stop and measure hadron energies. The energy knowledge along the momentum determined from the tracking detectors allows the ability to determine the particle's identification.

The ECALs are made of lead glass towers with photon multipliers attached to these towers on one side. An incoming photon or electron interacts with the lead glass to produce a light signal which is readout with these photon multipliers. Other particles also interact with the material in the ECALs however hadrons and muons are able to exit through the detector unlike photons and electrons. A frontal view of ECAL1 is shown in Fig. 2.15 and a frontal view of ECAL2 is shown in figure Fig. 2.16.

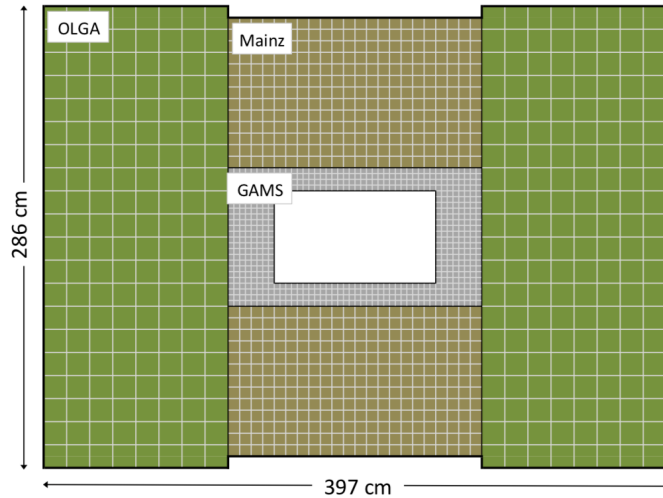


Figure 2.15: Frontal view of the electromagnetic calorimeter 1

The HCALs are sampling calorimeters which are made of alternating layers of iron and scintillating material. An incoming hadron deposits all its energy in the HCAL by making a particle showers in the iron. This particle shower makes a signal in the scintillating material which is then read out by photo multipliers. The HCALs are placed after the ECALs in each stage of the spectrometer because an electromagnetic shower happens within less material budget than a hadronic shower. The HCALs are effect at determining particle

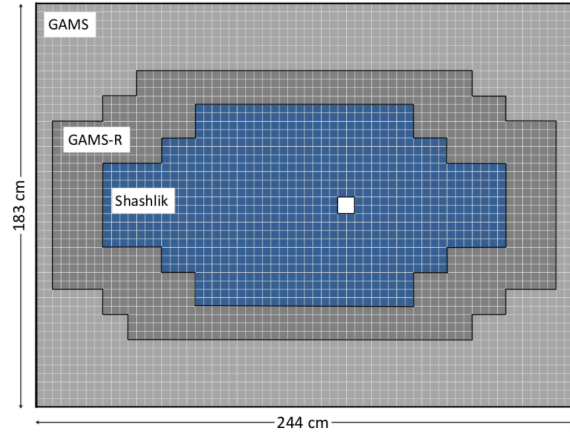


Figure 2.16: Frontal view of the electromagnetic calorimeter 2

energies from particle with energies between 10 GeV and 100 GeV.

The two MWs are located after an HCAL in their respective stages. Due to their higher mass and absence of color charge, muons are able to pass through the most material budget of any of the particles detected at COMPASS. For this reason both MWs consist of an absorber and tracking detectors downstream of this absorber. Any particles that make it through the absorber are with a very high probability muons.

MW1 consists of eight tracking planes before a 60 cm iron absorber and the same number of tracking planes after this absorber. The tracking portions of MW1 are built similarly to the richwall, described in section 2.3.2, in that they are also made of MDT modules. The active area of MW1 is $480 \times 410 \text{ cm}^2$ and includes a dead zone of $140 \times 80 \text{ cm}^2$. Each plane of this detector has a spacial resolution of 3 mm. A sketch of MW1 is shown in Fig. 2.17.

The second muon wall, MW2, is located downstream of a 2.4 m thick concrete absorber. MW2 consists of 12 planes each with an active area of $450 \times 450 \text{ cm}^2$ and a dead zone of $90 \times 70 \text{ cm}^2$. The detector operates similarly to the straw detectors, section 2.3.2, in that the detector is made of drift tubes with a wire in the center of these tubes. The diameter of the drift tubes is 29 mm and the position resolution is about 1.4 mm.

There is one last absorber in the COMPASS spectrometer located before the H5 hodoscope at the end of the spectrometer hall. This absorber is called muon filter 3 (MW3) and ensures that the inner trigger is only triggered by a muon.

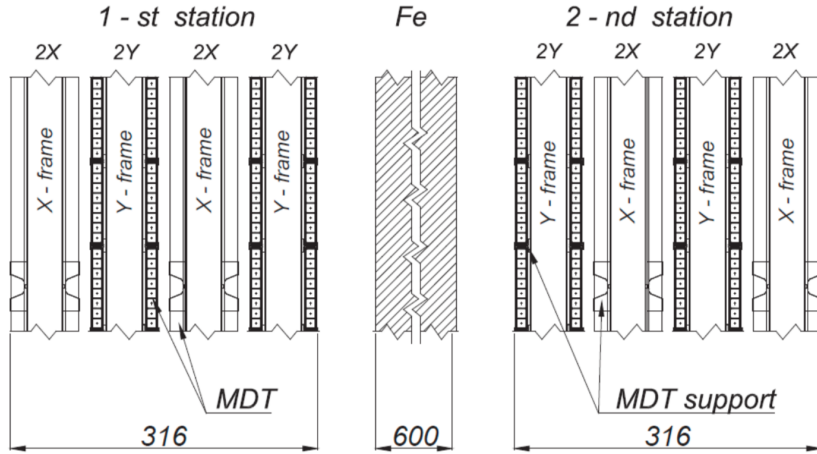


Figure 2.17: A side view sketch of the muon wall 1 detector

2.5 Trigger

The trigger system at COMPASS defines what is an event. Whenever the trigger signal is given, all the detector information within a few nanosecond timing window is recorded. Due to the fact that there are very many background events occurring as the beam impinges on the target, there is too much information going to the front end modules (FEMs) of the detectors for the FEMs to process and record all this information. For this reason only a certain subset of all the information is stored to disk. The trigger system must therefore have good timing resolution to make quick decisions on which data to record. At COMPASS the trigger systems consist of scintillating hodoscopes attached to PMTs. The timing resolution of these detectors is approximately 1 ns. A top view schematic of COMPASS showing where the relative positions of the hodoscopes for each trigger is shown in Fig. 2.18.

At COMPASS there are five different triggers used to register physics events. Each trigger type includes at least two hodoscopes at different z-positions in the spectrometer. The types of triggers are either target pointing, when the hodoscope slabs are horizontal; or energy loss, when the hodoscope slabs are vertical. The target pointing trigger is setup and used with higher polar scattering angles. As the name suggest, this trigger signals when a particle is scattered from the target. The energy loss trigger is used to trigger on lower Q^2 interactions and signals when a particle is bent a specified amount. This concept is illustrated in Fig. 2.19.

There are four triggers in SAS: the inner trigger (IT), the middle trigger (MT), the ladder trigger (LT) and the outer trigger (OT). The IT is an energy loss trigger and includes the hodoscopes HI04X and HI05X. The MT includes both energy loss and target pointing slabs. The hodoscopes in the MT are HM04X,

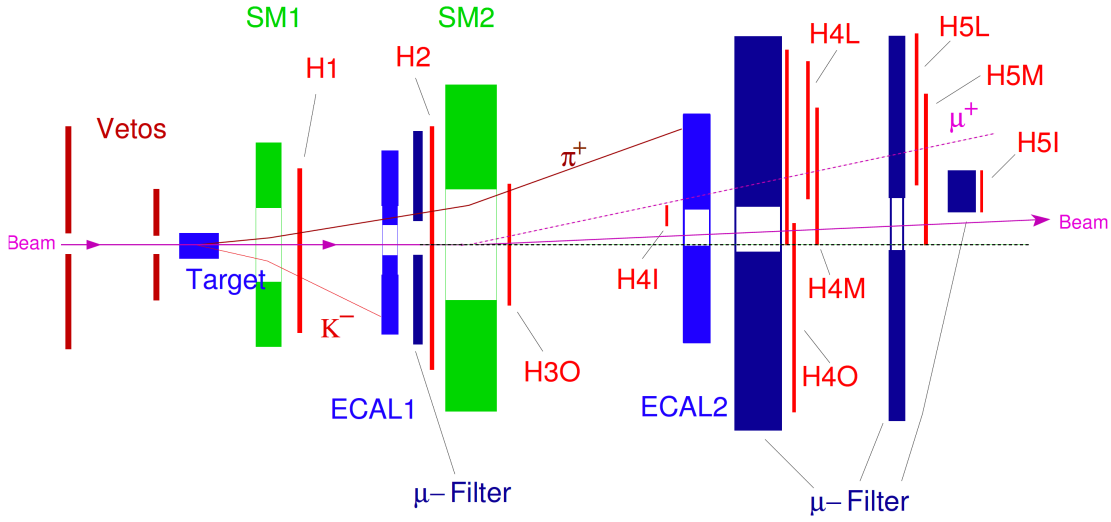


Figure 2.18: Top view of the spectrometer highlighting how different particles can signal a trigger

HM05X, HM04Y and HM05Y. The MT hodoscopes whose names end with an X have vertical slabs and those ending with a Y have horizontal slabs. The LT is an energy loss trigger which consists of HL04X and HL05X. The final trigger in SAS, the OT, is a target pointing trigger and consists of hodoscopes HO03Y and HO04Y. The remaining trigger system is in LAS and is a target pointing trigger consisting of hodoscopes HG01Y and HG02Y. The kinematic coverage for the 2015 triggers is shown in Fig. 2.20.

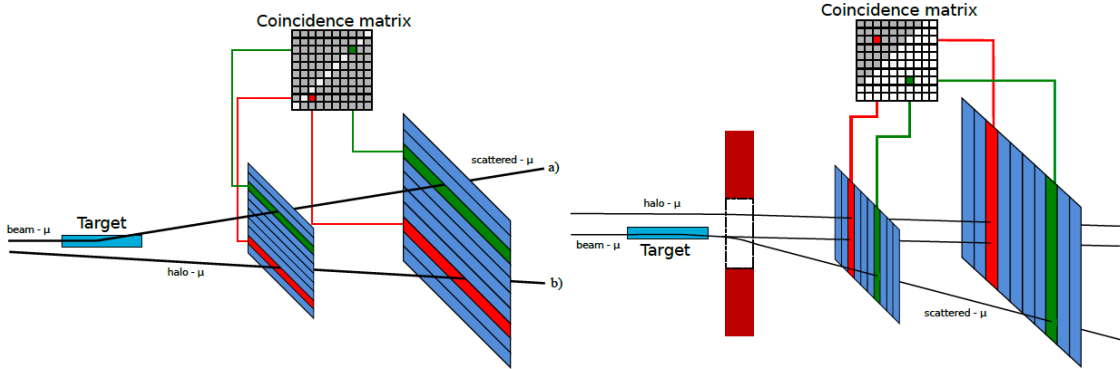


Figure 2.19: The two types of triggers (left is target pointing and right is energy loss) at COMPASS and an illustration of the coincidence matrix used to select events of interest

In addition to signaling when interesting events occur, it is also important to signal when background events are occurring. For this reason there is also a veto system upstream of the target as shown in Fig. 2.18. This veto trigger consists of hodoscopes attached to PMTs as well. It is centered on the beam axis but has a hole center on the nominal beam line. The veto trigger is used to reject halo muons which surround the beam.

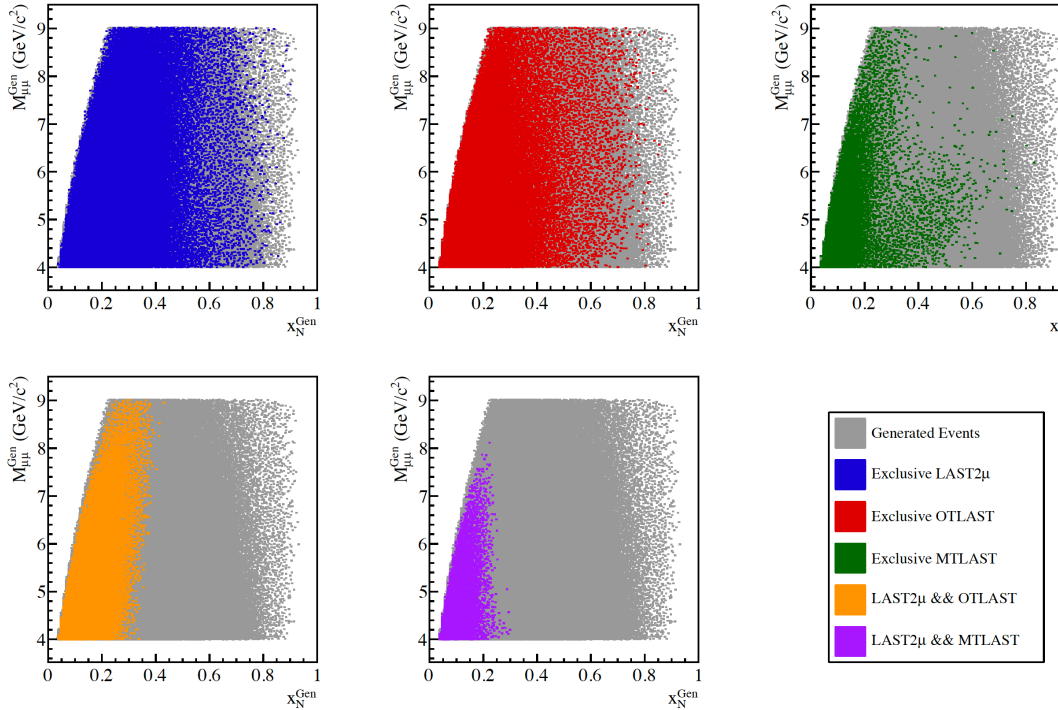


Figure 2.20: The kinematic coverage for the 2015 triggers determined from Monte-Carlo studies

Halo muons result from the beam decaying, as in Eq. 2.1 and Eq. 2.2, where this decay occurs upstream of the target but downstream of the ABS absorbers. The muon halo surrounds the hadron beam due to the muon's lower momentum, and it is for this reason that the veto hodoscopes, outside of the beam line, are able to reject events that would occur due to the halo.

There is one trigger in the spectrometer hall that is not a hodoscopes. This is the calorimeter trigger (CT). The CT can be used as a trigger when a particle deposits more than a certain energy threshold in the specified calorimeter. In 2015 this trigger was only used as an independent study of the other triggers at COMPASS. Particularly the CT was used to measure the trigger hodoscopes efficiencies.

The last trigger used at COMPASS is a random trigger. This trigger is setup outside of the spectrometer area and registers a signal when a radioactive source disintegrates. In this way the random trigger is truly random. In 2015 this trigger was used in studies of the beam flux.

In 2015, the goal was to measure two muons in the spectrometer. For this reason, two triggers must each signal a particle in coincidence for an event to be registered. For physics analysis the coincidence triggers are either two muons in LAS (LASxLAS), one muon in LAS and one in the OT (LASxOT) or one muon in LAS and one muon in the MT (LASxMT). The LASxLAS trigger system covers the high Q^2 and high x_{beam} phase space whereas the triggers including a SAS hodoscope cover lower Q^2 values. In addition to

these three dimuon triggers where three single muon triggers corresponding to a particle in LAS, MT or OT. These three single muon triggers, however, were pre-scaled down to only take every 500, 100 or 100 events respectively. For further tests 2015 included a random trigger and a beam trigger pre-scaled down by 35000.

2.6 Data Acquisition

The data acquisition (DAQ) collects data from the over 250,000 detector channels and transfers this data to storage on magnetic tape at CASTOR (CERN Advanced STORage). Despite the triggering system used to reduce the data rate, the data still is recorded at event rates between 10 kHz to 100 kHz. A typical COMPASS event size is 45 kB. The DAQ is designed to process these data rates and size while minimizing the dead time associated with data collection and transfer. In 2015 the dead time was approximately 10%. The total data the DAQ recorded, after the spectrometer finished commissioning, was approximately 750 terabytes of raw data.

Data collection begins with the digitization of information from a detector channel. This digitization is performed by a time to digital converter (TDC) or an analogue to digital converter (ADC). These TDCs and ADCs are either on the detector FEMs or on custom COMPASS readout electronics named: GANDOLF (Generic Advanced Numerical Device for Analog and Logic Functions), GeSiCA (Gem and Silicon Control and Acquisition) or CATCH (COMPASS Accumulate Transfer and Control Hardware). After digitization the data is transferred by optical fibers to an FPGA multiplexer where the data is buffered by spill and arranged by event. From there an FPGA switch sends the data to multiplexer slaves. The slaves are online computers that oversee the final steps for raw data and transfer this data to CASTOR. This whole process is shown schematically in Fig. 2.21.

2.7 Data Reconstruction

The COMPASS Reconstruction and AnaLysis Program (CORAL) reconstructs the raw data into physical quantities. For example CORAL is able to convert the raw data into particle tracks with momentum, charged and possibly an originating vertex location [7]. The raw data from the DAQ is digitized timing information from tracking detectors or digitized energy information for calorimeters. The process of reconstructing tracks takes the detector timing information and determines a position in space for a particular tracking detector based on a calibration. CORAL then uses a Kalman Filter to determine straight tracks in regions with no or low magnetic field [25]. The tracks are then connected through the magnetic field using a fast lookup table for known possible bending radii. At this point a track is determined to have a momentum, charge

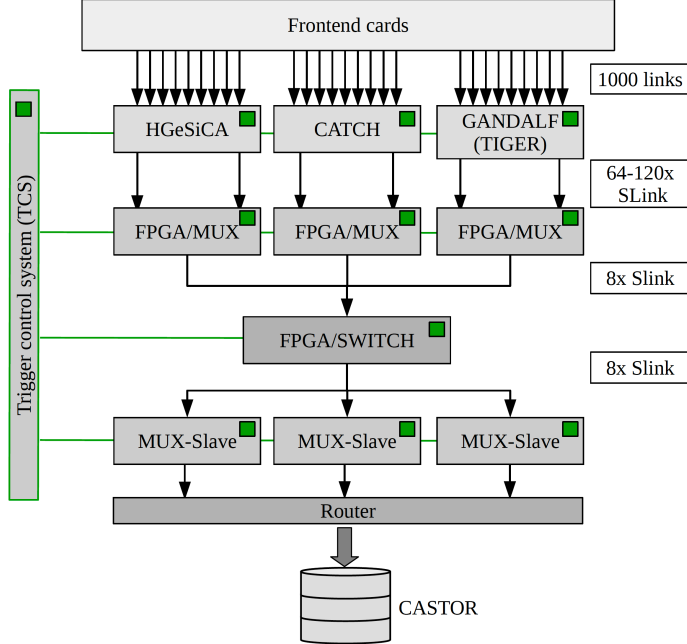


Figure 2.21: The data acquisition steps at COMPASS

and a χ^2 value associated with the track. From there the tracks are extrapolated back to the target region and the intersection of at least two tracks is determined as a vertex. If in addition to the two intersecting tracks, a beam particle can be extrapolated forward to the same vertex location then the vertex is assigned to be a primary vertex. Otherwise the vertex is defined as a secondary vertex.

This reconstruction stage reduces the data volume by approximately a factor of 10. A diagram of the reconstruction data flow is shown in Fig. 2.22. In 2015 there were several data reconstructions performed. Between each reconstruction improvements were made to detector calibrations, detector alignment, beam tracking and any other preprocessing improvements that could be made. The final two productions are the t3 production and the slot1 production. The results shown in this thesis are from either t3 or slot1 productions.

Once reconstruction has been performed the data is stored in data structured trees (DSTs). The usual procedure of reconstruction which gives physical values such as momentum and charge to tracks, results in data called miniDSTs. There is also the possibility to save more information, for example detector hit location information, to make so called fatDSTs. These DSTs are now in a format which can be processed by PHAST (PHysics Analysis Software Tool). PHAST is a COMPASS program written to further analyze physics data. With PHAST there is the possibility to loop over all the miniDSTs and make certain cuts and to produce a so called μ DSTs based on these cuts. In 2015 μ DSTs were made for all the analysis data where a cut was applied to the miniDSTs saving only events with at least two muons. Both CORAL and

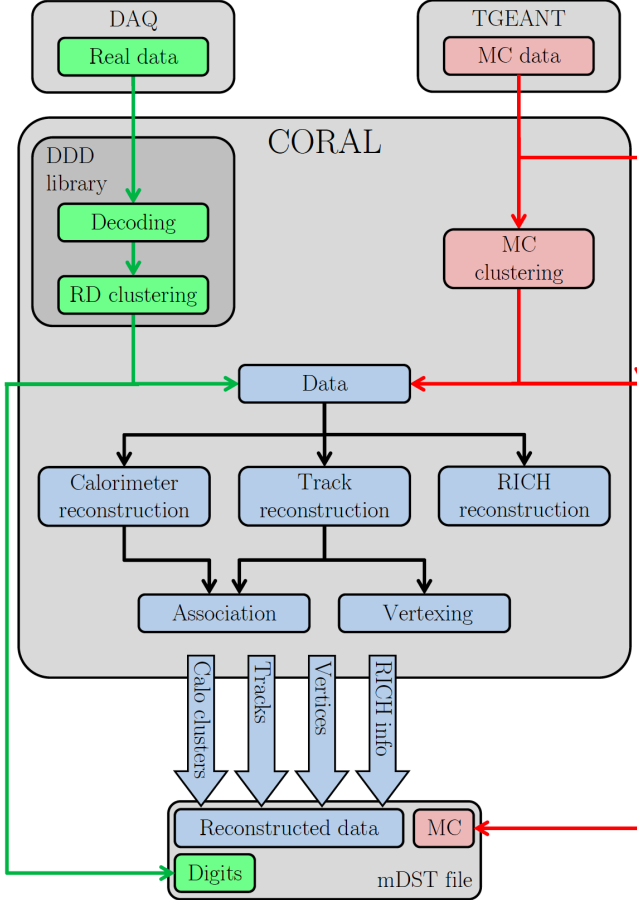


Figure 2.22: The schematic of the CORAL reconstruction process

PHAST are fully object-oriented C++ programs.

2.7.1 Monte-Carlo Production

Monte-Carlo data is simulated data which is performed in three steps. First a programs generates specific physics processes based on their theoretical probabilities. The generators of Monte-Carlo used for this thesis are PYTHIA versions 6 and 8 [37]. Next a GEANT4 simulation of COMPASS determines if a detector will register a hit from these generated physics processes. This saves the data in a raw data format which can be reconstructed by CORAL. Finally the simulated data is reconstructed by CORAL and analyzed in PHAST the same as if the data were real data.

2.8 2015 Drell-Yan Data Taking

The 2015 Drell-Yan data taking is one of the main programs for the COMPASS-II experiment. The data taking began in April of 2015 and ended in November of that year. The physics data used for analysis started in July and finished at the end of data taking. The data recorded before July was used for calibrations and commissioning. The total analysis data was split into nine data periods labeled W07-W15 where each data period corresponded to approximately two weeks of beam time. The spin orientation of each target cell was reversed after the first week of every period to reduce systematic effects arising from different geometric acceptances and luminosities of the up and downstream target cells.

2.8.1 Hadron Absorber

The previous sections in this chapter described the spectrometer setup generally and mentioned the specifics for the 2015 setup. The main unique hardware addition in 2015 is the hadron absorber. The hadron absorber was installed because the beam intensity is high and results in many main strong interactions in the target. For this reason the first tracking detectors upstream of SM1 have occupancies which are too high for tracking. Therefore the hadron absorber was installed to prevent all particles except muons from entering the spectrometer.

The hadron absorber was placed just downstream of the two target cells as can be seen in Fig. 2.23. The absorber corresponded to approximately 7.5 interactions lengths of material where the material was mostly alumina (Al_2O_3) and concrete. Inside the absorber was an aluminum target followed by a tungsten plug, each of radius 2.5 cm. The tungsten was used as a beam dump while the aluminum was present to prevent back scattering from the tungsten beam plug. A side view showing the dimensions and materials used can be seen in Fig. 2.24. Both the aluminum target and tungsten plug served the double purposes as absorbers and also as unpolarized nuclear targets. In addition to the hadron absorber two thin ${}^6\text{Li}$ absorbers were added just downstream of the primary absorber to absorb thermal neutrons produced in the primary absorber. This ${}^6\text{Li}$ absorber was proposed to improve the performance of the first tracking detector downstream of the target even with the hadron absorber installed.

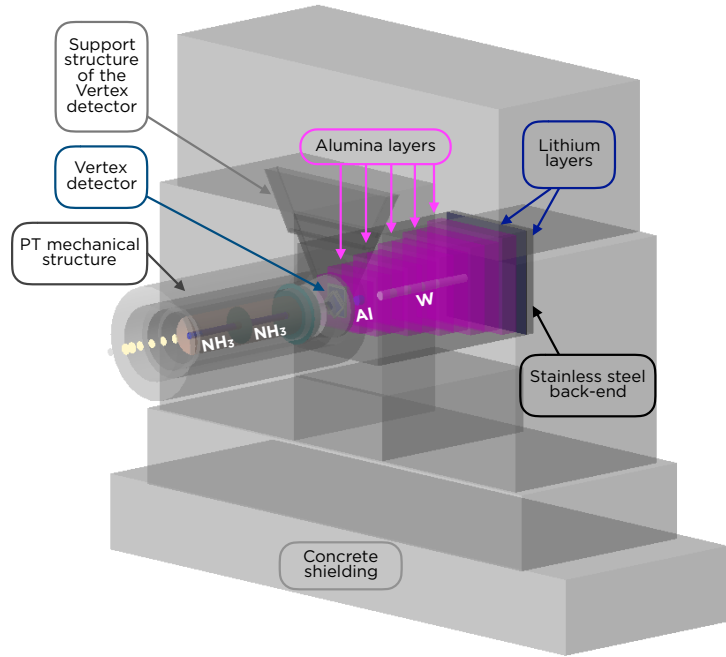


Figure 2.23: The hadron absorber downstream of the polarized target in 2015

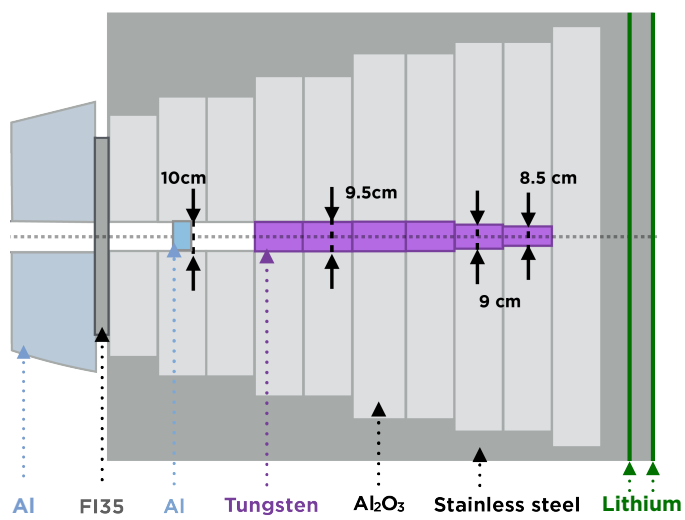


Figure 2.24: Side view of the hadron absorber used in 2015

Chapter 3

Drift Chamber 05

Drift Chamber 05 (DC05) is a large-area planar drift chamber. It was constructed in 2014 and 2015 at the University of Illinois and Old Dominion University and was then shipped to CERN for final assemble. DC5 was installed to the large angle spectrometer of COMPASS during the spring of 2015.

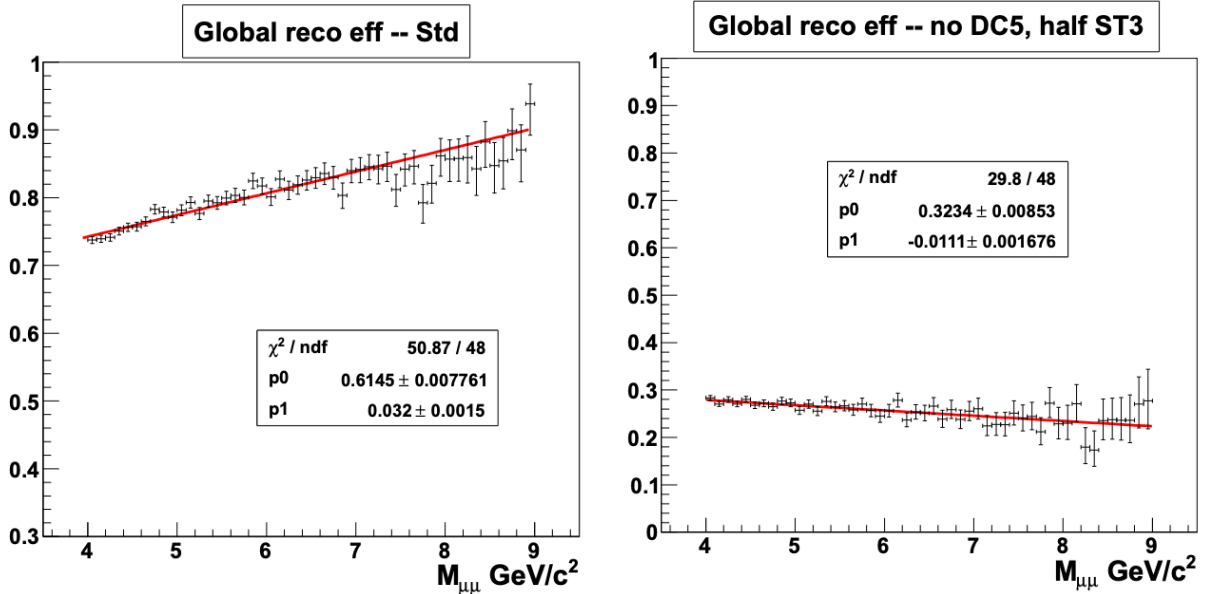
The DC5 detector is an import tracking detector, which successfully collected data from 2015 through 2018 and will continue to be an important component for track reconstruction in future measurements. The author of this thesis helped with the construction at Illinois and the assembly at CERN and as well for performing calibrations and maintaining DC5.

3.1 Motivation for Drift Chamber 05

Simulations of the COMPASS spectrometer for Drell-Yan measurements determined that 96% of all events include a track in the large angle spectrometer [26]. For this reason the Drell-Yan trigger system was designed only to record events with at least one track in LAS. As DC5 was installed in LAS it is therefore very important in track reconstruction for Drell-Yan measurements. Additional simulations with the Drell-Yan setup and this corresponding COMPASS Drell-Yan trigger showed that the global reconstruction efficiency drops below 30% without DC5 and half of another large area tracker in LAS [33]. That is to say the spectrometer reconstruction efficiency is very poor without DC05 and half of another LAS large area trackers which has unstable performance. Fig. 3.1a and Fig. 3.1b show the nominal global reconstruction efficiency and the worst case scenario for Drell-Yan measurements respectively. For these reasons it was very important to have DC05 installed and working reliably.

3.2 Operating Principle

Drift chambers are tracking detectors which can detect the location of where a high energy charge particle passes through them. A drift chamber is built up of an array of drift cells where at the center of each drift cell is an anode signal wire (also called a sense wire). Surrounding the signal wire are cathodes which close



(a) Global reconstruction efficiency with all detectors working. This image was taken from [34]

(b) Global reconstruction efficiency without DC05 and half of another LAS large area tracker. This image was taken from [34]

off the drift cell. The cathodes are set at a higher high voltage than the anode and therefore there are electric field lines from the cathode to the anode. Fig. 3.2 shows an example of a drift chamber cell and the equipotential voltages within the cell. In DC05 the there are two cathode planes on top and bottom of the drift cell and a cathode field wire adjacent to either side of the sense wire.

Between the anodes and cathodes of a drift cell is a gas mixture. The high energy charged particles which enter the chamber ionize this gas mixture. For each track passing through the chamber, multiple primary ionization electrons are produced and these electrons drift to the signal wire. The number of primary ionization electrons produced however, is not enough to create a detectable signal on the sense wires. For this reason the electric field increases as the inverse of the distance from the sense wire which allows the primary ionization electrons to gain enough energy to further ionize the gas and ultimately produce an electron avalanche near the sense wire. The signal created from this electron avalanche is strong enough to detect. A typical detector is built so that an avalanche can occur before the sense wire but not before a cathode wire. This is accomplished by constructing the chamber with sense wires having a much smaller diameter than the field wires, meaning the electric field near the sense wire can be much larger than the electric field near the field wire.

An important factor for a drift chamber is that the location of the primary ionized electrons can be determined within a drift cell. This knowledge allows for a better position determination of the passing

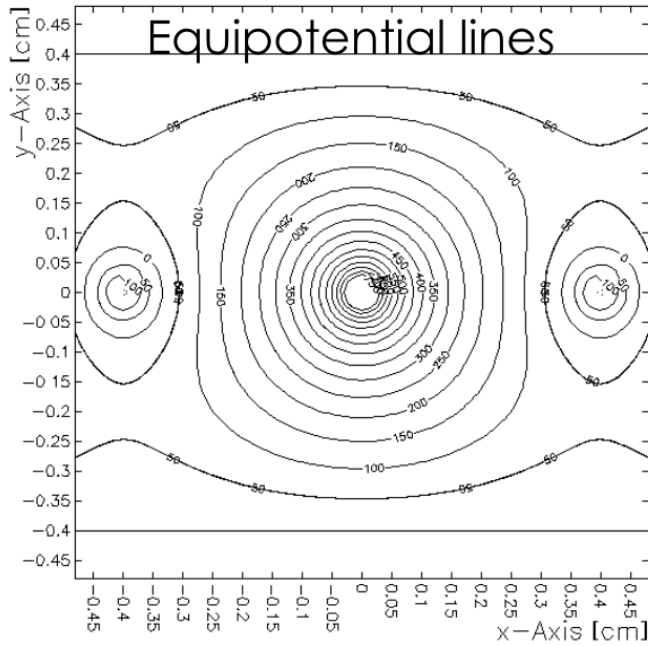


Figure 3.2: View down the axis of a drift cell and the equal voltages for this drift cell configuration. This image is taken from [12]

track as compared to a multi-wire proportional chamber. Each sense wire records the time a signal was detected from a track. For the same track, the trigger records the time the track enters the drift chamber and therefore the difference in time between the sense wire time and the trigger time is the drift time. For a drift chamber it is possible to produce a calibration curve which determines the position within a drift cell for a given drift time. This calibration curve is so-called the RT relation.

Even with a properly calibrated RT relation the track location is ambiguous from only one drift cell. This is because a single drift cell can only determine a track location as a distance from the sense wire. Therefore it is ambiguous where along the sense wire the track passed and also if the track passed to the left or right of the sense wire. For this reason drift chambers are built with several planes in series. A drift cell with the same orientation but shifted with respect to the first drift cell is used to distinguish left and right ambiguity and another cell with an orientation at an angle with respect to the first is used to determine where along the wire the track passed.

3.3 Preparation for DC05

One of the first steps in preparation for constructing DC05 was to simulate the detector response using Garfield [39]. The purpose of these simulations was to determine an operating threshold capable of achieving a $200 \mu\text{m}$ position resolution. With this position resolution goal in mind, Garfield simulated the electric potential field in each drift cell, as shown in Fig. 3.2, and was able to determine the arrival times for ionized electrons as a function of the number of primary ionized electrons for detection. This is important because the timing distribution for electron arrival times gets wider and therefore worsens the position knowledge as the number of primary electrons required for a signal increases. The variance of the electron arrival times was then used to determine the position resolution as a function of the number of primary electrons needed for detection. As is shown in Fig 3.3, the threshold should be tuned to detect the amplification of the fifth primary electron [12]. As is shown in Fig. 3.4 based on the simulation of the integrated induced current versus the drift arrival time, the threshold for detecting the signal should be no greater than 4 fC [12]. This threshold charge is determined by multiplying the induced current by the arrival time. The threshold was accordingly one of the design goals for the front-end electronics.

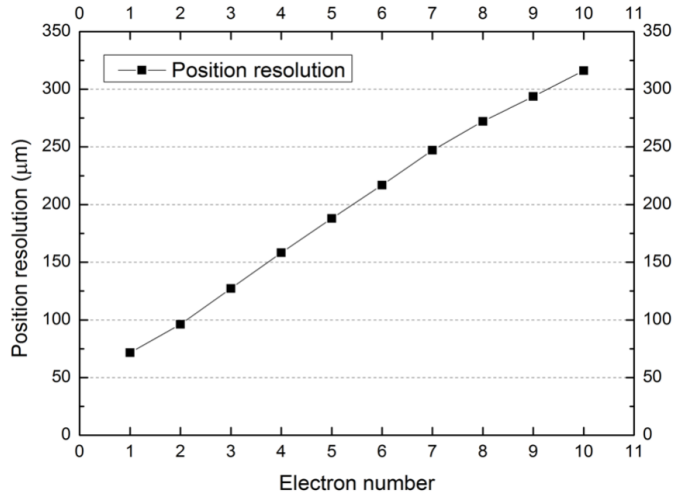


Figure 3.3: A simulation of the position resolution as a function of the number of primary electrons needed to record a signal. This image is taken from [12]

Two prototypes were built to gain hands on building expertise in preparation for construction. Both of these prototypes were constructed in a clean room in the Nuclear Physics Lab (NPL) at UIUC. Much of DC05 was built at the NPL as well. The two prototypes were called prototype A and prototype B. Prototype A, Fig. 3.5, consisted of 1 plane, eight sense wires, 9 field wires and was 50 cm in length. Prototype B on the other hand consisted of two planes with 16 sense wires per plane and a length of 163 cm. Prototype A

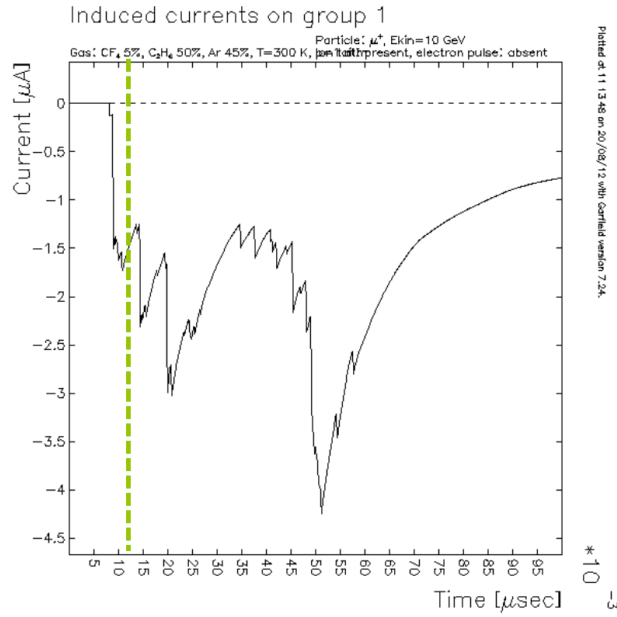


Figure 3.4: Garfield simulation of the induced signal current versus the arrival time. The green line corresponds to the arrival time of the fifth electron. This image is taken from [12]

was tested with beam at DESY and was shown to achieve $200 \mu\text{m}$ resolution [22]. Both of these prototypes were built using similar materials and construction techniques as the full size detector. In particular these two prototypes were the needed experience for working with sense wires having a diameter of $20 \mu\text{m}$.

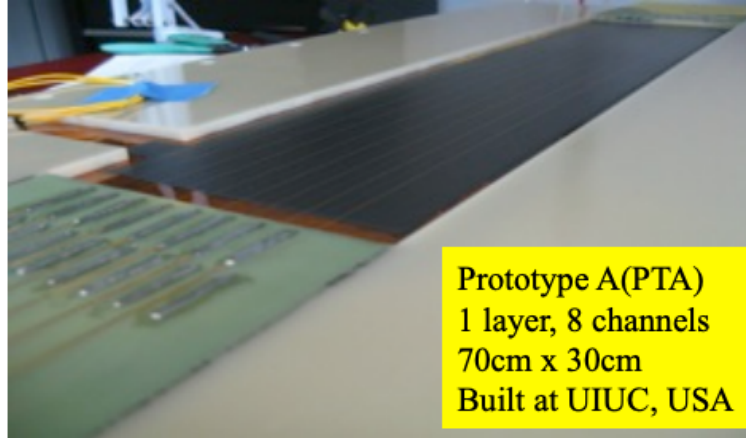


Figure 3.5: Inside view of prototype A. This image was taken from [22]



Figure 3.6

The completed DC05 being craned into the COMPASS large area spectrometer.

3.4 Design

The design of DC05, figure 3.6, was based off a previous large-area tracker at COMPASS. DC05 has an active area of $249 \times 209\text{cm}^2$ and consists of eight detector planes. The eight planes of DC05 correspond to four views, where each view measures a coordinate. The coordinates measured from DC05 are the horizontal, vertical and $\pm 10^\circ$ with respect to the horizontal. The horizontal and vertical coordinates consist of 2×256 sense wires and the offset to horizontal coordinates each consist of 2×320 wires for increased acceptance. In total DC05 includes 2304 sense wires and 2312 field wires. Each plane was made from a G-10 frame and five frames stacked together constituting a view. The whole detector was closed in with two precision, stainless steel stiffening frames, which were assembled with aluminized mylar as a gas window.

The views of DC05 consist of three cathode layers and two anode layers. The cathodes layers were made from carbon paint sprayed on a $25\ \mu\text{m}$ thin mylar layer. There were two single-layer cathodes layers and one layer with carbon on two sides within each view. Fig. 3.7 shows a side view of the layers of DC05. Additionally a 30 cm circular so-called beam killer was added to the cathodes to control the efficiency in the central part of the detector. The cathodes were nominally set to -1675 V and the beam killer voltage was set to -900 V for zero efficiency in the high flux central region. The voltage on the beam killer can however be raised above the amplification threshold if the beam flux is reduced and it is desirable to study the central region.

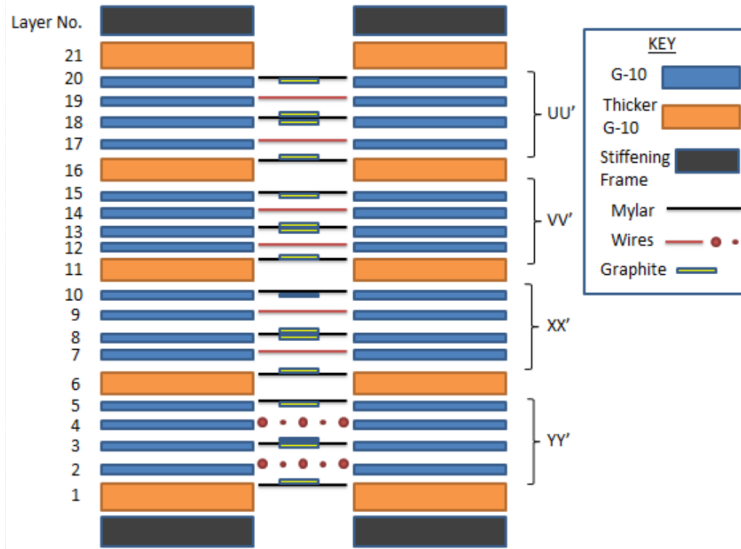


Figure 3.7: A side view sketch of the layers in DC05

The anode layers were made from alternating $20\ \mu\text{m}$ gold-plated tungsten sense wires and $100\ \mu\text{m}$ gold-plated copper beryllium field wires, as depicted in figure 3.8. Gold plating was used for both sense and field wires to prevent aging effects. The field wires were also placed at $-1675\ \text{V}$ and the sense wires were at $0\ \text{V}$. The nominal gain of DC05 is approximately 10^4 .

During data taking, DC05 is filled with a mixture 45% argon, 45% ethane and 10% CF_4 . The noble gas, argon, is the gas that is ionized and amplified, while ethane is used as a quencher and CF_4 is used to reduce aging effects. The quencher, ethane, absorbs photons from the electron avalanche which could produce and therefore make more electrons which would distort the electric field in a drift cell. The quencher therefore is used to reduce the avalanche and ensure the drift cell electric field lines are closer to their design values.

3.5 Construction

The construction of DC05 was carried out as precisely as possible starting with the precision from the stainless steel stiffening frames. The stiffening frames were cut with the highest relative accuracy by cutting the two frames on top of each other to a precision of $50\ \mu\text{m}$ everywhere in their plane. The precision from the

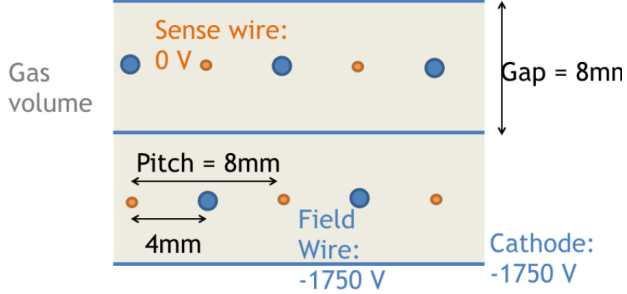


Figure 3.8
The drift cell dimensions of one plane in DC05

stiffening frames was transferred to the anode and cathode frames through 40 positioning pins. The G-10 frames were milled from strips at the NPL using a precision milling machine. Each four strips were then epoxied together on top of one of the stiffening frames.

The cathodes had mylar stretched and epoxied to them using a custom built stretching machine at CERN. Fig. 3.9 shows the process of stretching mylar on a cathode plane. An external company then spray painted carbon on them which was then polished till the resistance was approximately $30 \text{ k}\Omega/\text{m}$. All the sense and field wires were hand soldered as shown in Fig. 3.10, and sequentially verified for position using a microscope. It was estimated the position placement of each sense wire was at least as good as half the diameter of a sense wire or precise to $10 \mu\text{m}$.



Figure 3.9: Stretching mylar on a cathode plane at CERN

The final assemble was done at CERN. This consisted of stacking each of the 21 G-10 frames on top of the stiffening frame, Fig. 3.11, and attaching copper electronic shielding all along the exterior of the detector to reduce electronic noise.

There were various tests performed throughout the construction process for quality assurance before the final installation. The starting tests were measuring thickness and position of important cuts on the G-10

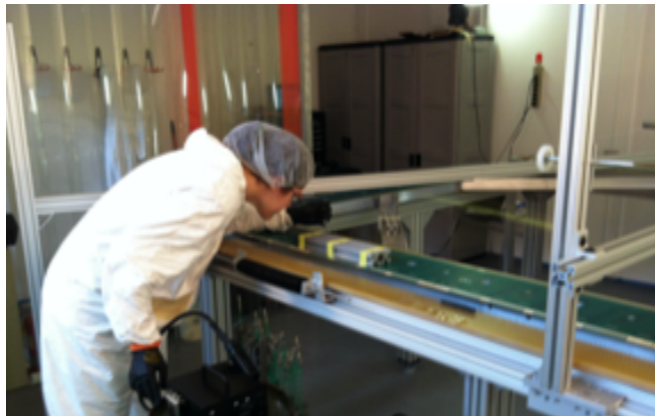


Figure 3.10: Hand soldering DC05 wires in the clean room at the NPL

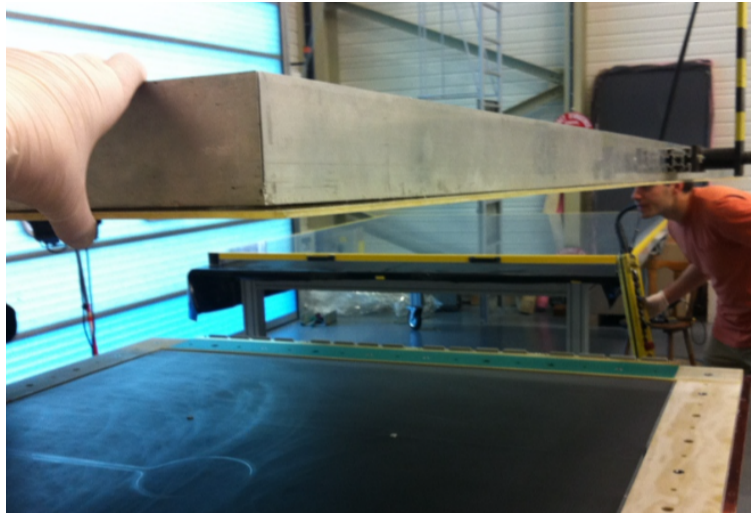


Figure 3.11: The process of stacking the G-10 frames at CERN

strips using a micrometer. G-10 strip thicknesses were iteratively milled until they reached better than $50 \mu\text{m}$ in thickness accuracy. The thickness deviation of the whole detector including the stainless steel stiffening frames was better than $750 \mu\text{m}$. The mechanical tension of the sense wires was tested for stability by ensuring the voltage difference between sense and field wires could reach as high as 2400 V in air. In addition the wire tension was cross-checked by determining the resonance frequency with which the wires vibrated. The resonance frequency was determined by placing the wires in a constant magnetic field and varying a sinusoidal current across each wire till the wires vibrated maximally. The leakage current between sense and field wires was verified to be less than 100 nA at nominal voltage in air. Finally amplification tests were first performed using a strontium-90 source and verifying the counts per electronics board increased

below the radioactive source.

3.6 2015 Performance

The overall performance of DC05 was checked using the COMPASS reconstruction software CORAL. In all cases the view of study was excluded from the reconstruction algorithm and the individual hit information for the view of interest was saved to get an unbiased measurement. The performance of DC05 is determined by judging its response to real tracks. In other words tracks that are not falsely reconstructed, so-called ghost tracks. To ensure these real tracks with higher quality for performance evaluation, only tracks with a primary vertex near the polarized target are considered.

The efficiency was found to be between 85% and 90% depending on the plane. The efficiency was determined by searching for a hit in the DC05 plane of interest within a road of 1.2 mm from the reconstructed track location. The road distance was chosen to be approximately six resolution deviations which is standard at COMPASS. Fig. 3.12 shows the efficiency of one plane of DC05. Using the so called RT relation, figure 3.13, the location of a track within a drift cell can be most accurately determined. This RT relation is tuned as a calibration to minimize the track residuals. The RT relation also varies depending on the beam type, intensity and the trigger type.

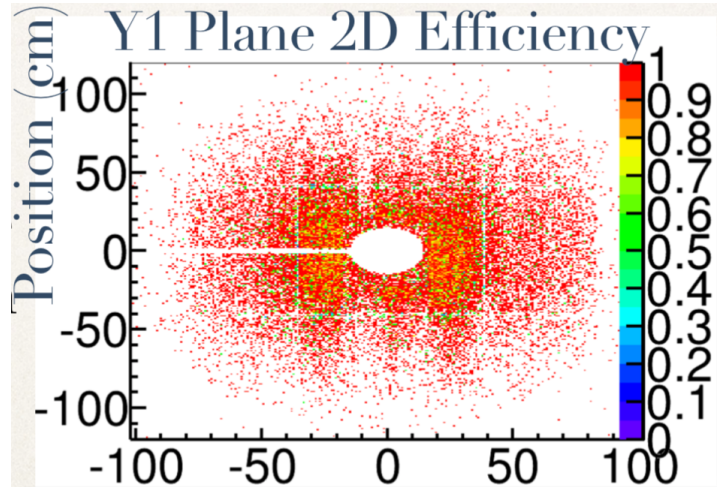


Figure 3.12

Two dimensional efficiency on the DC05Y1 plane. The center region with zero efficiency is a result of the beam killer.

The double layer residual was used to determine the position resolution. The double layer residual is the difference between the expected positions of the two planes in a view. The double residual is defined as

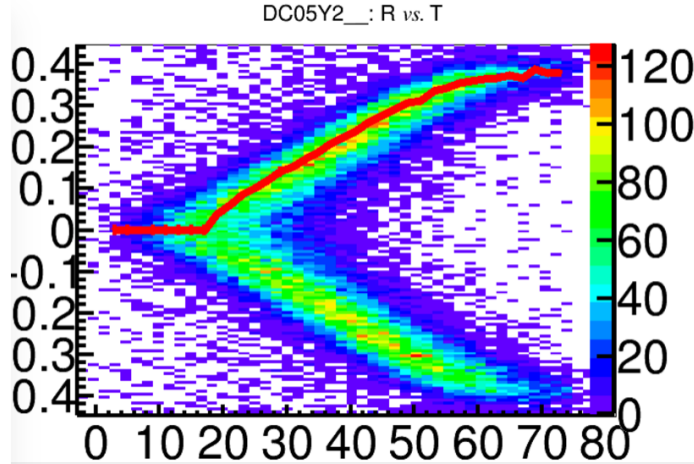


Figure 3.13

Time versus position relation, or RT relation, after calibrating. The red fit shows the calibration determined.

$$\Delta u_{\text{double residual}} = (u_{\text{plane 1}} - u_{\text{track}}) - (u_{\text{plane 2}} - u_{\text{track}}) = u_{\text{plane 1}} - u_{\text{plane 2}}, \quad (3.1)$$

where $u_{\text{plane 1(2)}}$ is the hit position on plane 1(2) determined from the detector of interested and u_{track} is the hit position determined from reconstruction. As can be seen in Eq. 3.1, the double layer residual is independent of the track resolution and only depends on the difference between detector hit positions. As the detector was construction with a known difference between these two cell hit positions, the double residual distribution is expected to be a constant value. Therefore the variance of the double residual distribution is the addition of the variance of the two individual planes. That is

$$\sigma_{\text{double residual}}^2 = \sigma_{\text{plane 1}}^2 + \sigma_{\text{plane 2}}^2 = 2 * \sigma_{\text{plane 1}}^2, \quad (3.2)$$

where $\sigma_{\text{plane 1(2)}}$ is the position resolution of plane 1(2). It is assumed that the position resolution is the same for each plane and therefore

$$\sigma_{\text{plane 1}} = \sigma_{\text{plane 2}} = \frac{\sigma_{\text{double residual}}}{\sqrt{2}} \quad (3.3)$$

For the 2015 Drell-Yan physics taking the resolution achieved was approximately 430 μm . This was determined by fitting the double residual with a Gaussian to extract the variance and assuming equal variance per plane in a view as is shown in Fig. 3.14.

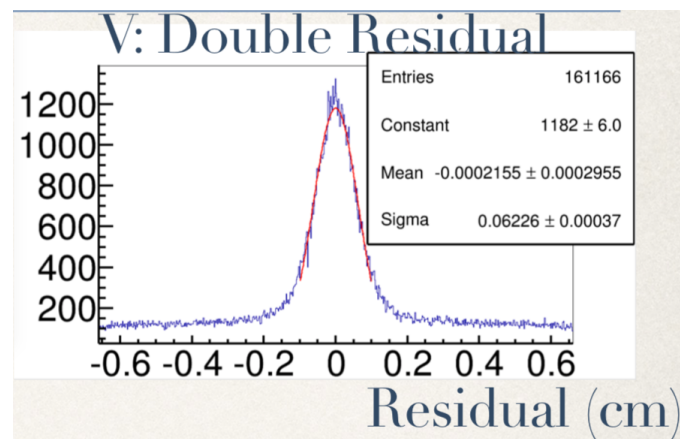


Figure 3.14: The double residual distribution for the V plane together with a Gaussian fit in red to determine the variance of the distribution

Chapter 4

Spectrometer Alignment

The alignment of the spectrometer is important for track reconstruction. Alignment is a part of pre-processing which ensures all the tracking detectors are centered relative to each other and therefore enables the track resolution to be as accurate as possible. Without accurate alignment, track reconstruction is not possible and it is therefore not possible to analyze any data. The author of this thesis oversaw collection of alignment data and was responsible for performing the alignment of the COMPASS spectrometer in 2015.

The objective of the alignment procedure is to produce a file called the detectors.dat. This file describes the parameters for all detectors at COMPASS and in particular, gives their orientation in space. For a tracking detector plane, there are four parameters the alignment procedure updates: the x central position, y central position, angle and the pitch. The pitch refers to a sense wire distance for wire chambers or central strip separation distance for detectors with strip readouts. One or two detectors.dat files was produced for each data taking period, depending on how many alignment runs were recorded that period. The goal of the alignment procedure is to have all four parameters aligned relative to a global reference frame in the COMPASS lab system.

The alignment procedure works by minimizing the distance between all the detector plane hit positions and a track position. The detector hit position is the location the detector believes a particle passed through the plane and the track position is the location the reconstruction believes the particle passed through the detector plane. The distance between this detector plane hit position and the track position will from here on be referred to as the residual distance. One residual is determined per track per detector associated with the track. The task of simultaneously minimizing all the residuals is difficult because there are over 300 detectors planes described in the detectors.dat. To accomplish this minimization, a large amount of quality data is needed and several specific matrix manipulations are utilized in the minimization procedure. This chapters gives an overview of the alignment procedure and includes some results from 2015. For a more complete review see reference [32].

4.1 Alignment Data

The alignment data is produced from a dedicated low intensity muon beam. The intensity in 2015 was approximately $10^5 \mu^-/\text{spill}$. A muon beam is desirable for alignment data because the beam muons interact less and therefore allows the alignment procedure to assume straight tracks in the minimization problem. The lower intensity is chosen because this allows for the assumption that only one track occurs per event and also the low intensity beam ensures a reduction of detector pile up effects. Reduction in pile up effects, makes reconstruction in the central detector areas possible, and therefore the beam killers on DC00, DC01, DC04 and DC05 can be set to an amplification voltage and as well all the GEM detectors can have their central high voltages turned up to an amplification voltage.

A dedicated trigger system is setup during alignment runs to maximize the illumination of the tracking detectors. The triggers used are a beam trigger, veto trigger and a halo trigger. While this trigger was good for illuminating the detectors, there were some timing shifts relative to the normal Drell-Yan trigger in 2015. For this reason some of the drift chambers used a different calibration curve shifted in time a few nanoseconds.

Two alignment runs of good quality are recorded either at the beginning, middle or end of a data taking period. The first alignment run is with the spectrometer magnets off and the second is with the spectrometer magnets on. The spectrometer magnets off run is used as a first iteration for the alignment procedure to initialize the tracking detector positions. The final alignment positions are then determined from the spectrometer magnets on data.

One physics run was also used to align detectors far from the beam line. Particularly, the outer region of the straw detectors did not receive enough statistics from the aligning runs. Therefore the alignment of the outer straw regions was performed with normal physics data. The runs used for alignment analysis in 2015 are listed in Table 4.1.

In 2015 the alignment runs were performed when the target solenoid was polarizing the target. The chicane magnets upstream of the target were therefore turned off to ensure the beam momentum was traveling along the target axis. Normally to achieve the reduced intensity, the T6 target is switch to an air target. However in 2015, the T6 target head was not able to switch between the different target lengths and therefore the maximum 500 mm target head was always in use. Therefore to achieve the desired lower intensity, a set of collimators upstream of the target reduced the aperture of the beam line till the correct intensity was achieved.

Period	Sub-period	Magnets off run	Magnets on run	Physics run	detectors.dat name
W07	one & two	259360	259361	259363	detectors.259361.transv.dat
W08	one & two	260072	260073	260100	detectors.260073.transv.dat
W09	one	260625	260626	260661	detectors.260626.transv.dat
	two	260625	260876	261312	detectors.260876.transv.dat
W10	one	261512	261513	261602	detectors.261513.transv.dat
	two	261512	261513	261974	detectors.261970.transv.dat
W11	one & two	262423	262425	262612	detectors.262370.transv.dat
W12	one & two	263139	263140	263175	detectors.263140.transv.dat
W13	one & two	263636	263637	263851	detectors.263637.transv.dat
W14	one & two	none	264428	264429	detectors.264163.transv.dat
W15	one & two	264614	264722	264736	detectors.264619.transv.dat

Table 4.1: COMPASS 2015 alignment data runs

4.2 Procedure

The starting point for alignment is a detectors.dat file with the tracking detector positions determined from a survey. The surveys are performed with the spectrometer magnets off and the precision from a survey is around 1 mm. Almost all of the detectors at COMPASS have a position resolution better than the survey precision however. Furthermore, several detectors near SM1 can shift in position due to the fringe field and therefore need a position determination with the spectrometer magnets on. For these reasons the alignment procedure is needed to improve on the survey precision and achieve the best possible track resolutions.

Between periods the starting detectors.dat file was the final detectors.dat from the previous week. Only for the first period were the survey positions used as a starting position. However, as long as the detector was not intentionally moved, it is expected that the shifts in detector position only change due to temperature effects and therefore do not change much.

Alignment Parameters

To best describe each detector relative to every other detector there are two reference systems of interest.

The first reference system is the COMPASS main reference system labeled $Oxyz$. This reference system can also be referred to as the COMPASS lab system, where the z-axis is along the beam momentum direction, the y-axis points vertically and the x-axis is such that the coordinate system is right handed. The origin of this reference system is at the center of the target from the original COMPASS setup.

The second reference system is the local reference system, which is labeled as $O'uvz$. This reference system is different for each detector and has its origin at the center of each detector center. The z-axis coincides with the z-axis in the COMPASS main reference system while the u-axis is in the direction along the measured coordinate of the detector, and the v-axis is perpendicular to the direction of the measured

coordinate of this detector. As an example, a drift chamber with vertical wires measures a coordinate along the horizontal direction and therefore it's u-axis is in the horizontal direction and it's v-axis is in the vertical direction. A drift chamber with horizontal wires, however, measures a coordinate along the vertical direction and therefore it's u-axis is in the vertical direction and it's v-axis is in the horizontal direction.

The alignment parameters are defined in $O'uvz$. The alignment procedure updates the starting detectors.dat file by the shifts

$$\delta u: \text{shift in } u \text{ direction}, \quad (4.1)$$

$$\delta \theta: \text{shift in rotation angle}, \quad (4.2)$$

$$\delta z: \text{shift in } z \text{ direction}, \quad (4.3)$$

$$\delta p: \text{shift in pitch}. \quad (4.4)$$

The shift in z direction has never converged however. As a result the z -coordinate from the survey is used as the final z position and the shift in pitch is used as an effective shift in the z direction.

Residual Function

The goal of the alignment procedure is to minimize the sum of all the residuals from each track and each detector associated with the track. Due to the fact that the alignment tracks are assumed to be straight, each track can be defined by four parameters. The track parameters, α_T , are

i: (x^0, y^0) the x and y coordinates at the main reference origin

ii: (t_x^0, t_y^0) the tangents of the track momentum in the x and y directions at the origin of the main reference system

where the track parameters are defined for each track. The alignment parameters, α_D , on the other hand are defined for each detector and are the same for all tracks. The alignment procedure minimizes the χ^2 function

$$\chi^2 = \sum_{i=1}^{n_{\text{tracks}}} \sum_{j=1}^{n_{\text{detectors}}} \frac{F_{i,j}^2(\alpha_{T,i}, \alpha_{D,j})}{\sigma_j^2}, \quad (4.5)$$

where σ_j^2 is the position resolution of detector j , $F_{i,j}$ is the residual distance of each detector j for each track i it is associated with.

The residual distance, F , depends on the track parameters and the detector parameters. For magnets off data the tracks are not bent at all and are therefore straight tracks through out the whole spectrometer. The x and y coordinates at position z are

$$x = x^0 + t_x^0(z - z^0), \quad (4.6)$$

$$y = y^0 + t_y^0(z - z^0), \quad (4.7)$$

where z^0 refers to the position at the origin in $Oxyz$. Rotating these track positions from the main references system, $Oxyz$, to the detector reference system, $O'uvz$, the residual distance is

$$F = \cos(\theta)[x^0 + t_x^0(z - z^0)] + \sin(\theta)[y^0 + t_y^0(z - z^0)] - u, \quad (4.8)$$

where u is the measured hit position from the detector at position z . To show the dependence on the alignment parameters

$$F(\alpha_T, \alpha_D + \delta\alpha_D) = (1 + \delta p) \left\{ \cos(\theta + \delta\theta)[x^0 + t_x^0(z - z^0)] + \sin(\theta + \delta\theta)[y^0 + t_y^0(z - z^0)] \right\} - (u + \delta u). \quad (4.9)$$

In Eq. 4.9, the change in pitch would intuitively affect the u position, however the change in pitch was moved to the track coordinates to make derivatives of F independent of u . This has no effect on the minimization of F .

In the case of magnets on data, the track positions need to have further modifications from Eq. 4.9. The magnetic field will bend the tracks so the track positions determined in Eq. 4.6 need to have further corrections. The track positions with SM1 and SM2 on are

$$x = x^0 + \delta x + (t_x^0 + \delta t_x)(z - z^0), \quad (4.10)$$

$$y = y^0 + \delta y + (t_y^0 + \delta t_y)(z - z^0), \quad (4.11)$$

where the δ_x , δt_x , δ_y and δt_y changes are determined from CORAL during the reconstruction process. Even though the spectrometer magnets have nominally vertical magnetic fields, there are still fringe fields which are not vertical. It is for this reason that CORAL also calculates an updated track position in the y -coordinate.

The residual dependence on the alignment parameters defined for magnetic fields on is then

$$F(\alpha_T, \alpha_D + \delta\alpha_D) = (1 + \delta p) \left\{ \cos(\theta + \delta\theta)[x^0 + \delta x + (t_x^0 + \delta t_x)(z - z^0)] + \sin(\theta + \delta\theta)[y^0 + \delta y + (t_y^0 + \delta t_y)(z - z^0)] \right\} - (u + \delta u). \quad (4.12)$$

χ^2 Minimization

The χ^2 function, Eq. 4.5, is analytically minimized. That is, the derivatives of Eq. 4.5 with respect to all the track and alignment parameters are set to zero and these alignment parameters are solved for. This can be written

$$\frac{1}{2} \frac{\partial \chi^2}{\partial \alpha_k} = \sum_i^{n_{\text{tracks}}} \sum_j^{n_{\text{detectors}}} \frac{1}{\sigma_j^2} \frac{\partial F_{i,j}}{\partial \alpha_k} F_{i,j} = 0. \quad (4.13)$$

To perform this calculation the residual function is Taylor expanded in the track and alignment parameters as

$$F = F^0 + \sum_k \frac{\partial F}{\partial \alpha_k} \alpha_k. \quad (4.14)$$

Using this approximation for F , Eq. 4.13 can be written as a matrix equation where the dimensions of the matrix are $(4n_{\text{detector}} + 4n_{\text{tracks}}) \times (4n_{\text{detector}} + 4n_{\text{tracks}})$. This matrix form is written as

$$\begin{bmatrix} \sum_i^{n_{\text{tracks}}} \sum_j^{n_{\text{detectors}}} \frac{1}{\sigma_j^2} \frac{\partial F_{i,j}}{\partial \alpha_{D_1}} \frac{\partial F_{i,j}}{\partial \alpha_{D_1}} & \dots & \sum_j^{n_{\text{detectors}}} \frac{1}{\sigma_j^2} \frac{\partial F_{i,j}}{\partial \alpha_{D_1}} \frac{\partial F_{i,j}}{\partial \alpha_{T_{4n_{\text{tracks}}}}} \\ \vdots & \ddots & \vdots \\ \sum_j^{n_{\text{detectors}}} \frac{1}{\sigma_j^2} \frac{\partial F_{i,j}}{\partial \alpha_{T_{4n_{\text{tracks}}}}} \frac{\partial F_{i,j}}{\partial \alpha_{D_1}} & \dots & \sum_j^{n_{\text{detectors}}} \frac{1}{\sigma_j^2} \frac{\partial F_{i,j}}{\partial \alpha_{T_{4n_{\text{tracks}}}}} \frac{\partial F_{i,j}}{\partial \alpha_{T_{4n_{\text{tracks}}}}} \end{bmatrix} \begin{bmatrix} \alpha_{D_1} \\ \vdots \\ \alpha_{T_{4n_{\text{tracks}}}} \end{bmatrix} = - \begin{bmatrix} \sum_i^{n_{\text{tracks}}} \sum_j^{n_{\text{detectors}}} \frac{1}{\sigma_j^2} \frac{\partial F_{i,j}}{\partial \alpha_{D_1}} F_{i,j}^0 \\ \vdots \\ \sum_j^{n_{\text{detectors}}} \frac{1}{\sigma_j^2} \frac{\partial F_{i,j}}{\partial \alpha_{T_{4n_{\text{tracks}}}}} F_{i,j}^0 \end{bmatrix}. \quad (4.15)$$

To solve Eq. 4.15, the matrix on the left side must be inverted. A normal alignment run however, results in over 200,000 tracks meaning this matrix is huge and infeasible to invert. Fortunately many of the entries in the matrix are zero which allows that this matrix inversion can be reduced to the inversion of several smaller matrices.

To perform the matrix inversion, note that Eq. 4.15 can be written

$$\left[\begin{array}{c|ccc} \sum_i C_i & \dots & G_i & \dots \\ \vdots & \ddots & 0 & 0 \\ G^T & 0 & \Gamma_i & 0 \\ \vdots & 0 & 0 & \ddots \end{array} \right] \left[\begin{array}{c} \alpha_\alpha \\ \vdots \\ \alpha_{T_i} \\ \vdots \end{array} \right] = \left[\begin{array}{c} \sum_i b_i \\ \vdots \\ \beta_i \\ \vdots \end{array} \right], \quad (4.16)$$

where $\sum_i C_i$ and $\sum_i b_i$ include only derivatives of $F_{i,j}$ with respect to alignment parameters, Γ_i and β_i include only derivatives of $F_{i,j}$ with respect to track parameters and G_i includes derivatives of $F_{i,j}$ with respect to both alignment and track parameters. Then reference [14] shows that Eq. 4.16 can be inverted to give the alignment parameters as

$$\alpha_\alpha = C'^{-1} b', \quad (4.17)$$

where

$$C' = \sum_i C_i - \sum_i G_i \Gamma_i^{-1} G_i^T, \quad (4.18)$$

and

$$b' = \sum_i b_i - \sum_i G_i \Gamma_i^{-1} \beta_i. \quad (4.19)$$

4.3 Results

The spectrometer alignment is performed in iterative steps. In each iteration of the alignment procedure, the matrix inversion, Eq 4.16, is performed and the alignment parameters are updated. All alignment tracks reconstructed in the first alignment iterations are based off of two pivot detectors. That is straight track parameters were determined from these two pivot detectors and all detectors were aligned relative to these pivot detectors. In 2015 the pivot detectors were GM05 in LAS and GM08 in SAS. After each iteration the detector parameters are updated to reduce the overall χ^2 value. Each new iteration is performed using the same data set and the alignment parameters are better described with each iteration.

The procedure used in 2015 was as follows:

1. Align with magnets off data. In this stage all the spectrometer detectors except the outer regions of the straw detectors are aligned. This includes all the detectors downstream of the polarized target but does not include the beam telescope detectors. Magnets off data is used as a first iteration and therefore only alignment in the u-coordinate is performed.
2. Align the same spectrometer detectors with magnets on data. In these iterations the detectors are

aligned for u-coordinate, angle and pitch.

3. Align the beam telescope detectors with magnets on data. In these iterations the previous detectors are all used as pivots. The beam telescope is therefore aligned relative to the spectrometer detectors.
4. Finally the outer region of the straws are aligned with physics data. For this alignment, the spectrometer detectors are again used as the pivot.

The quality of the alignment was monitored after each iteration and checked that the procedure was converging. In practice four iterations of each of the previous steps were found to be sufficient for convergence. To ensure the alignment data was from quality tracks, only tracks with momentum reconstructed and having reduced χ^2 less than 30 were considered.

As all detectors but the pixel detector planes measure a coordinate in one direction only, the detector positions are only updated in their measured direction. This can lead to detectors being well miss-aligned in the direction orthogonal to their measured coordinate however. To account for this, detector planes were updated to match the u-position from a detector plane measuring a different coordinate in the same detector station. For example DC04X planes had their y-coordinate determined from the DC04Y planes and DC04Y planes had their x-coordinate determined from DC04X planes.

After each alignment iteration the quality of the alignment is accessed for each individual detectors and for the spectrometer as a whole. The quality distributions to check after each iteration are described in the following list.

- i) The residual distribution, Δu , of each detector. That is a distribution of

$$\Delta u = u_{\text{track}} - u_{\text{detector}}, \quad (4.20)$$

where this distribution indicates if the detector is shifted along the direction of its measured coordinate. This distribution is expected to be a Gaussian with a zero mean and an RMS value comparable to the position resolution of the detector. Any deviation from a zero mean indicates the detector is shifted and a large RMS value indicates the detector is not performing as expected. If the detector is not performing as expected the most obvious reason is the calibrations used for that detector are not accurate. Fig. 4.1 shows an example of this distribution to monitor.

- ii) The change in the residual as a function of the detector's v-coordinate. In a wire detector for example, this is the change in the residual as a function of the distance along the wire. This distribution, Fig. 4.2,

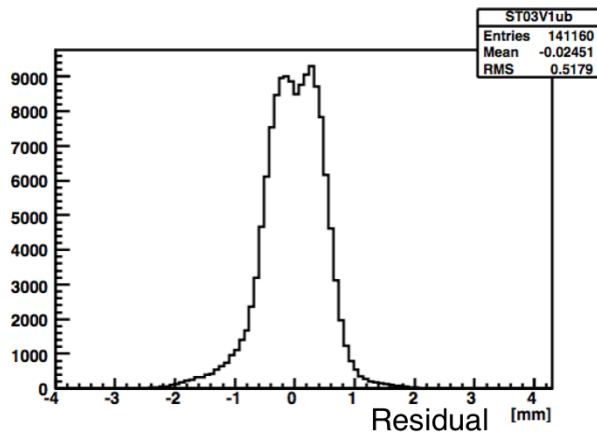


Figure 4.1: The residual distribution for a straw detector plane

is expected to be uniformly zero. A slope in this distribution indicates that the detector's angle is miss-aligned.

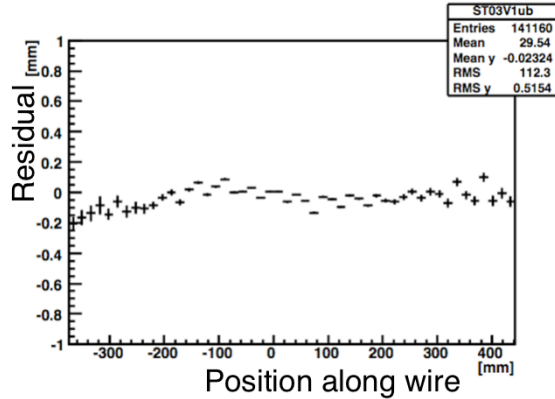


Figure 4.2: The residual as a function of the detector v-coordinate for a straw detector

- iii) The change in the residual as a function of the detector's u-coordinate. For a wire detector, this is the change in the residual as a function of the distance perpendicular to the wire. This distribution, Fig. 4.3, is also expected to be uniformly zero. A slope in this distribution indicates that the detector is miss-aligned in its z-coordinate or that its pitch is not described well. Due to the fact that the alignment data is with straight tracks, the alignment in the z-coordinate has never been able to converge. For this reason the pitch of the sensors on the detector is changed to account for this effective shift in z-position. The sensor pitch however, is never expected to be larger than the true detector pitch distance. If the detector pitch is determined to be too large after the alignment, this indicates a problem.

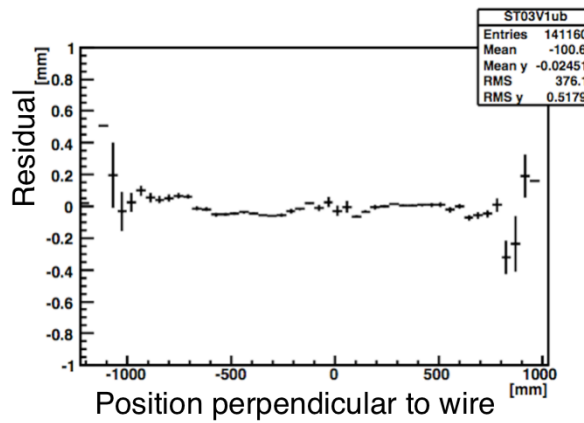


Figure 4.3: The residual as a function of the detector u-coordinate for a straw detector

- iv) The reduced χ^2 , Fig. 4.4, distribution of the reconstructed tracks. With better alignment the track reduced χ^2 distribution will approach a theoretical distribution of a reduced χ^2 distribution.

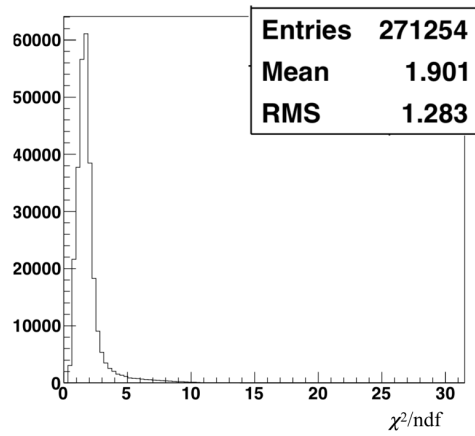


Figure 4.4: The reduced χ^2 from alignment data tracks

- v) The global number of tracks reconstructed. Better alignment implies that more detectors can be associated with a track and therefore more tracks will be reconstructed.

Chapter 5

Measurement of the Left-Right Asymmetry in the Drell-Yan Process

Introduction about L/R asym. In this Chapter.... Define AN

5.1 Data Sample

The data sample is from the 2015 COMPASS Drell-Yan measurement where a 190 GeV/c π^- beam impinged on a transversely polarized NH₃ target. The analysis data is from July 8, through November 12 which is after an initial spectrometer and beam commissioning phase. The data is split into 9 periods lasting approximated 2 weeks each, where each period consist of two sub-periods. To reduce systematic effects of acceptance and luminosity dependencies, the NH₃ target was split into two oppositely polarized cells with one cell polarized vertically up and one cell polarized vertically down in the lab frame. The cells were separated by 20 cm and the polarization of both cells was flipped between sub-periods. A summary of the data taking from each period is shown in Table 5.1.

Period	Sub-period	Polarization	First-Last run	Begin date	End date
W07	one	$\downarrow\uparrow$	259363 - 259677	July 9	July 15
	two	$\uparrow\downarrow$	259744 - 260016	July 16	July 22
W08	one	$\uparrow\downarrow$	260074 - 260264	July 23	July 29
	two	$\downarrow\uparrow$	260317 - 260565	July 29	August 5
W09	one	$\downarrow\uparrow$	260627 - 260852	August 5	August 12
	two	$\uparrow\downarrow$	260895 - 261496	August 12	August 26
W10	one	$\uparrow\downarrow$	261515 - 261761	August 26	September 1
	two	$\downarrow\uparrow$	261970 - 262221	September 4	September 9
W11	one	$\downarrow\uparrow$	262370 - 262772	September 11	September 22
	two	$\uparrow\downarrow$	262831 - 263090	September 23	September 30
W12	one	$\uparrow\downarrow$	263143 - 263347	September 30	October 7
	two	$\downarrow\uparrow$	263386 - 263603	October 8	October 14
W13	one	$\downarrow\uparrow$	263655 - 263853	October 15	October 21
	two	$\uparrow\downarrow$	263926 - 264134	October 22	October 28
W14	one	$\uparrow\downarrow$	264170 - 264330	October 28	November 2
	two	$\downarrow\uparrow$	264429 - 264562	November 4	November 8
W15	one	$\downarrow\uparrow$	264619 - 264672	November 9	November 11
	two	$\uparrow\downarrow$	264736 - 264857	November 12	November 16

Table 5.1: COMPASS 2015 data taking periods

5.1.1 Stability Tests

To ensure the data analyzed were recorded during stable beam and spectrometer conditions, stability of the analysis data was performed on a spill-by-spill and run-by-run basis. The data was recorded in runs with a maximum of 200 spills per run and where one spill can have several thousand events.

Bad Spill Analysis

To determine if a given spill is deemed unstable several macro variables were averaged over the spill and compared to neighboring spills. These macro variables were chosen specifically to be sensitive to the general stability conditions of the spectrometer and are listed in the follower enumerated list Table 5.1.1. The starting criteria for an event was two oppositely charged muons where a muon was defined as having crossed 15 radiation lengths of material.

1. number of beam particles divided by the number of events
2. number of beam particles divided by the number of primary vertices
3. number of hits per beam track divided by the number of beam particles
4. number of primary vertices divided by the number of events
5. number of outgoing tracks divided by the number of events
6. number of outgoing particles from a primary vertex divided by the number of primary vertices
7. number of outgoing particle from primary vertex divided by the number of events
8. number of outgoing particles from primary vertex divided by the number of events
9. number of hits from outgoing particles divided by the number outgoing particles
10. number of μ^+ tracks divided by the number of events
11. number of μ^+ tracks from primary vertex divided by the number of events
12. number of μ^- tracks divided by the number of events
13. number of μ^- tracks from primary vertex divided by the number of events
14. $\sum \chi^2$ of outgoing particles divided by the number of outgoing particles
15. $\sum \chi^2$ of all vertices divided by the number of all vertices in an event

16. Trigger rates (LASxLAS, OTxLAS, LASxMT)

If the spectrometer was stable during a spill the average values from the variables in Table ?? are expected to be constant from one spill to the next. To determine if a spill was recorded in unstable conditions the spill of interest is compared with its neighboring 2500 spill occurring before and after in time. If the spill of interest is a specified sigma away from any of the neighboring spills too many times, the spill of interest is marked as a bad spill. If a spill fails this bad spill criteria for any of the macro variables in Table ?? the spill is deemed bad and not included in the analysis. The criteria for the sigma distance and number times a spill crosses this distance to be deemed a bad are different for each data taking period. In addition to checking the nearest spills for each spill, all the spills in a run are marked bad if the run it has less than 10 spills or greater than 70% bad spills. Table ?? describes the impact of the bad spill analysis on each period.

Bad Run Analysis

The stability of the spectrometer is also verified on run-by-run check in parallel to the spill-by-spill check. The run-by-run analysis compares kinematic distributions and the average of these distributions per run to the same kinematic distributions and averages from the other runs in a given period. The kinematic distributions tested are: x_N , x_π , x_F , q_T , $M_{\mu\mu}$, P_{μ^+} , P_{μ^-} , P_γ , P_{π^-} , and vertex x , y and z positions. The quantities in the run-by-run analysis are expected to influence the asymmetries measured, however their distributions and averages are not expected to have spin-influenced effects from the limited statistics in just a single run. An unbinned-Kolmogorov test (UKT) is performed to compare each distribution. An UKT test is made between all the runs in a given period and a run is marked bad if it is incompatible with most of the runs in a period. The comparison of mean for each distribution from each run is made with the average from a given period. If one of the kinematical variables has an average more than five standard deviations from the average within a period, the run is rejected. The results of the bad spill rejection after having already applied the bad spill rejection are shown in Table ??.

5.1.2 Event Selection

The cuts in the event selection were chosen to ensure the event consisted of two oppositely charged muons, so called dimuons, resulting from a pion collision in the transversely polarized target. The event selection was initially filtered from miniDSTs to μ DSTs using the criteria of at least two muons detected in the spectrometer. The cuts used in this analysis are described in the following enumerated list where the event selection is performed on these μ DSTs and the events used come from the slot1 production. A summary of the number of events remaining after the last cuts is shown in Table 5.1.

Table 5.2: Stability analysis rejection percentages

Period	Bad spill rejection	Bad spill and spill rejection
W07	11.79%	17.94%
W08	18.00%	21.19%
W09	14.76%	17.11%
W10	15.88%	17.80%
W11	22.49%	26.14%
W12	12.71%	13.79%
W13	22.32%	22.73%
W14	8.91%	10.70%
W15	3.94%	3.94%

1. Two oppositely charged particles from a common best primary vertex. A primary vertex is defined as any vertex with an associated beam particle. In case of multiple common primary vertices the best primary vertex was determined by CORAL tagging the vertex as best primary (PHAST method `PaVertex::IsBestPrimary()`). In the case that CORAL did not tag any of the common vertices as the best primary the vertex with the smallest spatial χ^2 value was used as the best primary vertex.
2. A dimuon trigger fired. A dimuon trigger firing means there are at least two particles in coincidence in this event. The dimuon triggers used were a coincidence between two particles in the large angle spectrometer, LAS-LAS trigger, or a particle in the large angle spectrometer and a particle in the Outer hodoscope in the small angle spectrometer, LAS-Outer trigger. The LAS-Middle trigger was used as a veto on beam decay muons where beam decay muons result from the decay of the beam pion, kaon or anti-proton into a muon. This beam decay muon can then be in coincidence with a positive muon from another decay or strong reaction in the target. The LAS-Middle trigger was used a veto because this trigger was found to have many events resulting from a beam pion decaying to a muon.
3. Both particles are muons. A muon was defined as having crossed 30 radiation lengths of material between the particles first and last measured points. This criteria has been previously determined to be effective at distinguishing between muons and hadrons. In the data production no detectors were used from upstream of the hadron absorber so the absorber is not included in the determination of material crossed.
4. The first measured point for both particles is before 300 cm and the last measured point is after 1500 cm. This cut ensures both particles have positions upstream of the first spectrometer magnet and downstream of the first muon filter.
5. The timing of both muons is defined. This checks that the time relative to the trigger time is determined for both muons so further timing cuts can be performed.

6. Both muons are in time within 5 nanoseconds. This track time for each muon is defined relative to the trigger time as in the previous cut. This cut helps rejected uncorrelated muons.
7. The muon track's spacial reduced χ^2 's are individually less than 10. This cut ensures track quality.
8. A validation that each muon crossed the trigger it was associated as having triggered. This trigger validation cut was performed by extrapolating (PHAST Method PaTrack::Extrapolate()) each muon track back to the hodoscopes it fired and determining if the muon crossed the geometric acceptance of both hodoscopes.
9. The event does not occur in the bad spill or run list. Many tests were performed to test the basic stability of the spectrometer and beam as described in section 5.1.1. The spills placed on the bad spill list were deemed to occur during unstable data taking conditions.
10. The Drell-Yan kinematics are physical. That is x_π and x_N are between 0 and 1 and x_F is between -1 and 1.
11. The transverse momentum of the virtual photon, q_T is between 0.4 and 5.0 GeV/c. The lower limit ensures azimuthal angular resolution is sufficient and the upper cut is minimal and further ensures the kinematic distributions are physically possible.
12. The vertex originated within the z-positions of the transversely polarized target cells defined by the target group ($-294.5 < Z_{\text{vertex}} < -239.3$ for the upstream target or $-219.5 < Z_{\text{vertex}} < -164.3$ cm for the downstream target).
13. The vertex is within the radius of the polarized target measured to be 1.9 cm.

Cuts	W07	W08	W09	W10	W11	W12	W13	W14	W15	WAll	% Remaining
All Data	19410	19184	19654	20707	31371	23563	20561	13154	7697	175301	100.00 %
Good Spills	15947	14899	16217	16895	23041	20184	16026	11796	7422	142427	81.70 %
$0 < x_\pi, x_N < 1, -1 < x_F < 1$	15932	14886	16200	16885	23022	20171	16013	11794	7414	142317	81.70 %
$0.4 < q_T < 5 \text{ (GeV/c)}$	14342	13385	14609	15239	20667	18101	14365	10588	6636	127932	60.75 %
Z Vertex within NH ₃	4256	4024	4330	4552	6369	5503	4411	3130	2028	38603	15.05 %
Vertex Radius < 1.9cm	4175	3950	4257	4474	6252	5414	4334	3078	1987	37921	12.21 %

Figure 5.1: Event selection statistics for this analysis

5.1.3 Binning

The asymmetries are measured in bins of x_N , x_π , x_F , q_T , and $M_{\mu\mu}$. Where x_N and x_π the momentum fractions of the target nucleon and beam pion respectively, $x_F = x_\pi - x_N$, q_T is the transverse momentum

of the virtual photon and $M_{\mu\mu}$ is the invariant mass of the di-muon. The binning was determined by requiring equal statistical population in each kinematic bin. In addition, the asymmetries are determined in an integrated bin using all the analysis data. The analyzes binning limits are summarized in Table 5.3.

Kinematics	Lowest limit	Upper limit bin 1	Upper limit bin 2	Upper limit bin 3
x_N	0.0	0.13	0.19	1.0
x_π	0.0	0.40	0.56	1.0
x_F	-1.0	0.22	0.41	1.0
q_T (GeV/c)	0.4	0.86	1.36	5.0
$M_{\mu\mu}$ (GeV/c ²)	4.3	4.73	5.50	8.5

Table 5.3: Analysis binning limits

5.2 Extraction of Asymmetries

There are many ways to determine the left-right asymmetry denoted as A_N . The relevant techniques for the 2015 COMPASS setup are described and compared to ensure confidence in the end results. Sec. 5.2.1 starts with a general introduction to the notations and ideas used for all the asymmetry methods.

5.2.1 Geometric Mean

The number of physics counts, N , detected from any particular target can be written as

$$N = L * \sigma * a, \quad (5.1)$$

where L is the luminosity, σ is the cross-section of such an event and a is the acceptance. In this formula the acceptance is a function of detector efficiencies and the spectrometer acceptance. In simple words, the number of counts detected is the number of possible chances for an event to occur times the probability for an event to occur and that the event will be detected. To get spin-dependent counts for the left-right asymmetry, the target, polarization and left or right direction relative to the spin have to be included in the counts. Generically this can be written

$$N_{cell,L(R)}^{\uparrow(\downarrow)} = a_{cell,spectrometer\ direction}^{\uparrow(\downarrow)} * L_{cell}^{\uparrow(\downarrow)} * \sigma_{L(R)}, \quad (5.2)$$

where $\uparrow (\downarrow)$ denotes the target polarization, cell is either cell 1 for the upstream target cell or cell 2 for the downstream target cell, $L(R)$ is left(right) of the spin direction and spectrometer direction denotes either the spectrometer Jura side or the Saleve side corresponding to where the event was detected.

The most basic method to determine A_N per target cell is

$$A_N = \frac{1}{P} \frac{N_L - N_R}{N_L + N_R}, \quad (5.3)$$

where the counts, N , are defined as Eq. 5.1, and P denotes the fraction of polarized nucleons. An intuitive picture of left and right defined in the target frame is shown in Fig. 5.2.

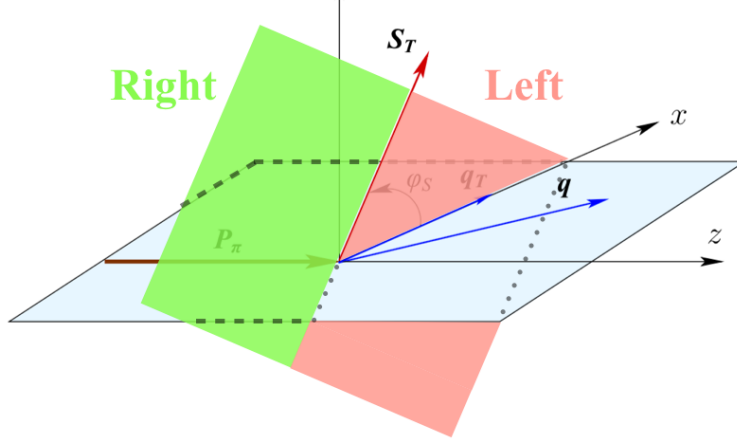


Figure 5.2: The definition of the left plane (red) and right plane (green) defined from a target spin up configuration in the target frame

The previous definitions of the detected counts, Eq. 5.2 and Eq. 5.1, and therefore also Eq. 5.3 all depend on the spectrometer acceptance. This is a problem because the spectrometer acceptance can change with time and space and therefore can be dependent on the physical kinematics which produced the event. Such dependencies can cause unphysical false asymmetries in the measurement of A_N and must therefore be removed or must be included as systematic effects.

Forming the geometric mean asymmetry is, however, a way to determine the left-right asymmetry without acceptance effects from the spectrometer. It is defined as

$$\frac{1}{P} \frac{\sqrt{N_{\text{cell } 1(2),L}^{\uparrow} N_{\text{cell } 1(2),L}^{\downarrow}} - \sqrt{N_{\text{cell } 1(2),R}^{\uparrow} N_{\text{cell } 1(2),R}^{\downarrow}}}{\sqrt{N_{\text{cell } 1(2),L}^{\uparrow} N_{\text{cell } 1(2),L}^{\downarrow}} + \sqrt{N_{\text{cell } 1(2),R}^{\uparrow} N_{\text{cell } 1(2),R}^{\downarrow}}}, \quad (5.4)$$

where P represents the fraction of polarized nucleons. Table ?? summarizes the notations used throughout this chapter.

Equation 5.4 can be thought of simply as the normalized difference of left minus right counts. Left and right counts are determined relative to the target spin directions and are defined as

Table 5.4: Notations used in defining the left/right asymmetry

Notation	Description
L(R)	virtual photon detected left(right) of spin
Jura(Saleve)	spectrometer west(east) side
cell 1(2)	up(down)stream target cell
\uparrow (\downarrow)	target cell polarized up(down)
P	fraction of polarized target nucleons

$$\begin{aligned} \text{Left} : \hat{q}_T \cdot (\hat{S}_T \times \hat{P}_\pi) &> 0 \\ \text{Right} : \hat{q}_T \cdot (\hat{S}_T \times \hat{P}_\pi) &< 0, \end{aligned} \quad (5.5)$$

where \hat{q}_T , \hat{S}_T and \hat{P}_π are unit vectors in the target reference frame for the virtual photon transverse momentum, the target spin and the beam pion momentum respectively.

Using Eq. 5.2 for the definition of counts, the geometric mean asymmetry is

$$\frac{1}{P} \frac{\kappa_{\text{geomean}} \sqrt{\sigma_L \sigma_L} - \sqrt{\sigma_R \sigma_R}}{\kappa_{\text{geomean}} \sqrt{\sigma_L \sigma_L} + \sqrt{\sigma_R \sigma_R}}, \quad (5.6)$$

where κ is a ratio of acceptances defined as

$$\kappa_{\text{geomean}} = \frac{\sqrt{a_{\text{cell 1(2), Jura}}^{\uparrow} a_{\text{cell 1(2), Saleve}}^{\downarrow}}}{\sqrt{a_{\text{cell 1(2), Saleve}}^{\uparrow} a_{\text{cell 1(2), Jura}}^{\downarrow}}}. \quad (5.7)$$

Here the detection side of spectrometer is specified by looking down the beam line as either Jura to mean left or Saleve to mean right. These relations of Jura is left and Saleve is right are only strictly true if the target polarization is pointing straight up in the target frame. In particular if the beam particle and the target polarization do not make a right angle in the laboratory frame this relation will no longer be strictly true but is an approximation for ease of notation.

Relation 5.6 is equal to A_N if κ is equal to one. However as stated previously, time effects can vary κ from unity. These effects are estimated through false asymmetry analysis and included in the systematic error bars described in section 5.3. Equation 5.4 is therefore to a good approximation an acceptance free method to determine A_N . It is also defined for the upstream and downstream cells independently and therefore can be used as a consistency check between the two target cells.

The statistical uncertainty of the geometry mean is

$$\frac{1}{P} \frac{\sqrt{N_L^\uparrow N_L^\downarrow N_R^\uparrow N_R^\downarrow}}{\left(\sqrt{N_L^\uparrow N_L^\downarrow} + \sqrt{N_R^\uparrow N_R^\downarrow}\right)^2} \sqrt{\frac{1}{N_L^\uparrow} + \frac{1}{N_L^\downarrow} + \frac{1}{N_R^\uparrow} + \frac{1}{N_R^\downarrow}}, \quad (5.8)$$

which reduces to $\frac{1}{P} \frac{1}{\sqrt{N}}$ in the case of equal statistics in each direction from each target cell polarization.

5.2.2 Two-Target Geometric Mean

As described in section 5.1 COMPASS had two oppositely polarized target cells in 2015. The previous geometric mean asymmetry, however, determined an A_N per target. It is desirable from a statistical point of view, however, to determine one A_N from the 2015 COMPASS setup. It is also desirable for comparison purposes to determine A_N using all the information from the 2015 COMPASS setup. This can be accomplished by modifying the geometric mean to add both target cells as follows

$$\frac{1}{P} \frac{\sqrt[4]{N_{\text{cell } 1,L}^\uparrow N_{\text{cell } 1,L}^\downarrow N_{\text{cell } 2,L}^\uparrow N_{\text{cell } 2,L}^\downarrow} - \sqrt[4]{N_{\text{cell } 1,R}^\uparrow N_{\text{cell } 1,R}^\downarrow N_{\text{cell } 2,R}^\uparrow N_{\text{cell } 2,R}^\downarrow}}{\sqrt[4]{N_{\text{cell } 1,L}^\uparrow N_{\text{cell } 1,L}^\downarrow N_{\text{cell } 2,L}^\uparrow N_{\text{cell } 2,L}^\downarrow} + \sqrt[4]{N_{\text{cell } 1,R}^\uparrow N_{\text{cell } 1,R}^\downarrow N_{\text{cell } 2,R}^\uparrow N_{\text{cell } 2,R}^\downarrow}}. \quad (5.9)$$

As in the basic geometric mean asymmetry, section 5.2.1, left and right are determined relative to the spin direction of the target as in Eq. 5.5. Again using Eq. 5.2 for the definition of counts, the two target geometric mean asymmetry, Eq. 5.9, can be written as

$$\frac{1}{P} \frac{\kappa_{\text{two-target}} \sqrt[4]{\sigma_L \sigma_L \sigma_L \sigma_L} - \sqrt[4]{\sigma_R \sigma_R \sigma_R \sigma_R}}{\kappa_{\text{two-target}} \sqrt[4]{\sigma_L \sigma_L \sigma_L \sigma_L} + \sqrt[4]{\sigma_R \sigma_R \sigma_R \sigma_R}}, \quad (5.10)$$

,

where now $\kappa_{\text{two-target}}$ is the ratio of acceptances from all targets and polarizations. This inclusive acceptance ratio is defined as

$$\kappa_{\text{two-target}} = \frac{\sqrt[4]{a_{\text{cell } 1,\text{Jura}}^\uparrow a_{\text{cell } 1,\text{Saleve}}^\downarrow a_{\text{cell } 2,\text{Jura}}^\uparrow a_{\text{cell } 2,\text{Saleve}}^\downarrow}}{\sqrt[4]{a_{\text{cell } 1,\text{Saleve}}^\uparrow a_{\text{cell } 1,\text{Jura}}^\downarrow a_{\text{cell } 2,\text{Saleve}}^\uparrow a_{\text{cell } 2,\text{Jura}}^\downarrow}}. \quad (5.11)$$

In this case the acceptance ratio is expected to vary less with time and therefore be closer to unity than the normal geometric mean acceptance ratio, Eq. 5.7. This is a consequence of having the different target cells oppositely polarized. Rewriting Eq. 5.11 with sub-period superscripts instead of target polarization superscripts

$$\kappa_{two-target} = \frac{\sqrt[4]{a_{cell 1,Jura}^a a_{cell 1,Saleve}^b a_{cell 2,Jura}^b a_{cell 2,Saleve}^a}}{\sqrt[4]{a_{cell 1,Saleve}^a a_{cell 1,Jura}^b a_{cell 2,Saleve}^b a_{cell 2,Jura}^a}}, \quad (5.12)$$

where sub-period a is with the upstream target polarized up and the downstream target polarized down and vice versa for sub-period b . From Eq. 5.12 it is more evident that the acceptance ratio terms for sub-period b are reciprocal to the terms for sub-period a and therefore the acceptance ratio is expected to be more stably close to unity.

Finally the statistical uncertainty of the two target geometric mean is

$$\frac{1}{P} \frac{LR}{(L+R)^2} \sqrt{\sum_{cell} \sum_{polarization} \left(\frac{1}{N_{cell,L}^{polarization}} + \frac{1}{N_{cell,R}^{polarization}} \right)}, \quad (5.13)$$

where L can be thought of as the left counts and equals to $\sqrt[4]{N_{cell 1,L}^\uparrow N_{cell 1,L}^\downarrow N_{cell 2,L}^\uparrow N_{cell 2,L}^\downarrow}$ and R can be thought of as the right counts and equals $\sqrt[4]{N_{cell 1,R}^\uparrow N_{cell 1,R}^\downarrow N_{cell 2,R}^\uparrow N_{cell 2,R}^\downarrow}$. The statistical uncertainty for the two target geometric mean also reduces to $\frac{1}{P} \frac{1}{\sqrt{N}}$ in the case of equal statistic populations in each direction and target polarization.

5.3 Systematic Studies

Several tests were performed to estimate the systematic uncertainty of the left-right asymmetry. The systematic errors are determined by adding all non-zero systematic uncertainties in quadrature. The impact from each source of systematic error is summarized in Tab. 5.7.

5.3.1 Period Compatibility (Time Dependence)

The asymmetries calculated for each time period in each kinematic bin are shown in Fig. 5.3.

By eye the asymmetry fluctuations appear to be statistically compatible. To quantify the compatibility of the asymmetries between the periods, a pull distribution is formed. The pull value is defined as

$$\Delta A_i = \frac{A_i - \langle A \rangle}{\sqrt{\sigma_{A_i}^2 - \sigma_{\langle A \rangle}^2}}, \quad (5.14)$$

and is determined for each period and kinematic bin. There are therefore 3 (number of bins) x 5 (number of kinematics) x 9 (number of periods) = 135 entries in the pull distribution. This distribution is shown in Fig. 5.4 along with a Gaussian fit. If the asymmetries all come from the same parent distribution then

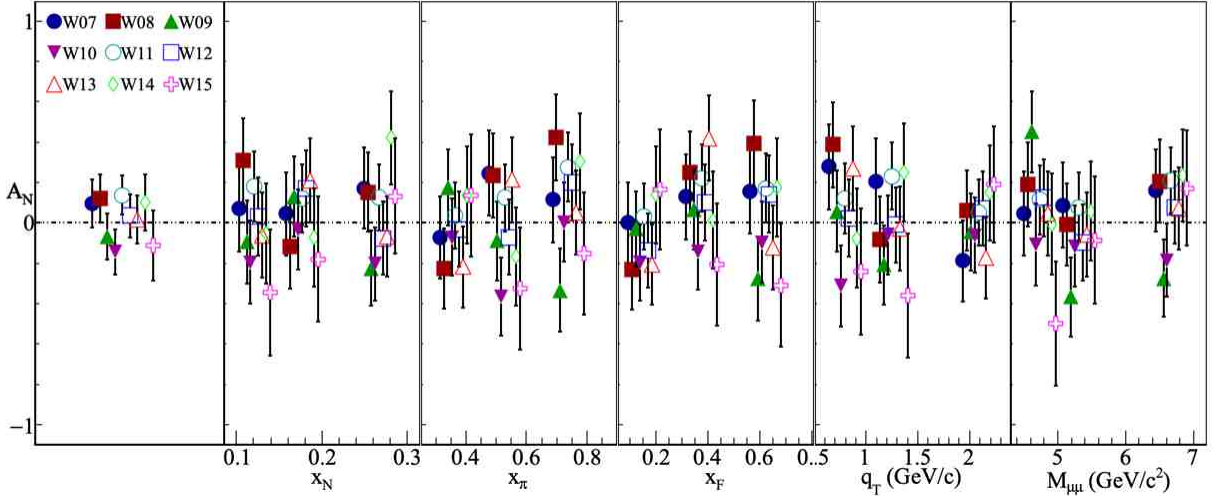


Figure 5.3: A_N determined for each period

due to the central limit theorem the pull distribution will be a Gaussian distribution with zero mean and unit variance. The discrepancy of the pull distribution from a standard Gaussian distribution is used to determine a systematic error as

$$\frac{\sigma_{\text{systematic}}}{\sigma_{\text{statistical}}} = \sqrt{|\sigma_{\text{pull}}^2 - 1|} + \frac{\mu_{\text{pull}}}{2}. \quad (5.15)$$

As the asymmetries in different kinematic bins are formed using the same data set the asymmetries between kinematic binning are correlated. For this reason an uncorrelated pull distribution is also formed for each kinematic bin and also compared with a standard Gaussian distribution. These distributions are shown in Fig. 5.5 and the results of the Gaussian fit are shown in Fig. 5.6. For these uncorrelated pull distributions there are now only 3 (number of bins) \times 9 (number of periods) = 27 entries in each kinetically binned pull distributions and only 9 (number of periods) bins in the integrated pull distribution.

Even though the Gaussian fits did not give exactly a standard Gaussian, the fit parameters are well compatible with a standard Gaussian within the errors of the fit. Therefore no systematic error was assigned due to incompatibility of the periods.

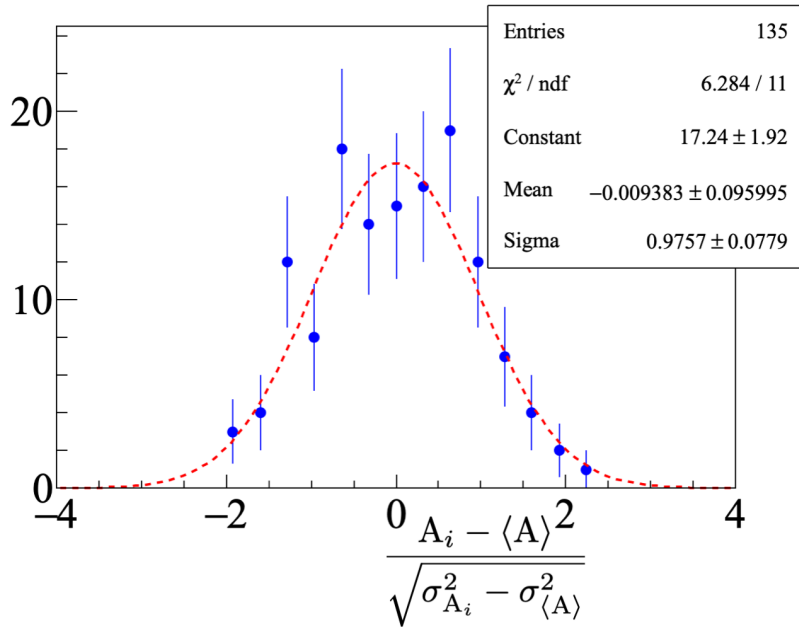


Figure 5.4: Pull distribution from the two target geometric mean

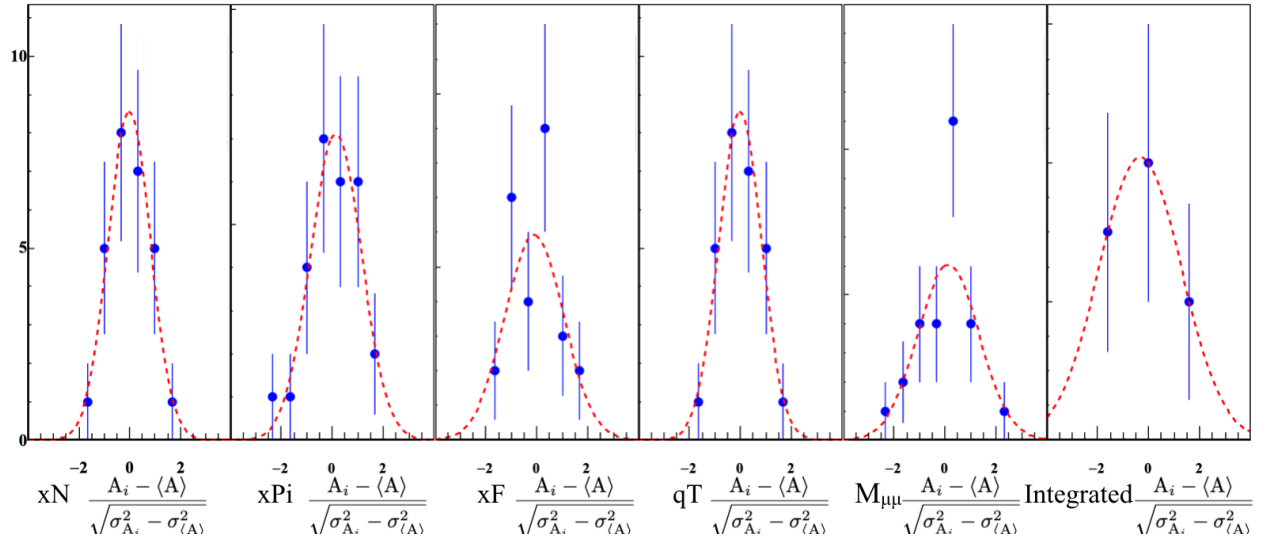


Figure 5.5: Uncorrelated pull distributions

Entries	27	Entries	27	Entries	27	Entries	27	Entries	27	Entries	9
χ^2 / ndf	0.4347 / 3	χ^2 / ndf	1.056 / 4	χ^2 / ndf	3.416 / 3	χ^2 / ndf	0.4347 / 3	χ^2 / ndf	3.152 / 4	χ^2 / ndf	1.091e-08 / 0
Constant	8.548 ± 2.043	Constant	7.101 ± 1.827	Constant	5.922 ± 1.622	Constant	8.548 ± 2.043	Constant	6.038 ± 1.603	Constant	4.085 ± 1.992
Mean	-0.01562 ± 0.17221	Mean	0.1422 ± 0.2204	Mean	-0.1036 ± 0.2910	Mean	-0.01562 ± 0.17221	Mean	0.1287 ± 0.2860	Mean	-0.3308 ± 0.8192
Sigma	0.8386 ± 0.1304	Sigma	1.004 ± 0.201	Sigma	1.15 ± 0.31	Sigma	0.8386 ± 0.1304	Sigma	1.197 ± 0.256	Sigma	1.616 ± 1.101

Figure 5.6: Results of Gaussian fit for the uncorrelated pull distributions

5.3.2 False Asymmetries

Acceptance From False Asymmetries

As was pointed out in Sec. 5.2.1 and Sec. 5.2.2, the asymmetry measurement assumes the acceptance does not change with time and therefore the acceptance ratios Eq. 5.7 and Eq. 5.11 are unitary. Any deviation from a unitary acceptance ratio is estimated with a false asymmetry and is taken as a systematic error. To determine if acceptance does change with time, a false asymmetry is calculated where the only way the false asymmetry could be non-zero is if acceptance changes with time. This false asymmetry for the two target geometric mean is

$$A_{N,\text{False}} = \frac{1}{P} \frac{\sqrt[4]{N_{\text{cell } 1,R}^{\uparrow} N_{\text{cell } 1,L}^{\downarrow} N_{\text{cell } 2,L}^{\uparrow} N_{\text{cell } 2,R}^{\downarrow}} - \sqrt[4]{N_{\text{cell } 1,L}^{\uparrow} N_{\text{cell } 1,R}^{\downarrow} N_{\text{cell } 2,R}^{\uparrow} N_{\text{cell } 2,L}^{\downarrow}}}{\sqrt[4]{N_{\text{cell } 1,R}^{\uparrow} N_{\text{cell } 1,L}^{\downarrow} N_{\text{cell } 2,L}^{\uparrow} N_{\text{cell } 2,R}^{\downarrow}} + \sqrt[4]{N_{\text{cell } 1,L}^{\uparrow} N_{\text{cell } 1,R}^{\downarrow} N_{\text{cell } 2,R}^{\uparrow} N_{\text{cell } 2,L}^{\downarrow}}} \quad (5.16)$$

$$= \frac{1}{P} \frac{\alpha \sqrt[4]{\sigma_R \sigma_L \sigma_L \sigma_R} - \sqrt[4]{\sigma_L \sigma_R \sigma_R \sigma_L}}{\alpha \sqrt[4]{\sigma_R \sigma_L \sigma_L \sigma_R} + \sqrt[4]{\sigma_L \sigma_R \sigma_R \sigma_L}}$$

$$= \frac{1}{P} \frac{\alpha - 1}{\alpha + 1}, \quad (5.17)$$

where α is an acceptance ratio and is defined as

$$\alpha = \frac{\sqrt[4]{a_{\text{cell } 1,\text{Saleve}}^{\uparrow} a_{\text{cell } 1,\text{Saleve}}^{\downarrow} a_{\text{cell } 2,\text{Jura}}^{\uparrow} a_{\text{cell } 2,\text{Jura}}^{\downarrow}}}{\sqrt[4]{a_{\text{cell } 1,\text{Jura}}^{\uparrow} a_{\text{cell } 1,\text{Jura}}^{\downarrow} a_{\text{cell } 2,\text{Saleve}}^{\uparrow} a_{\text{cell } 2,\text{Saleve}}^{\downarrow}}}. \quad (5.18)$$

The false asymmetry, Eq. 5.16, can be simplified as

$$A_{N,\text{False}} = \frac{1}{P} \frac{\sqrt[4]{N_{\text{cell 1,Saleve}} N_{\text{cell 2,Jura}}} - \sqrt[4]{N_{\text{cell 1,Jura}} N_{\text{cell 2,Saleve}}}}{\sqrt[4]{N_{\text{cell 1,Saleve}} N_{\text{cell 2,Jura}}} + \sqrt[4]{N_{\text{cell 1,Jura}} N_{\text{cell 2,Saleve}}}}. \quad (5.19)$$

That is $A_{N,\text{false}}$ is the normalized difference of counts from each target cell assuming the upstream target is always polarized down and the downstream target is always polarized up. Given that the polarization flips for both upstream and downstream target cells, $A_{N,\text{false}}$ is an asymmetry where physical effects cancel out. The kinematic dependencies of the false asymmetry are shown in Fig. 5.7 and the kinematic dependencies of the acceptance ratio, α , are shown in Fig. 5.8.

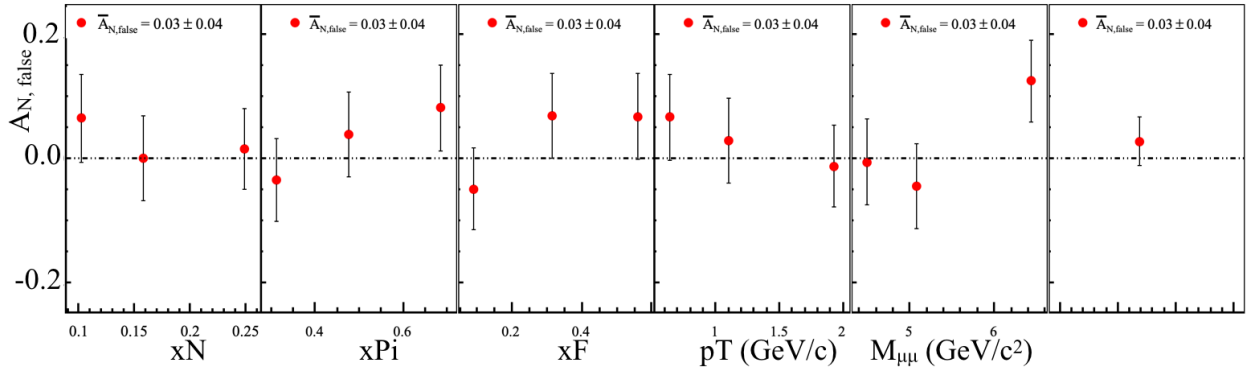


Figure 5.7: False asymmetry to estimate fluctuations in acceptance in time

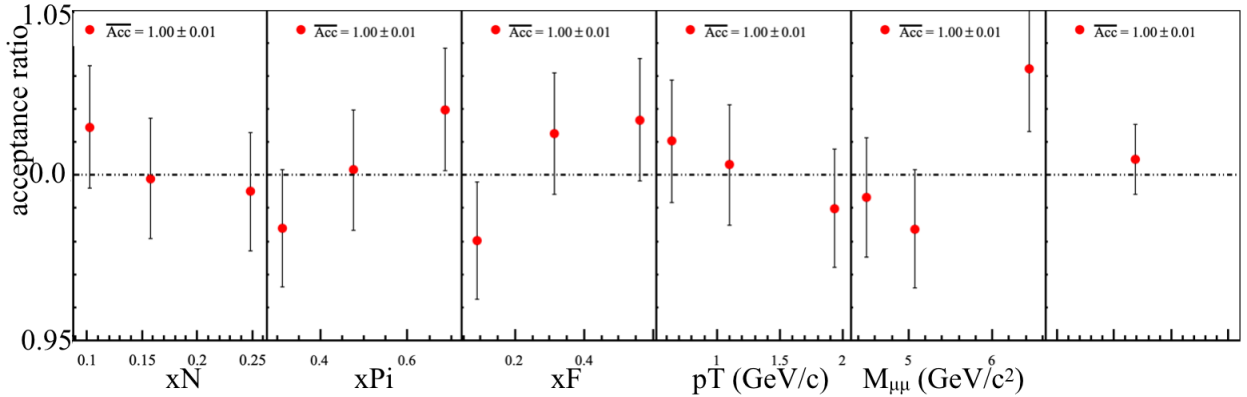


Figure 5.8: Acceptance ratio, Eq. 5.18, used to determine the systematic effects from acceptance changes in time

While α is an acceptance ratio it is not the same as the acceptance ratio in the true asymmetry. However α is similar to the true acceptance ratio, κ , in that α will only be different from unity as a result of time changes in the spectrometer. Therefore it is assumed α can be used as a good estimate of the true acceptance

ratio fluctuations. The systematic error due to acceptance fluctuations is determined as

$$\delta A_{N,\text{systematic}} = \frac{1}{P} \left(\frac{|\alpha - 1|}{2} + \delta_{\frac{|\alpha-1|}{2}} \right), \quad (5.20)$$

where this expression is derived in Appendix A.1. The kinematic dependence of the systematic error normalized to the statistical error is shown in Fig. 5.9. The binned average systematic error due to acceptance is 20% of the statistical error.

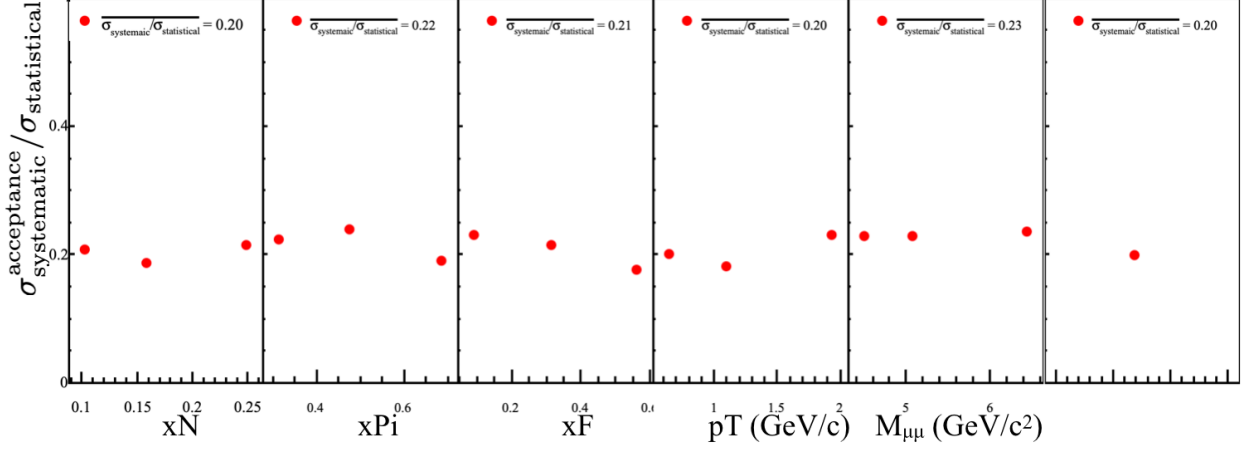


Figure 5.9: Systematic error due to acceptance effects

5.3.3 Further False Asymmetry Effects

Although the list of systematic effects specifically studied is quite exhaustive there is always the potential for other systematic effects not considered. Studies of the changes in time from additional false asymmetries were performed in an attempt to take into account all other systematic effects. All false asymmetries considered must be constructed in such a way that the physical process of interest cancels out. A false asymmetry could therefore only be non-zero from acceptance effects, luminosity or some other reason not considered. The additional false asymmetries are constructed in a way that luminosity effects cancel out and acceptance effects are approximately constant. With these assumptions, the pull values from Eq. 5.14 are expected to be distributed as a standard Gaussian distribution. Any deviation from a standard Gaussian is conservatively taken as a systematic effect from some unknown cause. The additional studied false asymmetries are summarized in the following enumerated list.

1. A false asymmetry similar to Eq. 5.16 but with the upstream left and right counts flipped defined as

$$\frac{1}{P} \frac{\sqrt[4]{N_{\text{cell } 1,\text{L}}^{\uparrow} N_{\text{cell } 1,\text{R}}^{\downarrow} N_{\text{cell } 2,\text{L}}^{\uparrow} N_{\text{cell } 2,\text{R}}^{\downarrow}} - \sqrt[4]{N_{\text{cell } 1,\text{R}}^{\uparrow} N_{\text{cell } 1,\text{L}}^{\downarrow} N_{\text{cell } 2,\text{R}}^{\uparrow} N_{\text{cell } 2,\text{L}}^{\downarrow}}}{\sqrt[4]{N_{\text{cell } 1,\text{L}}^{\uparrow} N_{\text{cell } 1,\text{R}}^{\downarrow} N_{\text{cell } 2,\text{L}}^{\uparrow} N_{\text{cell } 2,\text{R}}^{\downarrow}} + \sqrt[4]{N_{\text{cell } 1,\text{R}}^{\uparrow} N_{\text{cell } 1,\text{L}}^{\downarrow} N_{\text{cell } 2,\text{R}}^{\uparrow} N_{\text{cell } 2,\text{L}}^{\downarrow}}}. \quad (5.21)$$

This false asymmetry can be thought of as measuring the normalized counts on the Jura side minus the Saleve side. The period weighted average results of this false asymmetry are shown in Fig. 5.10 and as can be seen there is the asymmetry is systematically less than zero by more than a standard deviation. The uncorrelated pull distributions from this false asymmetry are shown in Fig. 5.11 and the corresponding Gaussian fit results are shown in Fig. 5.12. Due to the fact that there are less entries in these pull distributions the Gaussian fit results are not necessarily that good. In an attempt to correct for this and to take into account the fit errors, a weighted average of the mean and standard deviation are made, as in Eq. 5.25, using weights as the inverse fit variances. The resulting systematic error is again determined as in Eq. 5.15 using the weighted mean and weighted standard deviation.

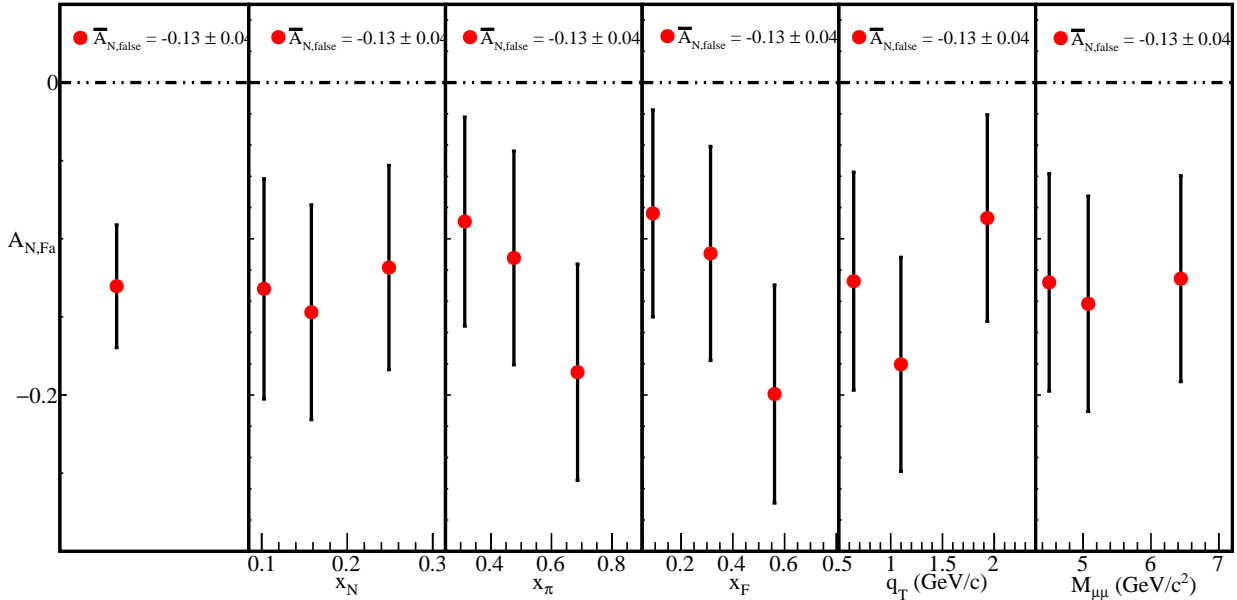


Figure 5.10: Two target geometric false asymmetry. This is non-zero due to acceptance effects

2. A false asymmetries using only the information from the upstream or the downstream target defined as

$$\frac{1}{P} \frac{\sqrt{N_{\text{cell } 1(2),\text{L}}^{\uparrow} N_{\text{cell } 1(2),\text{R}}^{\downarrow}} - \sqrt{N_{\text{cell } 1(2),\text{R}}^{\uparrow} N_{\text{cell } 1(2),\text{L}}^{\downarrow}}}{\sqrt{N_{\text{cell } 1(2),\text{L}}^{\uparrow} N_{\text{cell } 1(2),\text{R}}^{\downarrow}} + \sqrt{N_{\text{cell } 1(2),\text{R}}^{\uparrow} N_{\text{cell } 1(2),\text{L}}^{\downarrow}}}. \quad (5.22)$$

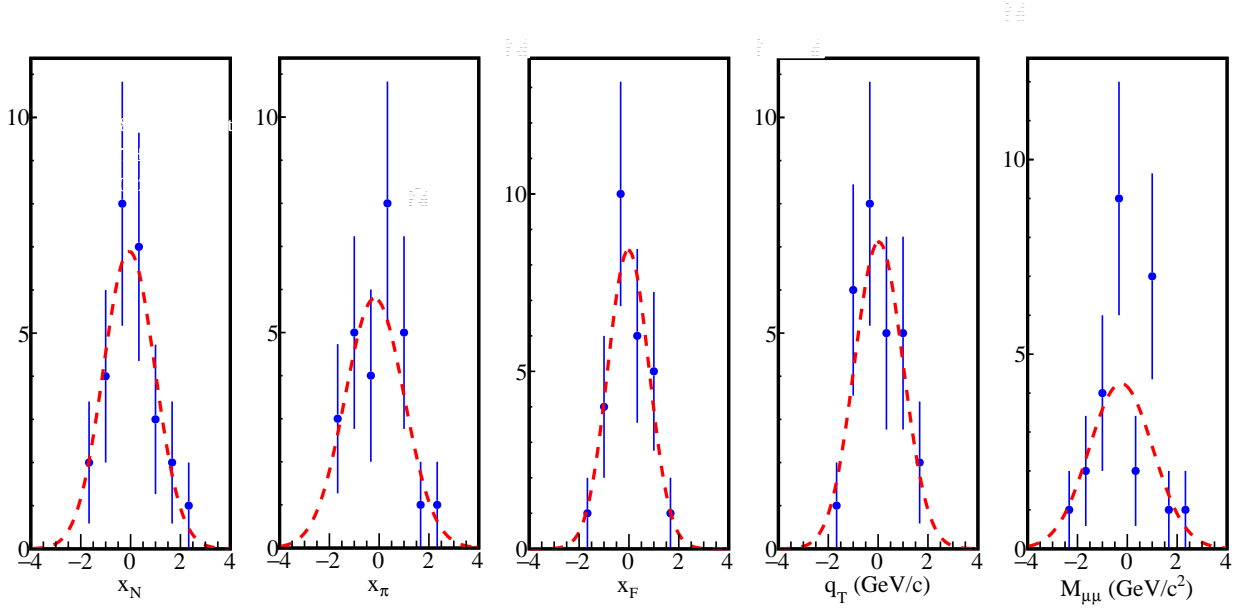


Figure 5.11: Uncorrelated pulls of the two target geomean false asymmetry

Entries	27	Entries	27	Entries	27	Entries	27	Entries	27
χ^2 / ndf	1.06 / 4	χ^2 / ndf	2.875 / 4	χ^2 / ndf	1.203 / 3	χ^2 / ndf	1.925 / 3	χ^2 / ndf	7.364 / 5
Constant	6.898 ± 2.019	Constant	5.797 ± 1.578	Constant	8.419 ± 2.089	Constant	7.116 ± 1.826	Constant	4.248 ± 1.307
Mean	-0.05617 ± 0.22189	Mean	-0.1796 ± 0.3545	Mean	-0.02243 ± 0.17361	Mean	0.0256 ± 0.2382	Mean	-0.2528 ± 0.3265
Sigma	1.032 ± 0.266	Sigma	1.187 ± 0.317	Sigma	0.8256 ± 0.1377	Sigma	0.9721 ± 0.1962	Sigma	1.279 ± 0.331

Figure 5.12: Gaussian fit results for the uncorrelated two target false geomean pulls

This false asymmetry can also be thought of as measuring the normalized counts on the Jura side minus the Saleve side but for each target individually. Both this false asymmetry and the previous false asymmetry can be written as Eq. 5.17 where α will be an acceptance ratio of Jura/Saleve. As the Jura/Saleve acceptance ratio is expected to be the same for the upstream and downstream targets, any difference between the two false asymmetries must be due to other reasons. A by period comparison between the upstream and downstream target is shown in Fig. 5.13 and as can be seen there are differences by period between the upstream and downstream asymmetries. A combined pull

distribution is made using the information from both upstream and downstream asymmetries and is shown in Fig. 5.14. As with the previous false asymmetry, lack of data leads to the same problems with fit and therefore the same weighting method is used to determine a systematic error.

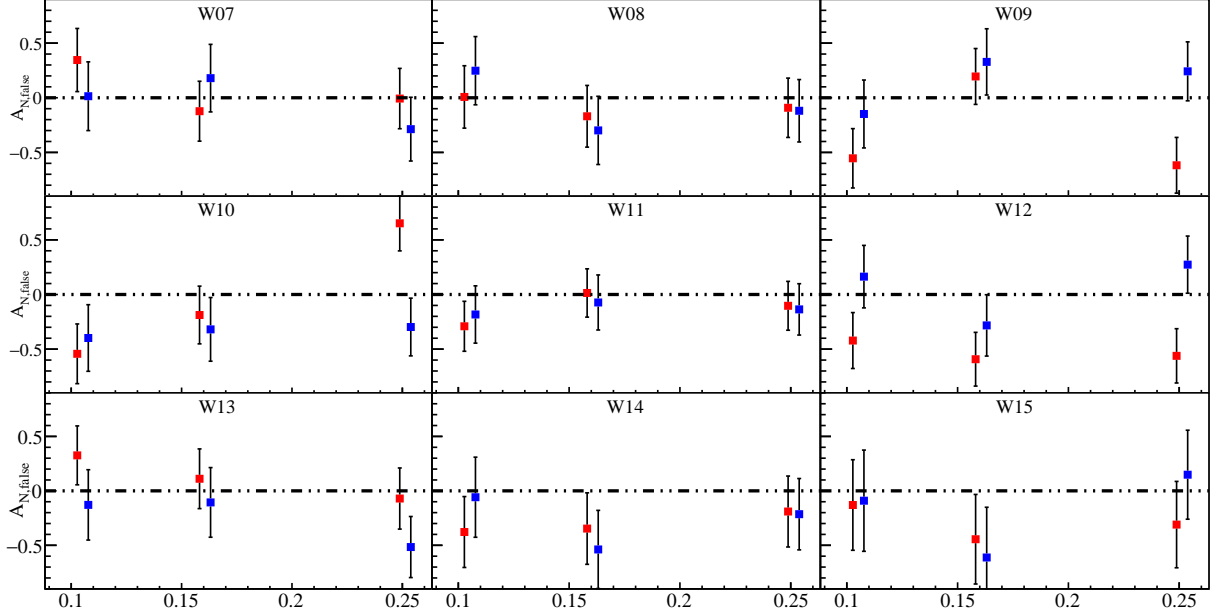


Figure 5.13: One target false asymmetries for the upstream target (red) and the downstream target (blue), as a function of x_N . Each graph is from a different period in time.

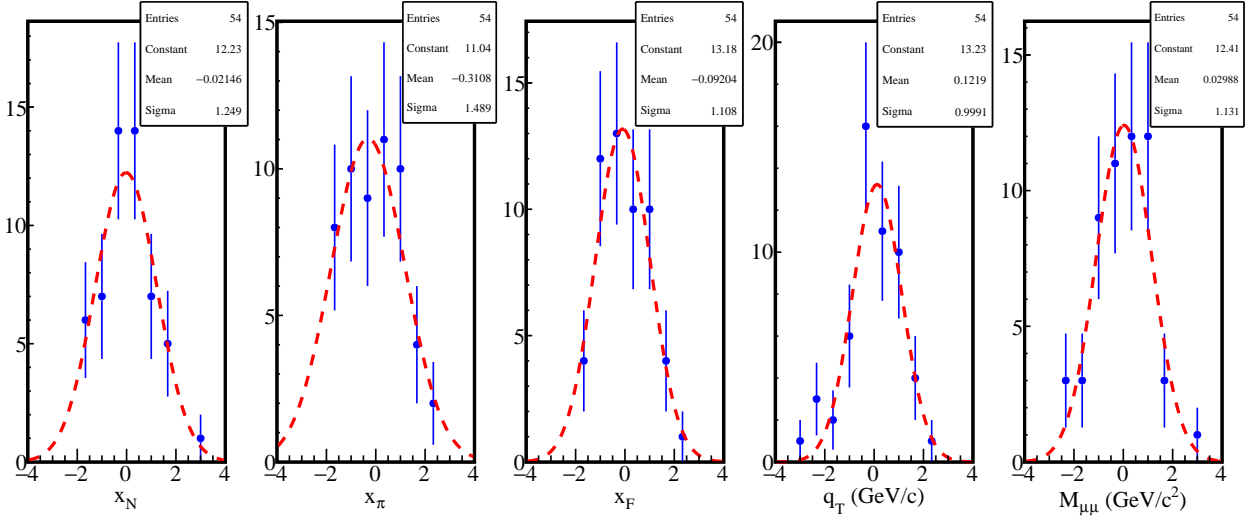


Figure 5.14: Pull values from one target geommean false asymmetries. Both upstream and downstream values are used to make this pull

3. Finally the same false asymmetry used to determine the acceptance fluctuations, Eq. 5.16, is also

checked for compatibility and a systematic error is determined in the same way as the previous false asymmetries. The pulls are shown in Fig. 5.15 and the corresponding fit parameters are shown in Fig. 5.16.

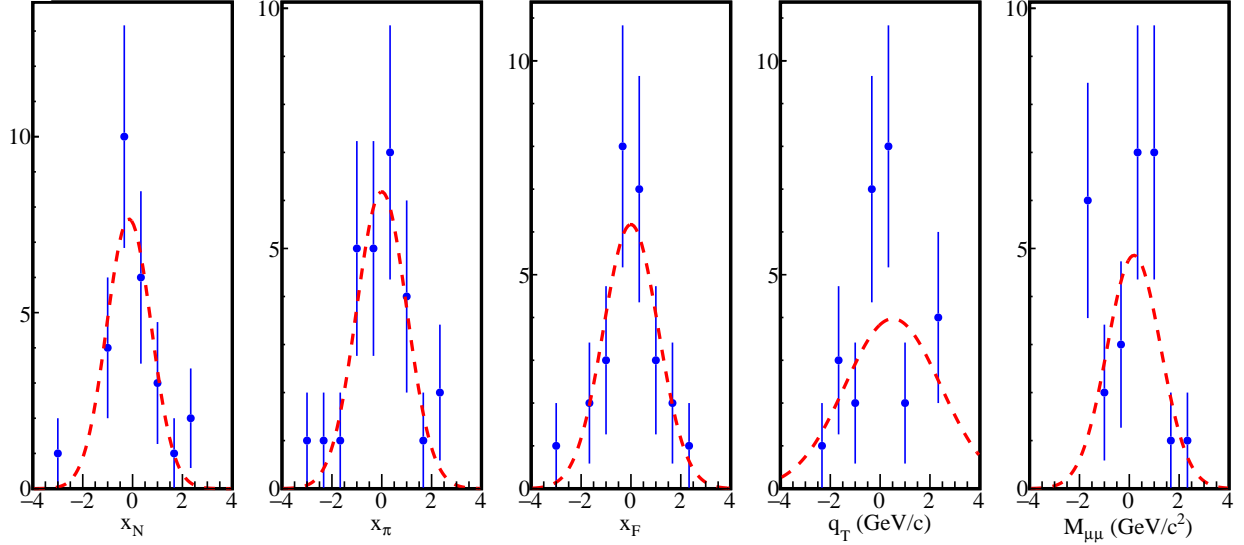


Figure 5.15: Pull distribution for a nearly acceptance free two target false geomean asymmetry

	Entries	27	Entries	27	Entries	27	Entries	27	Entries	27
1	χ^2 / ndf	3.517 / 4	χ^2 / ndf	3.737 / 6	χ^2 / ndf	2.357 / 5	χ^2 / ndf	6.734 / 4	χ^2 / ndf	7.973 / 4
Constant	7.658 ± 3.014	Constant	6.183 ± 1.859	Constant	6.176 ± 2.115	Constant	3.971 ± 1.201	Constant	4.857 ± 4.667	
Mean	-0.1441 ± 0.2765	Mean	-0.002351 ± 0.211941	Mean	-0.002406 ± 0.246275	Mean	0.5095 ± 1.1086	Mean	0.1882 ± 0.9446	
Sigma	0.891 ± 0.424	Sigma	1.004 ± 0.226	Sigma	1.098 ± 0.361	Sigma	1.92 ± 1.12	Sigma	1.072 ± 1.195	

Figure 5.16: Gaussian fit results for the previous pull distributions

A summary of the systematic error from each false asymmetry is shown in Tab. 5.5

Systematic error	$\langle \sigma_{\text{systematic}} / \sigma_{\text{statistical}} \rangle$
Two target Jura-Saleve	0.26
Combined one target	0.5
Two target acceptance estimation	0.29

Table 5.5: Summary of systematic error impacts from false asymmetries. The maximum systematic error is chosen as the systematic error.

5.3.4 Left/Right Event Migration

The spectrometer has finite resolution for any measured quantity and for this reason events measured as left outgoing could really be events that are right outgoing and vice versa for measured left outgoing events. This left-right miss-identification has the result of diluting spin-dependent effects by effectively having a sample from an unpolarized target along with the sample from the polarized target. Therefore the asymmetry A_N reduces from left-right miss-identification and this effect is included as a systematic effect.

For this thesis five Monte-Carlo processes were generated corresponding to three background processes and a spin-independent signal process. The generator used was PYTHIA8 and the data was generated and reconstruction at Blue Waters. The background processes simulated were JPsi production, Psi' production and open charm (OC) production. Each of these backgrounds can decay into two muons which results in a background contamination to the Drell-Yan signal. Table ?? gives the parameters used for the Monte-Carlo studied.

Table 5.6: Monte-Carlo settings produced on Blue Waters

Event generator	PYTHIA8
Pion pdf	GRVPI1
Proton pdf	NNPDF23
proton/neutron mixing ratio	1.96
Initial state radiation	on
Final state radiation	on
Multiple parton interactions	on
Simulated detector efficiencies	uniform

Miss-identification was estimated from the simulated Monte-Carlo data sample described in Table ?? where the sample was made from the respond of the COMPASS spectrometer to input Drell-Yan events in a similar mass range. The same analysis performed on real data was performed on this Monte-Carlo data to get the angles of interest. Fig. 5.17 shows the rate of events identified correctly and incorrectly as a function of the ϕ_S . This plot is made by determining which outgoing direction the generated events emerged with the outgoing direction the reconstructed events emerged.

As is clearly visible there is a band of higher miss-identification rate at the border between left and right.

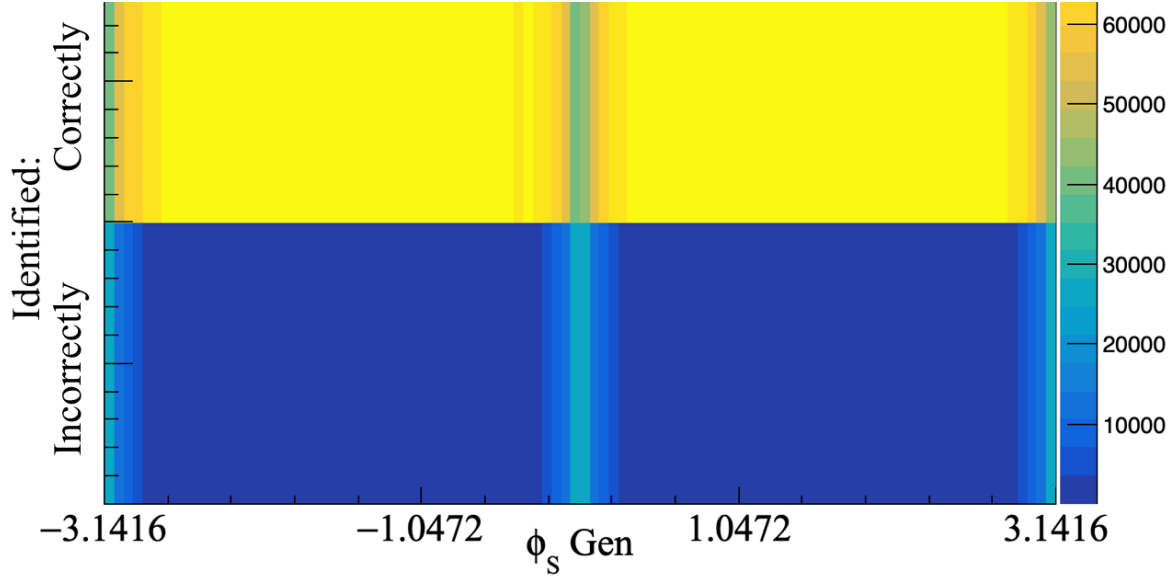


Figure 5.17: The rate of identified correctly and incorrectly left-right events as a function of ϕ_S . This is determined by comparing the generated outgoing direction with the reconstructed outgoing direction. The left-right boundary is clearly visible at $\phi_S = 0^\circ$ and $\phi_S = -\pi^\circ$ and $\phi_S = \pi^\circ$

For this reason a cut in the ϕ_S variable symmetric about the left-right border was tested to determine the percent of miss-identification as a function of the amount of ϕ_S cut. These results are shown in Fig. 5.18.

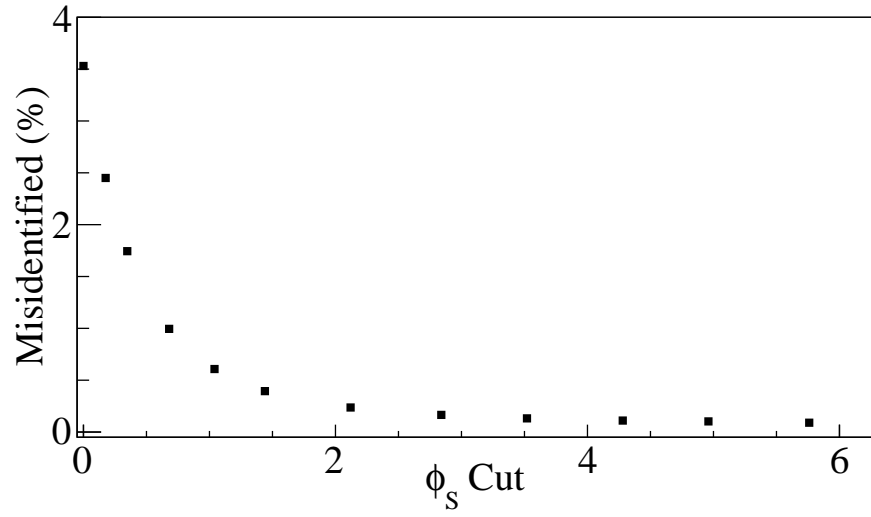


Figure 5.18: Percent left-right migration as a function of the amount of ϕ_S cut.

The systematic error for left-right migration is calculated as

$$\delta A_{N,\text{systematic}} = \gamma * A_N + \gamma * \delta A_N, \quad (5.23)$$

where this expression is derived in Appendix A.2.

No cut on ϕ_S was used for the asymmetry due to the fact that the systematic error is already small with no cut in ϕ_S and to avoid loss of statistics. The integrated systematic error due to left-right event migration was determined to be 9%.

5.3.5 Total Systematics

The total systematic error is determined by adding all non-zero systematic effects in quadrature as

$$\left\langle \frac{\sigma_{\text{systematics}}}{\sigma_{\text{statistical}}} \right\rangle = \sqrt{\sum_i^{\text{all systematics}} \left\langle \frac{\sigma_{\text{systematics},i}^2}{\sigma_{\text{statistical}}^2} \right\rangle}, \quad (5.24)$$

where all the systematic effects considered are summarized in Tab. 5.7.

Systematic error	$\langle \sigma_{\text{systematic}}/\sigma_{\text{statistical}} \rangle$	$\langle \sigma_{\text{systematic}} \rangle$	$\langle \sigma_{\text{statistical}} \rangle$
Period compatibility	0.0	0.0	0.039
Acceptance fluctuation	0.2	0.008	0.039
False asymmetry	0.5	0.020	0.039
Left-Right migration	0.09	0.004	0.039
Total	0.55	0.021	0.039

Table 5.7: Summary of systematic error impacts to the integrated asymmetry

5.4 Results

The asymmetries in this analysis are extracted separately from each of the nine data periods, Table 5.1, and then combined as a weighted average. This calculation method is used to minimize the effects of acceptance changes between periods as the spectrometer was kept stable within each period but had the options for detector changes and repairs between periods. This resulting asymmetry, A_N for each method, section 5.2.1 and section 5.2.2, is determined from a weighted average as

$$A_N = \frac{\sum_{\text{period}} A_{N,\text{period}} \sigma_{\text{period}}^{-2}}{\sum_{\text{period}} \sigma_{\text{period}}^{-2}}, \quad \delta A_N = \sqrt{\sum_{\text{period}} \frac{1}{\sigma_{\text{period}}^{-2}}}. \quad (5.25)$$

The results for the basic geometric mean are shown in Fig. 5.19 and the results for the two target geometric mean are shown in Fig. 5.20. The numerical values for the two-target geometric mean with statistical and

systematic error bars are summarized in Table ???. The systematic error bars are discussed in Sec. 5.3.

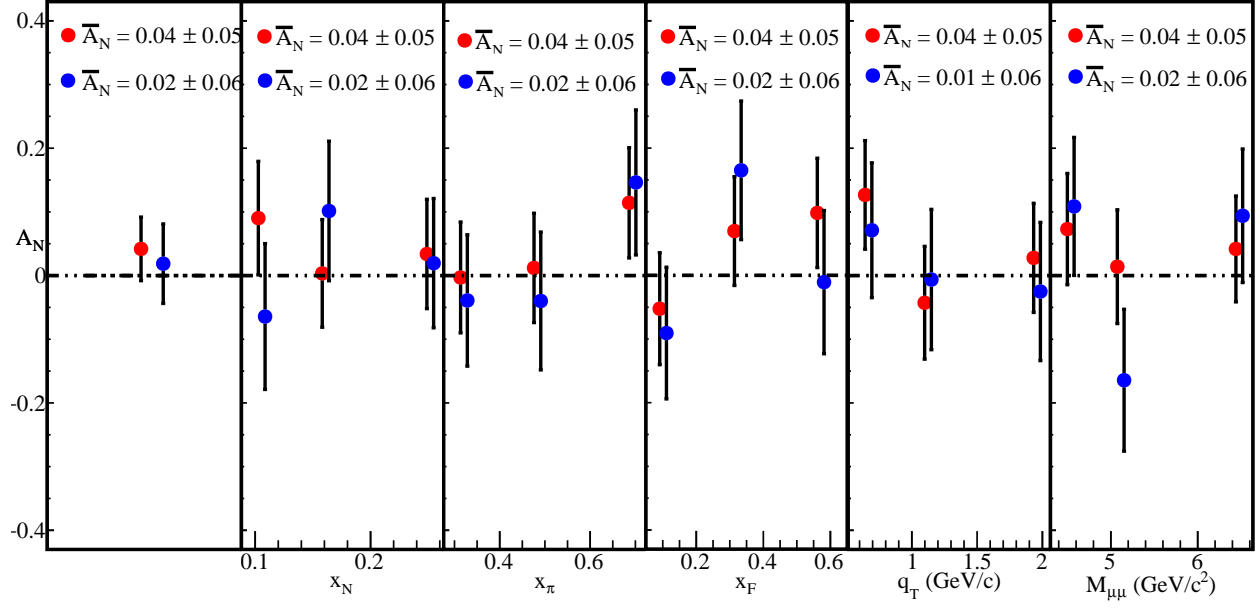


Figure 5.19: A_N determined from the geometric mean method for the upstream target (red) and the downstream target (blue) for all kinematic binnings

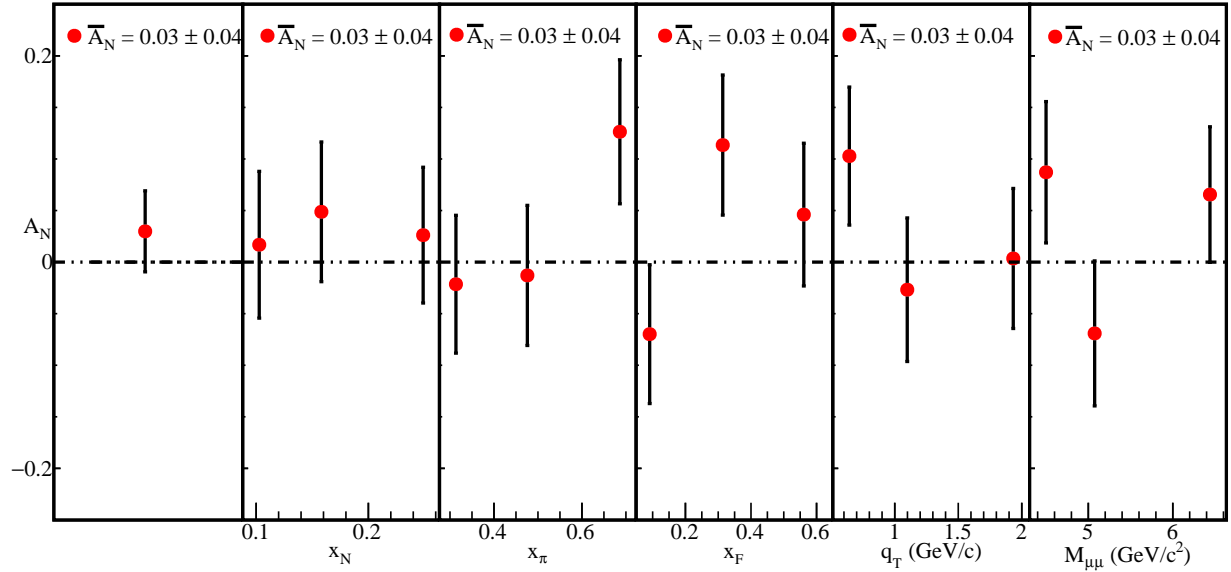


Figure 5.20: A_N determined by the two-target geometric mean method for all kinematic binnings

Table 5.8: Two-Target geometric mean numerical values and error bars for each kinematic bin

Binning variable	Bin Range	A_N	δA_N^{stat}	δA_N^{sys}
$\langle x_N \rangle$				

5.4.1 Comparison of results

List of Figures

1.1	The leading order Feynman diagram for deep inelastic scattering	1
1.2	The F_2 structure function measured by several experiments. Note that the data is shifted up by a factor 2^{ix} to see the x dependence. Image taken from [38]	4
1.3	The unpolarized parton distribution functions times the momentum fraction. The different color correspond to different quarks or gluons. Image taken from [38]	5
1.4	The longitudinally polarized parton distribution functions times the momentum fraction for the u-quark (top) and the d-quark (bottom). Image taken from [38]	6
1.5	The eight TMDs needed to describe a spin 1/2 nucleon at leading order. The columns represent the different nucleon polarization and the rows represent the different quark polarizations. The individual figures give a visual of the TMD's interpretation.	7
1.6	The semi-inclusive deep inelastic scattering leading order Feynman diagram	8
1.7	The γ -nucleon lab frame where the target nucleon is at rest and the virtual photon is along the z-axis. The lepton scattering plane defines the xz-plane where the outgoing lepton defines the positive x-direction. This image was taken from [10].	10
1.8	The asymmetry amplitude related to the Sivers function measure by COMPASS [8] and HERMES [5]	12
1.9	The Drell-Yan leading order diagram	13
2.1	The CERN experiments and accelerators	18
2.2	A schematic of the 2015 COMPASS setup	18
2.3	The M2 beam line at CERN	20
2.4	Bending the beam to a horizontal position. The BMS detectors are upstream and downstream of the bend 6 magnet.	21
2.5	The momentum distribution of the π^- beam, determined during dedicated low intensity beam conditions	22
2.6	Light lines emitted inside CEDARs at COMPASS. The red(green) lines correspond to Cherenkov light emitted from a particle.	22
2.7	The polarized target at COMPASS	23
2.8	The empty polarized target cells side by side along with their NMR coil positions	25
2.9	Principle of operation for the micromesh gaseous structures (micromegas)	28
2.10	The operation principle of the gas electron multiplier (GEM) detectors	29
2.11	Drift cell of a drift chamber with the ionized drift electron lines coming from the incident charged particle	30
2.12	Front on view of a the active area of a straw detector at COMPASS	31
2.13	The richwall mini drift tubes	31
2.14	Side view demonstrating the principle of operation of the RICH detector.	33
2.15	Frontal view of the electromagnetic calorimeter 1	33
2.16	Frontal view of the electromagnetic calorimeter 2	34
2.17	A side view sketch of the muon wall 1 detector	35
2.18	Top view of the spectrometer highlighting how different particles can signal a trigger	36

2.19	The two types of triggers (left is target pointing and right is energy loss) at COMPASS and an illustration of the coincidence matrix used to select events of interest	36
2.20	The kinematic coverage for the 2015 triggers determined from Monte-Carlo studies	37
2.21	The data acquisition steps at COMPASS	39
2.22	The schematic of the CORAL reconstruction process	40
2.23	The hadron absorber downstream of the polarized target in 2015	42
2.24	Side view of the hadron absorber used in 2015	42
3.2	View down the axis of a drift cell and the equal voltages for this drift cell configuration. This image is taken from [12]	45
3.3	A simulation of the position resolution as a function of the number of primary electrons needed to record a signal. This image is taken from [12]	46
3.4	Garfield simulation of the induced signal current versus the arrival time. The green line corresponds to the arrival time of the fifth election. This image is taken from [12]	47
3.5	Inside view of prototype A. This image was taken from [22]	47
3.6	48
3.7	A side view sketch of the layers in DC05	49
3.8	50
3.9	Stretching mylar on a cathode plane at CERN	50
3.10	Hand soldering DC05 wires in the clean room at the NPL	51
3.11	The process of stacking the G-10 frames at CERN	51
3.12	52
3.13	53
3.14	The double residual distribution for the V plane together with a Gaussian fit in red to determine the variance of the distribution	54
4.1	The residual distribution for a straw detector plane	63
4.2	The residual as a function of the detector v-coordinate for a straw detector	63
4.3	The residual as a function of the detector u-coordinate for a straw detector	64
4.4	The reduced χ^2 from alignment data tracks	64
5.1	Event selection statistics for this analysis	69
5.2	The definition of the left plane (red) and right plane (green) defined from a target spin up configuration in the target frame	71
5.3	A_N determined for each period	75
5.4	Pull distribution from the two target geometric mean	76
5.5	Uncorrelated pull distributions	76
5.6	Results of Gaussian fit for the uncorrelated pull distributions	77
5.7	False asymmetry to estimate fluctuations in acceptance in time	78
5.8	Acceptance ratio, Eq. 5.18, used to determine the systematic effects from acceptance changes in time	78
5.9	Systematic error due to acceptance effects	79
5.10	Two target geomean false asymmetry. This is non-zero due to acceptance effects	80
5.11	Uncorrelated pulls of the two target geomean false asymmetry	81
5.12	Gaussian git results for the uncorrelated two target false geomean pulls	81
5.13	One target false asymmetries for the upstream target (red) and the downstream target (blue), as a function of x_N . Each graph is from a different period in time.	82
5.14	Pull values from one target geomean false asymmetries. Both upstream and downstream values are used to make this pull	82
5.15	Pull distribution for a nearly acceptance free two target false geomean asymmetry	83
5.16	Gaussian fit results for the previous pull distributions	83
5.17	The rate of identified correctly and incorrectly left-right events as a function of ϕ_S . This is determined by comparing the generated outgoing direction with the reconstructed outgoing direction. The left-right boundary is clearing visible at $\phi_S = 0^\circ$ and $\phi_S = -\pi^\circ$ and $\phi_S = \pi^\circ$.	85

5.18	Percent left-right migration as a function of the amount of ϕ_S cut.	85
5.19	A_N determined from the geometric mean method for the upstream target (red) and the down-stream target (blue) for all kinematic binnings	87
5.20	A_N determined by the two-target geometric mean method for all kinematic binnings	87

List of Tables

4.1	COMPASS 2015 alignment data runs	57
5.1	COMPASS 2015 data taking periods	65
5.2	Stability analysis rejection percentages	68
5.3	Analysis binning limits	70
5.4	Notations used in defining the left/right asymmetry	72
5.5	Summary of systematic error impacts from false asymmetries. The maximum systematic error is chosen as the systematic error.	84
5.6	Monte-Carlo settings produced on Blue Waters	84
5.7	Summary of systematic error impacts to the integrated asymmetry	86
5.8	Two-Target geometric mean numerical values and error bars for each kinematic bin	88

Appendix A

Systematic Error Derivations

A.1 Systematic Error From Acceptance

For an asymmetry defined as

$$A_\alpha = \frac{1}{P} \frac{\alpha\sigma_L - \sigma_R}{\alpha\sigma_L + \sigma_R} \quad (\text{A.1})$$

where α is an acceptance ratio. α is assumed to be close to unity therefore let

$$\alpha = 1 \pm 2 * \epsilon, \quad (\text{A.2})$$

where ϵ is a small positive number. The asymmetry can therefore be written

$$\frac{1}{P} \frac{(1 \pm 2 * \epsilon)\sigma_L - \sigma_R}{(1 \pm 2 * \epsilon)\sigma_L + \sigma_R} = \frac{1}{P} \frac{\sigma_L - \sigma_R \pm 2 * \epsilon * \sigma_L}{(\sigma_L + \sigma_R)(1 \pm \frac{2*\epsilon*\sigma_L}{\sigma_L+\sigma_R})}. \quad (\text{A.3})$$

From there Taylor expand the denominator to get

$$A_\alpha \approx \frac{1}{P} \frac{\sigma_L - \sigma_R \pm 2 * \epsilon * \sigma_L}{(\sigma_L + \sigma_R)} * \left(1 \mp \frac{2 * \epsilon * \sigma_L}{\sigma_L + \sigma_R}\right) \quad (\text{A.4})$$

$$= A_N \pm \frac{1}{P} \frac{2 * \epsilon * \sigma_L}{\sigma_L + \sigma_R} \mp A_N * \frac{2 * \epsilon * \sigma_L}{\sigma_L + \sigma_R} \mp \frac{1}{P} \left(\frac{2 * \epsilon * \sigma_L}{\sigma_L + \sigma_R} \right)^2.$$

Assuming A_N is small and $\sigma_L \approx \sigma_R$

$$A_\alpha \approx A_N \pm \frac{\epsilon}{P}. \quad (\text{A.5})$$

The true asymmetry can now be written

$$A_{N,\text{systematic}} \approx A_\alpha \mp \frac{\epsilon}{P}. \quad (\text{A.6})$$

Including the $\frac{\epsilon}{P}$ term as an additive error and using standard error propagation the systematic error can be approximated as

$$\delta A_{N,\text{systematic}} = \frac{|\alpha - 1|}{2} \frac{1}{P} + \frac{\delta_{\frac{|\alpha-1|}{2}}}{P}. \quad (\text{A.7})$$

A.2 Systematic Error From Left-Right Event Migration

Assuming the fraction of events miss-identified is γ and that the amount of miss-identified events reconstructed left equals the amount of outgoing events reconstructed right

$$A_{N,\text{measure}} = \frac{1}{P} \frac{(L + \frac{\gamma}{2}N_{\text{total}}) - (R + \frac{\gamma}{2}N_{\text{total}})}{(L + \frac{\gamma}{2}N_{\text{total}}) + (R + \frac{\gamma}{2}N_{\text{total}})} = \frac{1}{P} \frac{L - R}{(L + R) * (1 + \gamma * \frac{N_{\text{total}}}{L + R})}, \quad (\text{A.8})$$

where N_{total} is the total events measure, L is the true events measured to the left that should be measured left and R is the number of events measure to the right that should be measured to the right.

Assuming γ is a small percentage, the denominator can be Taylor expanded to give

$$A_{N,\text{measure}} \approx A_N \left(1 - \gamma * \frac{N_{\text{total}}}{L + R} \right). \quad (\text{A.9})$$

Including $\gamma A_{N,\text{measure}}$ as an additive error and using standard error propagation the systematic error can be approximated as

$$\delta A_{N,\text{systematic}} = \gamma * A_{N,\text{measure}} + \gamma * \delta A_{N,\text{measure}}. \quad (\text{A.10})$$

References

- [1] P. Abbon et al. The COMPASS experiment at CERN. *Nucl. Instrum. Meth.*, A577:455–518, 2007.
- [2] A. Abragam and M. Goldman. Principles of dynamic nuclear polarisation. *Reports on Progress in Physics*, 41:395–467, 1978.
- [3] I. Abt, A. M. Cooper-Sarkar, B. Foster, V. Myronenko, K. Wichmann, and M. Wing. Study of HERA ep data at low Q^2 and low x_{Bj} and the need for higher-twist corrections to standard perturbative QCD fits. *Phys. Rev.*, D94(3):034032, 2016.
- [4] B. Adeva et al. The Spin dependent structure function $g(1)(x)$ of the proton from polarized deep inelastic muon scattering. *Phys. Lett.*, B412:414–424, 1997.
- [5] A. Airapetian et al. Observation of the Naive-T-odd Sivers Effect in Deep-Inelastic Scattering. *Phys. Rev. Lett.*, 103:152002, 2009.
- [6] A. et al. Airapetian. Flavor decomposition of the sea-quark helicity distributions in the nucleon from semiinclusive deep inelastic scattering. *Phys. Rev. Lett.*, 92:012005, Jan 2004.
- [7] V. Yu. Aleksakhin, Y. Bedfer, S. Gerasimov, and A. Yu. Korzenev. Geometrical event reconstruction in the COMPASS experiment. *Phys. Part. Nucl. Lett.*, 4:350–362, 2007. [Pisma Fiz. Elem. Chast. Atom. Yadra2007,no.4,588(2007)].
- [8] M. Alekseev et al. Collins and Sivers asymmetries for pions and kaons in muon-deuteron DIS. *Phys. Lett.*, B673:127–135, 2009.
- [9] S. Arnold, A. Metz, and M. Schlegel. Dilepton production from polarized hadron hadron collisions. *Phys. Rev.*, D79:034005, 2009.
- [10] Alessandro Bacchetta, Markus Diehl, Klaus Goeke, Andreas Metz, Piet J. Mulders, and Marc Schlegel. Semi-inclusive deep inelastic scattering at small transverse momentum. *JHEP*, 02:093, 2007.
- [11] Vincenzo Barone, Alessandro Drago, and Philip G. Ratcliffe. Transverse polarisation of quarks in hadrons. *Phys. Rept.*, 359:1–168, 2002.
- [12] Ran Bi. Simulation of properties of compass drift-chamber prototypes. DNP, 2013.
- [13] J. D. Bjorken and Emmanuel A. Paschos. Inelastic Electron Proton and gamma Proton Scattering, and the Structure of the Nucleon. *Phys. Rev.*, 185:1975–1982, 1969.
- [14] Volker Blobel and Claus Kleinwort. A New method for the high precision alignment of track detectors. In *Advanced Statistical Techniques in Particle Physics. Proceedings, Conference, Durham, UK, March 18-22, 2002*, pages URL-STR(9), 2002.
- [15] Elliott D. Bloom et al. High-Energy Inelastic e p Scattering at 6-Degrees and 10-Degrees. *Phys. Rev. Lett.*, 23:930–934, 1969.
- [16] Daniel Boer and P. J. Mulders. Time reversal odd distribution functions in lepto-production. *Phys. Rev.*, D57:5780–5786, 1998.

- [17] Radja Boughezal, John M. Campbell, R. Keith Ellis, Christfried Focke, Walter Giele, Xiaohui Liu, Frank Petriello, and Ciaran Williams. Color singlet production at NNLO in MCFM. *Eur. Phys. J.*, C77(1):7, 2017.
- [18] Martin Breidenbach, Jerome I. Friedman, Henry W. Kendall, Elliott D. Bloom, D. H. Coward, H. C. DeStaeler, J. Drees, Luke W. Mo, and Richard E. Taylor. Observed Behavior of Highly Inelastic electron-Proton Scattering. *Phys. Rev. Lett.*, 23:935–939, 1969.
- [19] Stanley J. Brodsky, Dae Sung Hwang, and Ivan Schmidt. Final state interactions and single spin asymmetries in semiinclusive deep inelastic scattering. *Phys. Lett.*, B530:99–107, 2002.
- [20] Stanley J. Brodsky, Dae Sung Hwang, and Ivan Schmidt. Initial state interactions and single spin asymmetries in Drell-Yan processes. *Nucl. Phys.*, B642:344–356, 2002.
- [21] C. G. Callan and David J. Gross. High-energy electroproduction and the constitution of the electric current. *Phys. Rev. Lett.*, 22:156–159, Jan 1969.
- [22] IhnJea Choi. Desy test-beam measurement with compass drift chamber prototypes. DNP, 2013.
- [23] John C. Collins. Leading twist single transverse-spin asymmetries: Drell-Yan and deep inelastic scattering. *Phys. Lett.*, B536:43–48, 2002.
- [24] Juan Rojo et. al. The PDF4lhc report on PDFs and LHC data: results from run i and preparation for run II. *Journal of Physics G: Nuclear and Particle Physics*, 42(10):103103, sep 2015.
- [25] R. Fruhwirth. Application of Kalman filtering to track and vertex fitting. *Nucl. Instrum. Meth.*, A262:444–450, 1987.
- [26] F Gautheron et al. COMPASS-II Proposal. 2010.
- [27] L. A. Harland-Lang, A. D. Martin, P. Motylinski, and R. S. Thorne. The impact of the final HERA combined data on PDFs obtained from a global fit. *Eur. Phys. J.*, C76(4):186, 2016.
- [28] M. Hirai and S. Kumano. Determination of gluon polarization from deep inelastic scattering and collider data. *Nucl. Phys.*, B813:106–122, 2009.
- [29] A. Kotzinian. Description of polarized $\pi^- + N$ Drell-Yan processes.
- [30] P. J. Mulders and R. D. Tangerman. The Complete tree level result up to order $1/Q$ for polarized deep inelastic leptoproduction. *Nucl. Phys.*, B461:197–237, 1996. [Erratum: Nucl. Phys.B484,538(1997)].
- [31] Emanuele R. Nocera, Richard D. Ball, Stefano Forte, Giovanni Ridolfi, and Juan Rojo. A first unbiased global determination of polarized PDFs and their uncertainties. *Nucl. Phys.*, B887:276–308, 2014.
- [32] H. Pereira and J. M. Le Goff. Compass Spectrometer Alignment.
- [33] C. Quintans. Las reconstruction efficiency - dc05/st03. COMPASS DY, March, 12 2014.
- [34] C. Quintans. Las reconstruction efficiency without dc05/st03. COMPASS DY, March, 28 2014.
- [35] I. A. Savin. COMPASS results on the nucleon spin structure. *Nucl. Phys. Proc. Suppl.*, 219-220:94–101, 2011.
- [36] Dennis W. Sivers. Single Spin Production Asymmetries from the Hard Scattering of Point-Like Constituents. *Phys. Rev.*, D41:83, 1990.
- [37] Torbjrn Sjstrand, Stefan Ask, Jesper R. Christiansen, Richard Corke, Nishita Desai, Philip Ilten, Stephen Mrenna, Stefan Prestel, Christine O. Rasmussen, and Peter Z. Skands. An Introduction to PYTHIA 8.2. *Comput. Phys. Commun.*, 191:159–177, 2015.
- [38] M. Tanabashi et al. Review of Particle Physics. *Phys. Rev.*, D98(3):030001, 2018.
- [39] R. Veenhof. Garfield - simulation of gaseous detectors. <http://cern.ch/garfield>.